

Harry E. Martz, Jr., Center Director

The Center for Nondestructive Characterization (CNDC) envisions significantly advancing research and development of nondestructive characterization science to enable successful Lawrence Livermore National Laboratory (LLNL) and Department of Energy (DOE) programs, and to be a national science and technology resource.

The CNDC near-term strategic mission objectives will advance core competencies and technologies in two areas: 1) quantitative NDC and 2) fast 3-D nanoscale imaging.

Quantitative NDC includes quantitative multidimensional nondestructive measurements to determine physical properties such as geometry, density, elemental and molecular composition; thermal, structural, and mechanical properties; stress state; and radioactive assay, in three dimensions and as a function of time.

Fast nanoscale imaging provides many programs with quantitative multidimensional (>3-D) imaging down to nanometer-scale lengths.

Our long-term strategic mission objectives include extension of near-term missions, plus embedded-in-design, multi-spectral imaging, and miniaturization for portability. The embedded-in-design objective will unite currently diverse and non-coupled technologies such as design, modeling, materials properties with characterization, testing, process monitoring and control, reverse engineering, and refurbishment and reuse into a global package to impact the engineering process. Multi-spectral imaging will expand the spectral range of CNDC imaging technologies and increase the synergism between different methodologies. The portability objective is to reduce current and new CNDC systems to the size of a small suitcase.

The CNDC FY-99 mission objectives are advancing core competencies and technologies, including the following programs:

Weapon system performance—this includes 3-D measurements over a large extent with high spatial resolution and advanced diagnostics. Examples include the Advanced Radiography Campaign and materials properties;

Science-based stockpile stewardship—specifically, durability and life prediction;

Extraordinary laser systems—this includes advanced diagnostics, for example, for fusion targets and automated *in situ* optics damage inspection;

Nonproliferation, arms control, and international security—related to reducing the threat from weapons of mass destruction.

CNDC supports a multidisciplinary team, consisting of mechanical and electronics engineers, physicists, materials and computer scientists, chemists, technicians, and radiographers, from LLNL, academia, and industry, within the U.S. and abroad. This collaboration brings together disciplines to provide the key scientific and technological advancements required to address LLNL programmatic and industrial nondestructive characterization challenges.

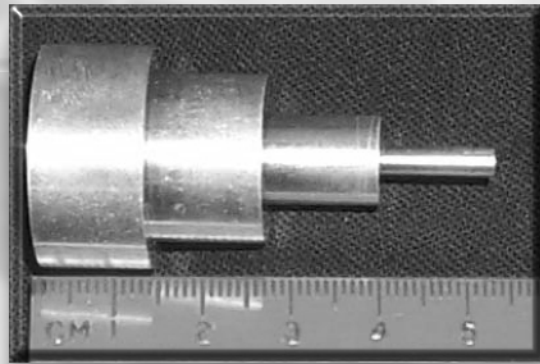
CNDC provides materials characterization, aid in process design and development, and encompasses process monitoring and control sensors and the monitoring of in-service damage. CNDC is also being applied at the end of a part's life for proper reuse or safe and proper disposal. Therefore, CNDC is becoming a front-line and end-of-line technology that strongly impacts issues of certification, life prediction, life extension, reuse, and disposal.

This year CNDC collaborated with Defense and Nuclear Technologies, Enhanced Surveillance Program, Nonproliferation, Arms Control and International Security, Lasers, the Microtechnology Center and Johns Hopkins University. Such collaborations enable CNDC to stay at the leading edge of CNDC technology, research, and development.

The primary contributions of the CNDC this year are described in the nine reports that follow: 1) The Optically Parallel Ultrasound Sensor (OPUS); 2) Speckle Reduction for LIDAR Using Optical Phase Conjugation; 3) Evaluation of an Amorphous-Silicon Array for Industrial X-Ray Imaging; 4) High-Frequency Laser-Based Ultrasound for NDC Applications; 5) New Developments in RECON; 6) Component Gap Detection by Infrared Imaging; 7) Quantitative Tomography Simulations and Reconstruction Algorithms; 8) Ultra-Wideband Phased Array; and 9) Photonic Velocimetry System Optimization.

Center for Nondestructive Characterization

5



5. Center for Nondestructive Characterization

Overview

Harry E. Martz, Jr., Center Director

The Optically Parallel Ultrasound Sensor (OPUS)

Jeffrey S. Kallman, A. Elaine Ashby, Graham H. Thomas, and Dino R. Ciarlo 5-1

Speckle Reduction for LIDAR Using Optical Phase Conjugation

Mark W. Bowers. 5-5

Evaluation of an Amorphous-Silicon Array for Industrial X-Ray Imaging

Kenneth W. Dolan, Clinton M. Logan, Jerry J. Haskins, R. Derrill Rikard, and Daniel J. Schneberk. 5-11

High-Frequency Laser-Based Ultrasound for NDC Applications

Robert D. Huber, Graham H. Thomas, Howard Lee, Christopher Richardson, and Professor James Spicer. . 5-25

New Developments in RECON

Jessie A. Jackson. 5-31

Component Gap Detection by Infrared Imaging

Charles S. Landram, Richard W. Martin, Nancy K. Delgrande, and Philip F. Durbin 5-37

Quantitative Tomography Simulations and Reconstruction Algorithms

*Harry E. Martz, Jr., Dennis M. Goodman, Jessie A. Jackson, Clinton M. Logan,
Maurice B. Aufderheide, III, Alexis Schach von Wittenau, James M. Hall, and Dale M. Sloan 5-47*

Ultra-Wideband Phased Array

Rexford M. Morey. 5-71

Photonic Velocimetry System Optimization

Paul D. Sargis, Nicole E. Molau, Jeffrey B. Cooke, Oliver T. Strand, and Mark E. Lowry. 5-77

The Optically Parallel Ultrasound Sensor (OPUS)

Jeffrey S. Kallman
Defense Sciences Engineering Division
Electronics Engineering

A. Elaine Ashby and Graham H. Thomas
Manufacturing and Materials Engineering Division
Mechanical Engineering

Dino R. Ciarlo
Engineering Research Division
Electronics Engineering

In FY-99 we extended the FY-98 proof-of-principle work on the Optically Parallel Ultrasound Sensor (OPUS) and produced working acoustic field sensors. We used these sensors to acquire transmission ultrasound data over a planar region. These sensors will be useful in transmission ultrasound imaging as well as ultrasonic tomography.

Introduction

Nondestructive Characterization (NDC) is important for evaluating materials and processes without causing damage. At Lawrence Livermore National Laboratory (LLNL) we have a variety of means of doing nondestructive inspections. The main imaging technologies involve either x rays or ultrasound. X-ray imaging is very useful, but sometimes a subject is either difficult to penetrate, has low x-ray contrast, or might be damaged by radiation. Ultrasonic inspection is sometimes used in these situations. Ultrasound has different penetration and contrast characteristics than x rays, as well as eliminating the subject's exposure to ionizing radiation.

Among the ultrasound modalities in use at LLNL is transmission ultrasound imaging. This modality is best suited to imaging subjects that are lossy (such as ceramics). In this modality the subject is placed in an ultrasound medium bath, insonified by an acoustic source, and the resultant output acoustic field is mechanically scanned with an ultrasound sensor (see **Fig. 1**). This imaging modality, although useful, is very time-consuming (taking approximately 20 min to collect the data from small objects).

Transmission ultrasound imaging yields the phase and amplitude of the acoustic field transmitted by the object of interest. These data are the information needed to perform volumetric imaging of the object of interest. Unfortunately, many views of the object are required before the volume can be reconstructed, and the time required to collect the necessary views means that this imaging modality is so expensive that only the most important objects can be imaged in this manner.

In an effort to speed the acquisition of transmission ultrasound data (and make feasible the routine use of volumetric ultrasound imaging), we have developed the Optically Parallel Ultrasound Sensor (OPUS). This sensor uses the phenomenon of frustrated total internal reflection (FTIR)¹ to make the acoustic field modulate an optical beam. The OPUS allows the acquisition of an entire plane

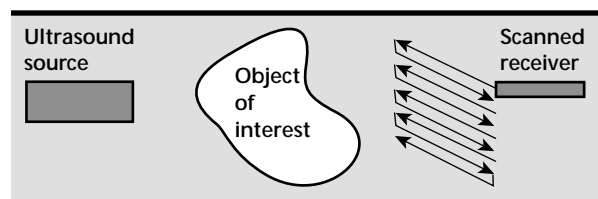


Figure 1. Transmission ultrasound imaging, currently performed using a mechanically scanned point or line sensor.

of acoustic field data at once. The OPUS has the potential to reduce the time of data acquisition by up to four orders of magnitude (see **Fig. 2**).

In FY-98 we carried out proof-of-principle research into making an OPUS. Funding was granted in FY-99 to design and fabricate the system.

The OPUS exploits FTIR: when light is incident at angle θ_1 on the interface between a slow medium (refractive index n_1) and a fast one (index n_2), light is refracted at an angle θ_2 in accordance with Snell's law², $n_1 \sin\theta_1 = n_2 \sin\theta_2$ (**Fig. 3a**). When $(n_1 \sin\theta_1)/n_2 \geq 1$, total internal reflection (TIR) occurs (**Fig. 3b**).

In TIR, 100% of the light that hits the interface is reflected. There is, however, a small evanescent wave that exists outside the high index medium. This evanescent wave falls off exponentially with distance and is almost nonexistent one wavelength beyond the interface. If another piece of high index medium intercepts this evanescent wave (**Fig. 3c**), the light is transmitted across the gap, and the TIR is frustrated (because it is no longer 100% total). The amount of light that is transmitted (and consequently the amount reflected) is very sensitively dependent on the size of the gap. By changing the gap, we can modulate the reflection of light off the TIR interface.

The heart of the OPUS is a thin silicon nitride membrane mated to an optical TIR interface by short gold walls. The membrane and walls maintain an air gap between an acoustic medium (water) and the optical interface (see **Fig. 4**). When there is no ultrasound, the membrane is still and light that hits the

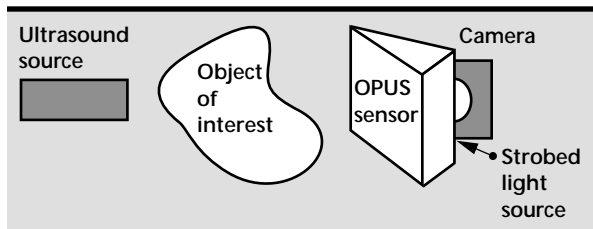


Figure 2. Illustration of the OPUS. Imaging is accelerated by acquiring the data from an entire plane of the acoustic field at once.

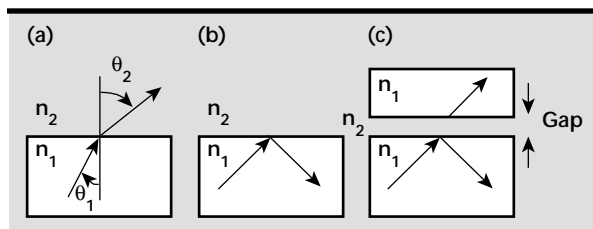


Figure 3. (a) Snell's law refraction of light from region of index n_1 to region of index n_2 ; (b) total internal reflection; (c) frustrated total internal reflection.

interface is partially reflected and partially transmitted. When exposed to ultrasound, the membrane vibrates, changing the air gap and modulating the reflected light. The gold walls divide the membrane into small acoustic pixels (60 mm on a side) that are staggered to minimize cross-talk.

Given a continuous light source we could use a photodiode to monitor the modulation of the reflected beam, but we'd need a photodiode per acoustic pixel and multiplexed electronics. An alternative is to use a strobed light source and a digital camera to take a sequence of images that allow us to extract the phase and amplitude of the vibration of the entire set of acoustic pixels. Just as a strobe light can be used to watch the vibration of a drum head, we're using a strobed source to watch the relative phases and amplitudes of tens of thousands of tiny drum heads, all at once. Given a sequence of images (ten over the course of the acoustic cycle (see **Fig. 5**)) and calibration data, we can extract the phase and amplitude of the vibration, and thus extract the pressure phase and amplitude.

The system we built to acquire these images consists of the sensor (mounted to the side of a water tank), an acoustic source, a synchronized optical source, and a digital camera (see **Fig. 6**). The main timing signal for both the acoustic and optical sources comes from the oscillator. The oscillator output is split among an amplifier, an oscilloscope, and the optical pulse generator. The output from the amplifier is fed to a power meter and then to the acoustic source transducer. The output from the pulse generator is fed to both the

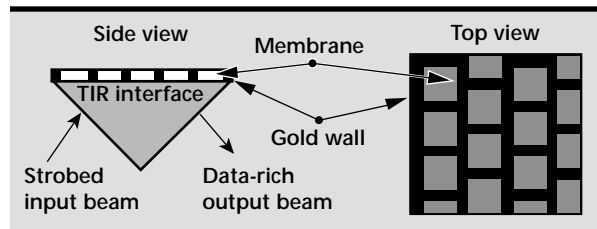


Figure 4. Structure of the OPUS, built from a silicon nitride membrane that stands over a TIR interface on short gold walls. The gold walls form staggered acoustic pixels.

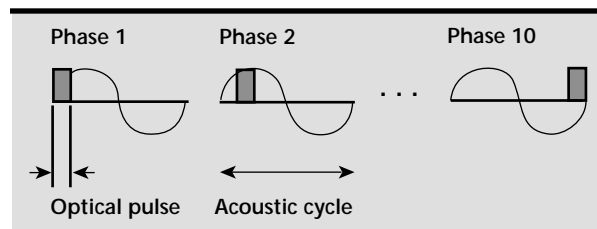


Figure 5. Sequence of images taken at ten different phases of the acoustic cycle.

LED and the oscilloscope. The light from the LED is homogenized, polarized, and collimated. It impinges on the sensor where it is modulated and then picked up by the digital camera. The digital camera data is acquired by the computer.

In a typical data acquisition session, both a calibration set (without the subject) and a data set (with the subject) are acquired. To acquire data the operator sets the oscillator frequency (nominally 1 MHz) and the amplifier gain, reads the power meter, sets the data set name into the computer, sets the phase on the pulse generator, and has the computer acquire an image. To take the next image in the sequence the user adjusts the pulse generator to put the optical pulse at the correct acoustic phase, changes the data file name on the computer, and has the computer acquire an image. This happens a minimum of ten times per image sequence. We are pursuing the automation of this process.

Progress

Working from the proof-of-principle system and data collected in FY-98 we constructed the OPUS data acquisition system shown in **Fig. 6** and used the facilities and personnel of the microfabrication group to build several sensors. Over the course of the year we experimented with the sensors, collecting data and making refinements to the sensor designs (both microstructure and macrostructure). We discovered that the membranes must be very carefully cleaned prior to sensor assembly, as any contamination larger than $0.2\text{ }\mu\text{m}$ was large enough to cause the membrane to deform around it, concentrating stress, and eventually breaking the membrane under the hydrostatic load of being immersed into the operating fluid.

We also found that the nonplanarity of the silicon wafers on which the membranes are grown can accentuate the membrane fragility. We have discovered ways to mitigate these effects. Another aspect of our work this year was the start of automating the acquisition of data. Eventually this will require the purchasing of a computer-controlled signal generator, amplifier, power meter, and pulse generator. We began the modifications to the computer program that acquires the data to minimize the human interactions during sequence acquisition.

The sensor we have been working with most recently has a 0.7 cm^2 sensing region. The image in **Fig. 7** is the result of using this sensor to look at the acoustic fields transmitted through a candle placed 2.5 cm in front of the sensor. Two sequences of data were taken, one without the candle in the acoustic path (**Fig. 7a**) and one with the candle (**Fig. 7b**). Each pixel of both sequences of data was examined to extract the amplitude of the sinusoidal variation in brightness through the sequence. The ratio of these amplitudes to their respective backgrounds gives an indication of the relative pressure at every pixel. Dark pixels occur when there is a lower relative pressure; bright pixels occur where the relative pressure is higher. The acoustic wavelength at which the data that went into this image was acquired is 1.75 mm. We expect the two images to differ in the following ways: **Fig. 7a** should show no structure, while **Fig. 7b** should show similar structure in every horizontal row (the candle was suspended vertically in front of the sensor, so we expect to see relatively constant vertical columns in the data). Of course, there are reasons to expect nonuniformity as well: nonuniformity of the source and nonuniformity of the candle (the presence of a wick) being among these.

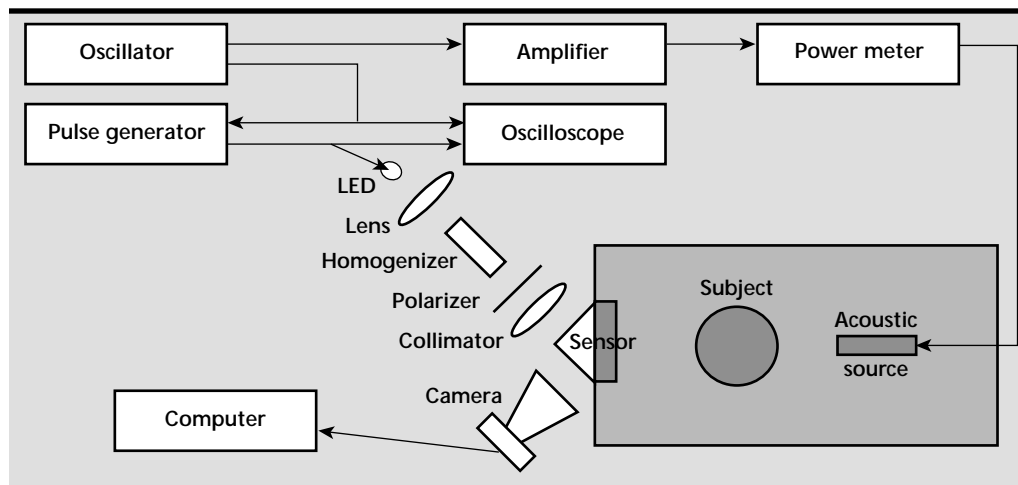


Figure 6. Schematic view of the OPUS data acquisition system.

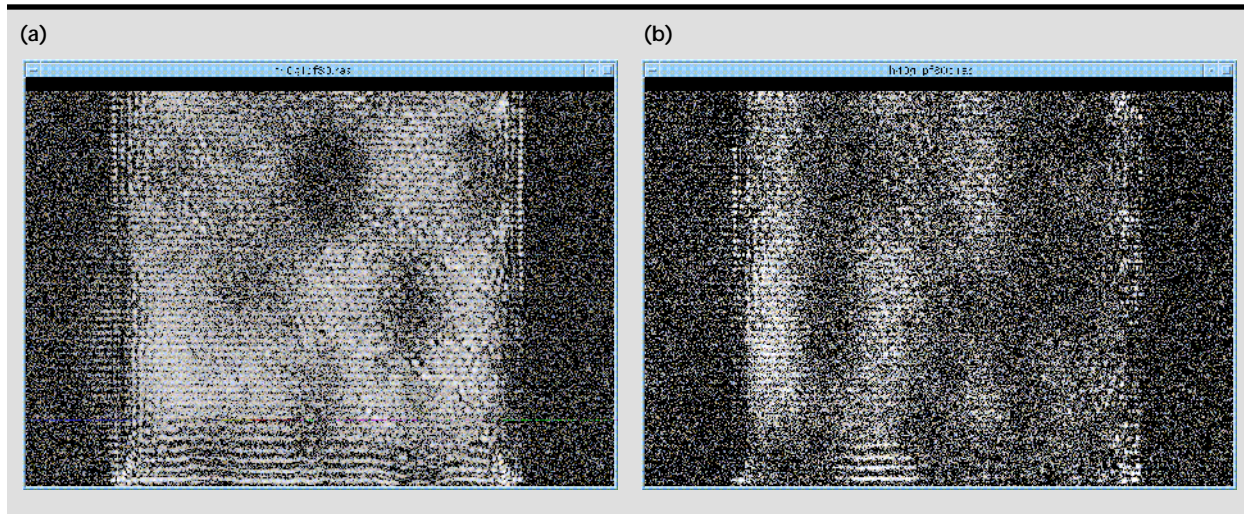


Figure 7. Relative acoustic pressure data extracted from two sequences of data images: (a) without a candle and (b) with a candle. Note that image (b) has bright vertical columns while image (a) does not.

Future Work

There has been great progress on this project in the last year, but there remain a number of challenges to make this device useful: the sensor aperture must be expanded to several times the current size, the sensor must be made more sensitive, time for data acquisition must be reduced, and the data acquisition must be automated.

We are currently looking at ways of expanding the aperture, including making mosaics of the current membranes and working with membranes set up like paned windows. To make the membranes more sensitive we are examining new membrane materials. To reduce the data acquisition time, we are examining the possibility of changing our light source and using a nonlinear optical temporal novelty filter³ to increase our signal to noise level to the point that we can use video-rate cameras. The automation of the data acquisition is perhaps the simplest problem to solve, requiring only the purchase of the computer-controlled hardware and the time to program it.

Another aspect of this work is the use of the pressure phase and amplitude information to do acoustic tomography. This is the great promise of the technology: that hitherto infeasible acoustic inspections will become commonplace. At this point much work needs to be done on the algorithms to do these reconstructions.

FTIR has been harnessed to allow acoustic pressure to modulate optical beams. These beams are acquired one plane at a time. Optically-strobed sequences of images acquired in this manner allow the extraction of relative pressure phase and amplitude. This technology promises to revolutionize transmission acoustic imaging, allowing near real-time imaging of 2-D projections, and fast data acquisition for volumetric image processing.

References

1. J. Strong (1958), "Concepts of Classical Optics," W. H. Freeman and Company, Inc., New York, New York, p. 124.
2. F. A. Jenkins and H. E. White (1950), "Fundamentals of Optics," McGraw-Hill Book Company, Inc., New York, New York, p. 5.
3. G. F. Albrecht, H. F. Robey, and T. R. Moore, "An optical technique for the measurement of turbulent spectra using the photorefractive properties of BaTiO_3 ," Lawrence Livermore National Laboratory, Livermore, California (UCRL-102551).

peckle Reduction for LIDAR Using Optical Phase Conjugation

Mark W. Bowers
Defense Systems Engineering Division
Electronics Engineering

We are developing a novel method for increasing the accuracy and expediency of remote detection LIDAR (light detection and ranging) systems. Laboratory and numerical studies have shown that it is possible to increase the signal-to-noise (S/N) ratio for LIDAR systems under certain conditions using optical phase conjugation. This increase in S/N results in more accurate detection of chemical effluents while simultaneously reducing the time necessary to acquire this information. Research has shown that it is possible to expand this work into the near- and mid-infrared regime, two regimes that are commonly used for remote detection by LIDAR. Bulk phase conjugate systems as well as liquid and solid waveguides have been studied for their viability in this application.

Introduction

Remote detection systems can be used to monitor dangerous chemical spills as well as environmental conditions around the world. It is imperative that these detection systems work reliably and accurately while being as distant from the source as possible. It would be advantageous if, in addition, the remote detection systems were compact and consumed little power so that they could be carried in smaller vehicles, planes, or spacecraft. LIDAR (light detection and ranging) is well suited for these applications. A LIDAR system is one in which a laser beam is transmitted out towards an area to be probed. The return scatter from the aerosol itself or the topographic background is detected and measured.

LIDAR systems can measure chemical effluents accurately by using a detection technique known as differential absorption LIDAR (DIAL). In the DIAL technique two or more laser pulses of different frequencies are transmitted sequentially towards a target area. The differences in return signal power for each of these frequencies are measured. Since it is assumed that the returned power would be identical for all frequencies in the absence of absorption, this differencing technique can determine the relative absorption at the transmitted frequencies.

In practical, field operational systems, the simplistic view given above is complicated by noise sources, such as speckle. Speckle, as shown in **Fig. 1a**, results from the light scattering off a diffuse surface.

The light returning to any one point in the detector aperture will originate from multiple points on the diffuse surface. Each of these individual light rays will add constructively or destructively with its own phase. The random phases of each light ray will result in a random, but deterministic, light irradiance at each point in the detector aperture. If viewed with a camera, this pattern will appear as bright and dark spots (**Fig. 1b**).

The exact number of bright and dark spots in the detector aperture is a random number, although the mean value and variance can be calculated for a given situation. Thus, the total irradiance measured by the detector is random, resulting in an unknown deviation from the expected signal return. The atmosphere will complicate even this picture by adding turbulence that can change the speckle return over time, usually over a few milliseconds time period.

In current field operating systems, the noise contribution by speckle and atmospheric turbulence can be reduced significantly, but at a cost. The mean and the variance of the signal are deterministic, and thus can be reduced by averaging. Averaging can improve the S/N by an amount proportional to the square root of the number of pulses averaged. Since each pulse must wait at least long enough for the speckle field to change, the time between pulses will be on the order of milliseconds. In order to get adequate results, averaging times of seconds or minutes may be necessary. The maximum averaging

time is also limited by slow system drifts and will limit the accuracy of the resultant measurements to something well below that which is necessary to complete the desired mission.

Optical phase conjugation is a nonlinear optical method of removing the phase differences of the diffuse rays of light described above. By removing the phase differences the light can be made to add constructively over the entire detector aperture, thus removing the presence of a speckle pattern and the associated noise. For optical phase conjugation to completely compensate for the speckle noise, all of the light over 2π steradians must be collected and conjugated. This is not possible for LIDAR systems due to the large distances between the LIDAR source and the topographic background.

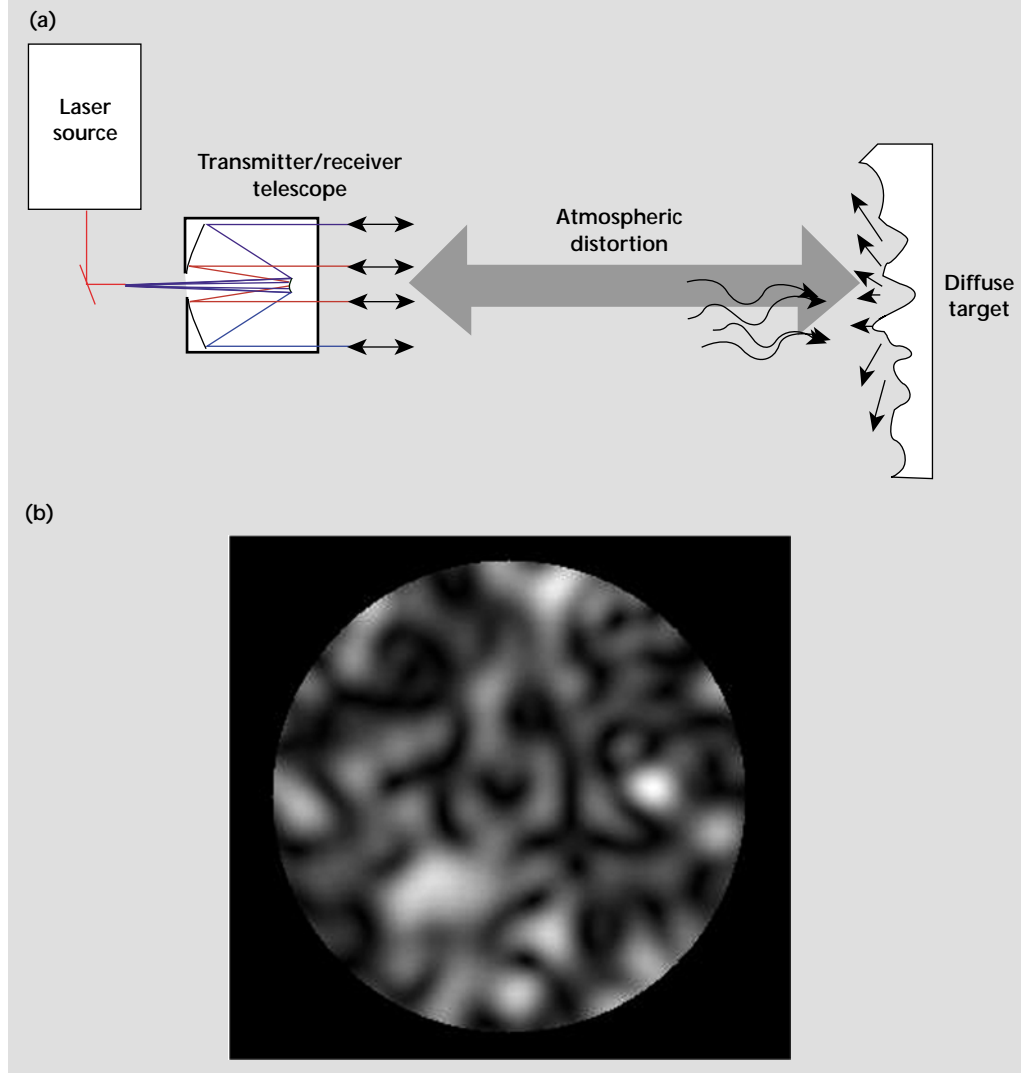
Previously it was generally accepted that capturing only a portion of the scattered light would reduce or completely null out the effects of

optical phase conjugation. This belief was based on the premise that microscopic scattering dominates the phase-front of the optical beam propagation. Unpublished numerical studies have shown that the macroscopic scattering properties of a surface can be just as important in the wavefront evolution. Microscopic and macroscopic here refer to feature sizes smaller than or larger than the diffraction limited optical spot sizes, respectively. This project is intended to show that it is possible, under most normal LIDAR operating conditions, to use optical phase conjugation to mitigate the effects of speckle.

Progress

Stimulated Brillouin Scattering (SBS) was chosen as the nonlinear process to achieve the optical phase conjugation for a variety of reasons. The properties of SBS have been studied extensively,

Figure 1. Speckle.
(a) Laser light reflecting off a diffuse surface. The received image of the laser spot on the diffuse surface is as shown in (b), not a single spot as would be expected with incoherent light.



resulting in a wide information base on which to build. Two notable works are by Bruesselbach *et al.*¹ for atmospheric turbulence compensation and Delaye *et al.*² where SBS is used for optical phase conjugation of a diffuse optical field. Other advantages of SBS include conjugator response times faster than that of atmospheric turbulence, high gains (single stage gains of >80 dB have been demonstrated³) that can overcome the losses in propagating over large distances. Another important fact about SBS is that it has been widely used with the LIDAR laser systems, thus making retrofitting existing LIDAR systems simpler and less costly.

The main goal in this first year of the project was to demonstrate the technical feasibility of using optical phase conjugation to reduce the undesirable effects of speckle. The first step toward this goal was to perform a numerical study to show what regimes, both in fieldable systems and in laboratory experiments, would benefit from this new technology. The optical fields were modeled using the analytical software package "MatLab" in a manner consistent with current LIDAR simulation programs. Representative results from this numerical study are shown in **Fig. 2** for a field LIDAR system. The 10-km distance to the topographic background and the 1-m-aperture detector resulted in a loss of 70 dB in the return signal information and power, not normally a regime in which optical phase conjugation is considered practical. From this numerical study it was determined that the quality of the phase conjugation process is directly dependent upon the number of speckle bright spots, called speckle cells, in the detection aperture.

A laboratory experiment was planned that would closely approximate an outdoor field LIDAR system. A numerical study was performed using MatLab to ensure that the detection aperture would have

adequate phase conjugation quality, determined mainly by the number of speckle cells in the collection aperture. Usually more than 20 will suffice. The number of speckle cells is a controllable parameter determined only by the characteristics of the LIDAR itself, not by the properties of the target used.

The experiment was planned using a Nd:YAG laser system and a CS₂-filled cell as the nonlinear SBS material. The results of this initial experiment, **Figs. 3a** and **3b**, showed that the SBS process significantly improved the quality of the scattered light. The single pulse S/N improvement for this system was 100:1 and the multiple pulse S/N improvement with averaging was 9.3:1. The SBS gain was 10 dB, lower than estimated above due to the bulk focusing optics used, but adequate for the laboratory testing used here. Although good, the results were less than expected from the numerical studies performed earlier. The problem was found to be in the geometry of the SBS phase conjugator.

Although the geometry is the one most commonly used for SBS phase conjugation, it was not appropriate for fields with a large number of speckle cells. The geometry prevented light rays that were entering at extreme angles from participating in the phase conjugation process. Thus, some of the information was lost and incomplete phase conjugation resulted. We were able to reproduce this effect numerically, as shown in **Figs. 3c** and **3d**.

Waveguides, which can capture the light rays that enter at extreme angles, were the solution to this problem. The waveguides are cylindrical pipes or fibers that are filled with an SBS active material. Liquid and solid filled waveguides were tested. The liquid filled waveguides did have good phase conjugation properties. These waveguides, however, suffered from heat buildup near the entrance that created bubbles after several minutes of operation.

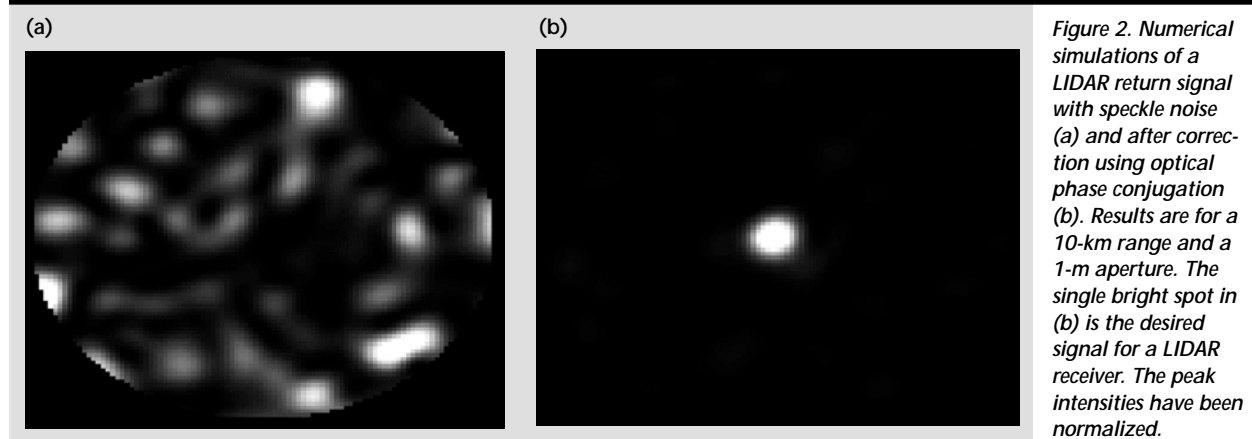


Figure 2. Numerical simulations of a LIDAR return signal with speckle noise (a) and after correction using optical phase conjugation (b). Results are for a 10-km range and a 1-m aperture. The single bright spot in (b) is the desired signal for a LIDAR receiver. The peak intensities have been normalized.

The bubbles would be drawn into the waveguide, stopping the SBS process. This problem can be corrected by flowing the liquid continuously through the waveguide, removing bubbles whenever they form.

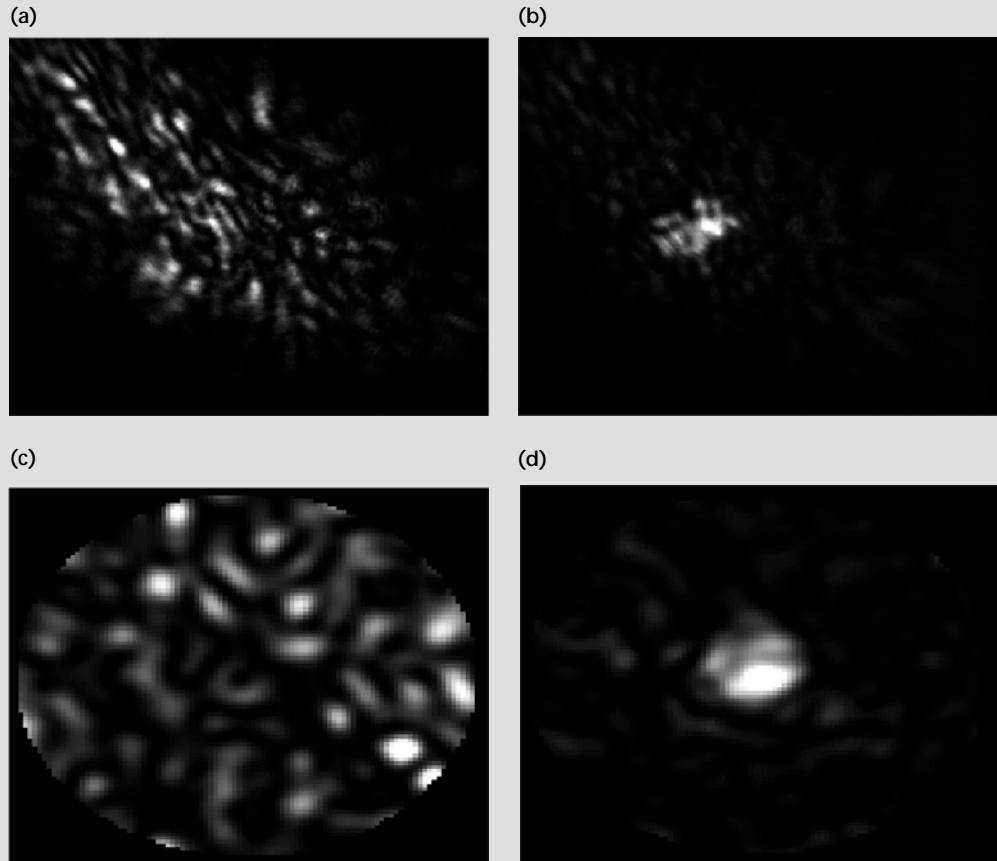
The solid waveguides are essentially optical fibers that are specially shaped to enhance the SBS process. These waveguides have similar phase conjugation properties to those of the liquid filled counterparts, but do not suffer from the bubble formation. For the incorporation of the waveguide SBS generators into a LIDAR system it is essential that they reach SBS threshold well below the power levels available. Since the power available is approximately 600 μJ for the oscillator/generator, the threshold should be below 100 μJ to achieve adequate conjugate intensity. Low thresholds for SBS initiation, as low as 70 μJ , were demonstrated as part of this project thus far. This is an enhancement over the original bulk CS_2 cells that had a threshold of more than 2 mJ.

The maximum power permissible in the fibers tested is limited to twice the threshold value, too low to yield sufficient energy for the speckle correction

testing. New fibers that have an improved geometry for SBS enhancement have been ordered. The threshold for these new fibers has been calculated to be better than 10 μJ with a maximum of power of several millijoules.

A collaborative effort, funded through this project, was undertaken with the nonlinear optics group at the University of Rochester, to search for appropriate materials for the SBS process in wavelength regions of interest to most commercial DIAL systems. The most desirable wavelength region is that from 2 to 4 μm . A table of more than 100 suitable materials was found and narrowed down to the best candidates. From this list it was evident that commercially available infrared (IR) fibers would be suitable candidates due to their availability in a waveguide form. IR sapphire fibers can be commercially manufactured to our desired geometry while maintaining a high damage threshold. Tests were performed at the University of Rochester on the SBS process in sapphire fibers to determine the optimum geometry. More tests are needed on these fibers to determine if they can work with the short pulses delivered by the LIDAR system.

Figure 3. Experimental results for our laboratory prototype system, showing speckle noise (a) for a LIDAR return signal, and significantly better signal quality (b) after the incorporation of the optical phase conjugation. Images (c) and (d) are the numerical simulations of (a) and (b), respectively. In image (d) the effect of losing the extreme rays is taken into account. The peak intensities in (b) and (d) have been attenuated by 30 dB for display purposes.



Summary

Although previously thought impractical, numerical and experimental evidence in this project suggest that optical phase conjugation can significantly improve the S/N for LIDAR systems. Numerical simulations show that ideal phase conjugation can lead to improvements in the S/N for real world LIDAR applications. The laboratory experiments have also demonstrated large improvements in the S/N, although less than ideal due to extreme optical rays. This data is supported with numerical simulations attenuating the extreme rays. New fiber designs and materials are being studied that will significantly improve the properties of the system.

Future Work


In the second year of this project the useful energy range of the SBS fiber phase conjugators will need to be expanded. Fibers are on order that should have the energy range and wavelength range desired for the laboratory experiments. The initial testing of these fibers will be done with the Nd:YAG laser.

Finally, a field demonstration of a DIAL that will be retrofitted with the SBS optical phase conjugation system is planned. We plan to do minimal alterations to the existing LIDAR system, thus choosing the correct SBS material for the phase conjugator is paramount. This particular LIDAR has 5-ns optical pulses at a wavelength of 1.5 μm . The material chosen must have a phonon decay time of <5 ns and be transparent at that optical wavelength. The phonon decay time of sapphire is currently unknown and

will need to be measured using the laser system in the LIDAR itself. If the sapphire fiber proves to be too slow, a liquid with a fast phonon decay time, such as freon-113 in a waveguide geometry, may be used or the pulse length of the laser will need to be lengthened.

The field demonstration will show the increase in the S/N of a DIAL system in a real environment. The first field demonstration will take place using a specular target at a distance of 700 m. This test will be used to work out the bugs in the system and demonstrate the quality of the optical phase conjugation as incorporated into the DIAL system. The next test will use a diffuse target in place of the specular target at the same range. An increase in the S/N of just three in this test will prove to be an order of magnitude reduction in the averaging time needed for this DIAL to perform its intended functions.

References

1. H. Bruesselbach, D. C. Jones, D. A. Rockwell, R. C. Lind, and G. Vogel (1995), "Real-time atmospheric compensation by stimulated Brillouin-scattering phase conjugation," *J. Opt. Soc. Am. B.*, Vol. **12**, pp. 1434-1447.
2. P. Delaye, A. Blouin, D. Drolet, and J. Monchalin (1995), "Heterodyne detection of ultrasound from rough surfaces using a double phase conjugate mirror," *Appl. Phys. Lett.*, Vol. **67**, pp. 3251-3253.
3. A. M. Scott and K. D. Ridley (1989), "A review of Brillouin-enhanced four-wave mixing," *IEEE JQE*, Vol. **25**, pp. 438-459. 



valuation of an Amorphous-Silicon Array for Industrial X-Ray Imaging

Kenneth W. Dolan, Clinton M. Logan, Jerry J. Haskins,
and R. Derrill Rikard

*Manufacturing and Materials Engineering Division
Mechanical Engineering*

Daniel J. Schneberk

*Computer Applications Science and Engineering Division
Computation Organization*

We are evaluating flat panel imagers, both amorphous silicon and amorphous selenium, for use as imaging elements in digital radiography and computed tomography (CT) systems. Digital radiography systems are being developed for applications where the digital image format and fast image acquisition provide an advantage over film, and where image quality and dynamic range requirements can be satisfied. CT systems based on the flat panel technologies are being developed as a means of improving the speed of image acquisition and image quality when the field of view is greater than 5 or 6 in. on a side. Results of evaluations and applications of amorphous-silicon flat panel imagers are reported here.

Introduction

The results of the amorphous-selenium (a-Se) work were reported by us last year¹ and appear elsewhere.²⁻²⁶

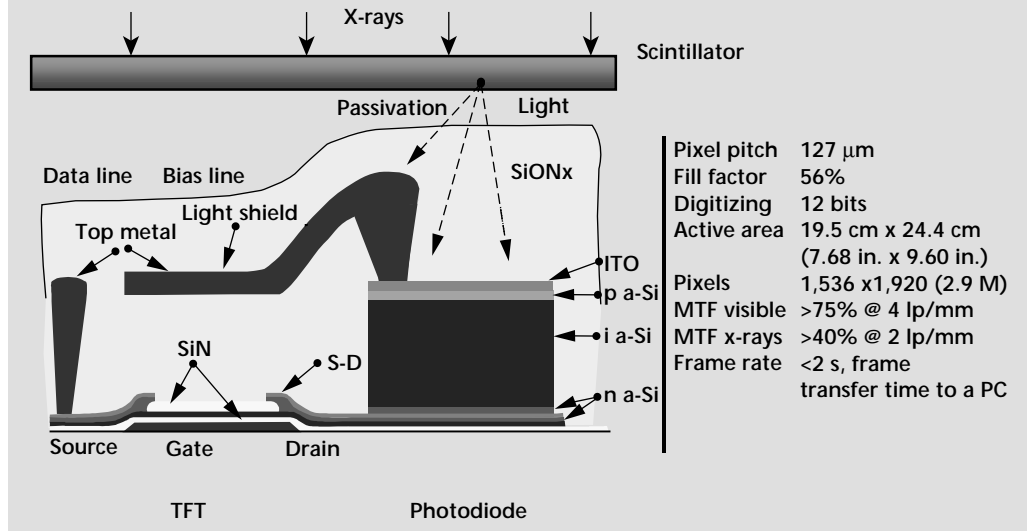
The Flashscan 20, a large flat panel amorphous-silicon (a-Si) x-ray imaging array made by dpiX, Incorporated, Palo Alto, California, was used in the present digital radiography and computed tomography (CT) application evaluations. The sensitive area of the array is 195 mm \times 244 mm (7.7 in. \times 9.6 in.), pixel dimensions are 127 μ m \times 127 μ m (0.005 in. \times 0.005 in.) with 1536 data lines by 1920 gate lines, resulting in 2.95×10^6 pixels.²⁷ The array incorporates charge sensitive amplifiers and 12-bit A/D converters, but the useful dynamic range is approximately 11 bits.

The a-Si array converts light images into electrical charge, pixel by pixel. The light images are produced by x-ray interactions in a scintillating screen placed in intimate contact with the a-Si array. The construction of the array (**Fig. 1**) consists of a thin film a-Si over a large area glass substrate. Photodiodes (n-i-p) made from the a-Si thin film layer convert light energy into electrical energy, and thin film transistors serve as pixel switches. The scintillating screen can be selected to provide an optimal configuration for

image acquisition speed, contrast sensitivity, spatial resolution, and source energy.

The a-Si flat panel arrays are suitable for radiographic imaging applications because the photodiodes have good light sensitivity (for example, quantum efficiency at the visible wavelengths is approximately 70%), and low dark current. Fill factors for the sensitive area can be made sufficiently high (57% with the present panel), and photocurrent decay times are sufficiently long to allow readout without loss of signal. In the readout operation, the gate lines are switched on sequentially, and the charge stored in the associated row of photodiodes is transferred to parallel data lines for readout by a bank of amplifiers. The amplifiers read the charge signals in parallel, and then output them sequentially as analog voltage signals to A/D converters. The digital image is typically corrected for offset and gain variations, and interpolations are performed for defective pixels.

With this protocol the x-ray source can be operated in the continuous exposure mode for image acquisition. In this mode the array is acquiring data *during* the readout cycle. Readout time is 1.6 s. Exposure is added to this in 0.1- or 0.2-s increments to provide up to 4.8 s exposure per frame, as shown in **Table 1**.

Figure 1. Schematic of dpi_x a-Si array.

The disadvantage of this is that variations in source intensity during the readout cycle will affect the data. For this reason source stability checks must be made before and after each image, using at least two unattenuated beam (I_0) regions in the image.

Progress

Calculated X-Ray Spectra

X-ray exposures were obtained with a conventional x-ray tube with maximum operating potential 450 kV, beryllium tube window, and focal spot of 1.0 mm. Filtered and unfiltered source spectra for

this tube were calculated using Tubdet²⁸. Results of these calculations are shown in **Figs. 2** through **4**. The calculated unfiltered spectra are shown in **Fig. 2** for x-ray tube operating potentials 120, 250 and 450 kV-peak (kVp). The characteristic $K\alpha$ - and $K\beta$ -fluorescence lines from the tungsten anode are apparent at 58.8 kV and 67.6 kV, but are clipped in these figures to allow display of the continuum spectrum. Unfiltered spectra are commonly used at lower operating potentials for radiography of thinner, lower atomic number materials to obtain the highest contrast sensitivity where latitude (that is, ability to image a range of thicknesses in a test object) is not an important consideration.

Table 1. Integration time options for dpi_x array.

Switch setting	Delay (s)	Readout (s)	Total
0	0.1	1.6	1.7
1	0.2	1.6	1.8
2	0.4	1.6	2
3	0.6	1.6	2.2
4	0.8	1.6	2.4
5	1	1.6	2.6
6	1.2	1.6	2.8
7	1.4	1.6	3
8	1.6	1.6	3.2
9	1.8	1.6	3.4
10	2	1.6	3.6
11	2.2	1.6	3.8
12	2.4	1.6	4
13	2.6	1.6	4.2
14	2.8	1.6	4.4
15	3	1.6	4.6
16	3.2	1.6	4.8

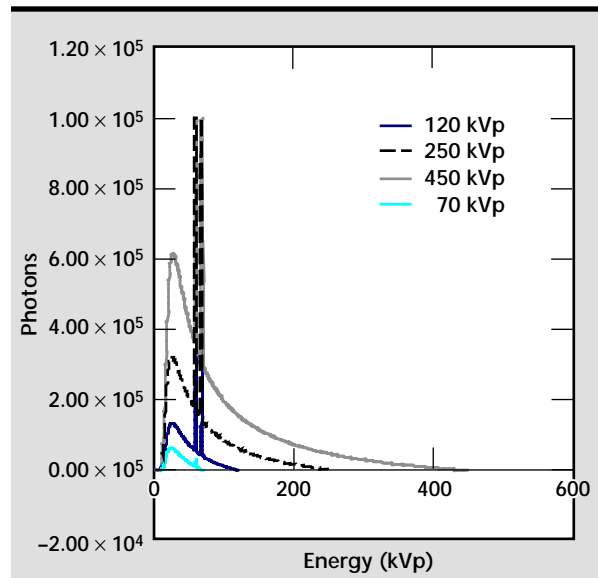


Figure 2. Calculated x-ray source spectra, unfiltered, at operating potentials of 70, 120, 250 and 450 kVp.

The calculated output spectra as filtered by 0.076 mm (0.003 in.) tungsten at 120 kVp, 3.2 mm (0.125 in.) copper at 250 kVp, and 6.5 mm (0.25 in.) copper at 450 kVp are shown in **Fig. 3**. Filtered spectra are commonly used at higher operating potentials for radiography of thicker, higher atomic number, or higher density materials to increase latitude and reduce scatter. A comparison of the filtered and unfiltered spectra at 120 kVp is shown in **Fig. 4** to indicate the reduced intensity in the low energy portion of the spectrum, and the reduced overall relative intensity. A step intensity change in the spectrum associated with the K-absorption edge of the tungsten filter at 69.5 kV is also apparent in **Fig. 4**.

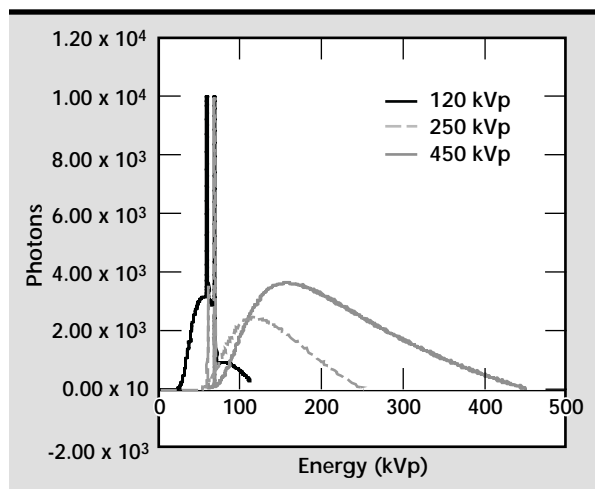


Figure 3. Calculated x-ray source spectra filtered by 0.076 mm W at 120 kVp, 3.2 mm Cu at 250 kVp, and 6.5 mm Cu at 450 kVp.

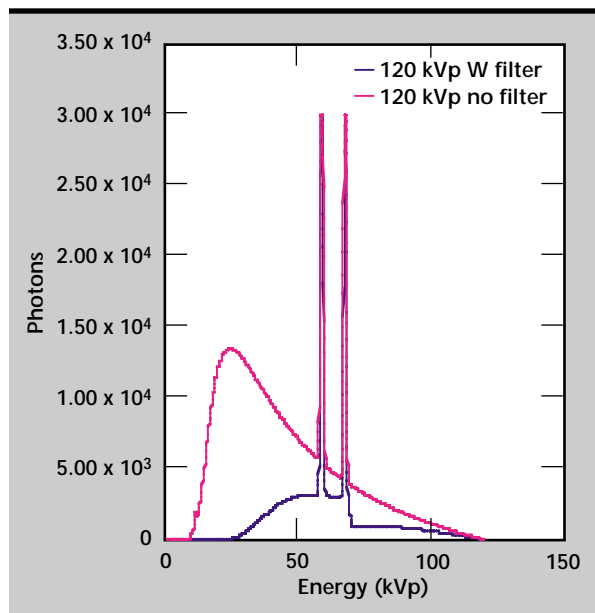


Figure 4. Comparison of calculated filtered and unfiltered x-ray source spectra at operating potential 120 kVp showing difference in low energy content.

Shielding

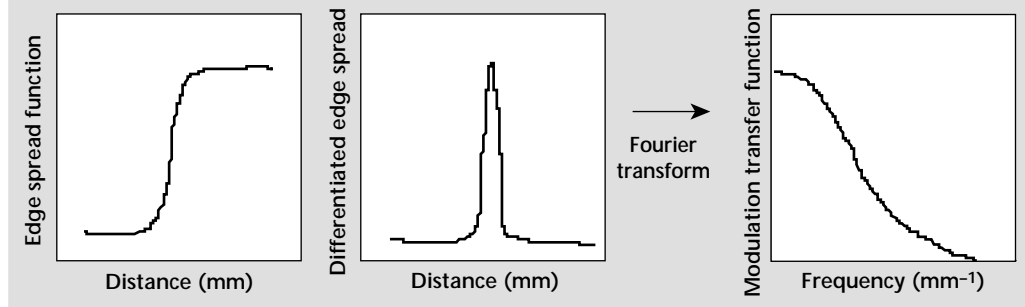
The a-Si array itself is not easily damaged by radiation exposure,²² but electronic read-out components adjacent to the array within the panel enclosure are susceptible to radiation damage. The threshold for damage of these components is not known, and it was not the purpose of these tests to determine the threshold and thereby disable the panel. A short exposure x-ray image of the panel was taken to determine the location of sensitive components, and lead shielding was positioned to protect these components. The damage threshold for many electronic components is 1 krad of exposure, so lead shielding was sized to reduce accumulated exposures to below this level. This consisted of 6 to 12 mm of lead with the 450-kVp conventional x-ray tube source, and up to 50 mm of lead for the 9-MV linear accelerator. In addition, 150 mm of tungsten collimation limited the x-ray beam to the area of the panel for the 9-MV images.

Geometric Unsharpness

Unsharpness in the radiographic image that results from the geometric arrangement of x-ray tube, test object, and imager is always a concern when attempting to obtain best resolution. Geometric unsharpness (U), is given by the relationship $U = F \cdot T / D$ where F is the x-ray source focal spot diameter, T is the object-to-imager plane distance, and D is source-to-object distance.

In the present case, the a-Si array is separated from the front cover surface of the flat panel assembly by no more than approximately 6 mm (0.25 in.). This gives a U of 0.006 mm with the conventional x-ray tube using 1.0 mm focal spot, source-to-object distance 1 m, and object positioned directly against the front surface of the panel. This is only a small fraction of a pixel size, 0.127 mm, and is therefore not a contributor to degraded resolution for thin or small diameter objects. Geometric unsharpness that would contribute to degraded resolution comes from values of U that are a significant fraction of a pixel size, such as more than one-half pixel dimension or 0.06 mm. This condition would occur for an object-to-imager separation, or object cord length of more than 50 mm, given 1.0 mm focal spot and 1 m source-to-object distance. Acceptably small U for larger diameter objects, or larger object-to-imager separations, are obtained by increasing source-to-object distance with considerations of reduced x-ray intensity at the imager due to the larger source-to-imager distance.

Figure 5. Principle of the edge-spread function in determining the modulation transfer function.



Modulation Transfer Function

The modulation transfer function (MTF) describes contrast transmission as a function of feature size. It is a function that is sensitive to all the elements of an imaging system that contribute to image unsharpness, and provides a practical measure of the capability of an imaging system to distinguish features of various sizes. One method for obtaining an MTF is to determine the edge spread function. This is done by obtaining the image of a totally absorbing object that has a sharp edge, such as a thin parallelepiped block, where the edge surface is positioned parallel to the centerline of the x-ray beam. In our case, a thin right parallelepiped tantalum block was positioned against the front panel of the a-Si imager on the centerline of the x-ray beam. A line trace of the image intensity across the edge is obtained, and then the differential of this trace is determined (see **Fig. 5**). The differential trace can be fit to a Gaussian or multiple Gaussian functions to model the peaks and tails to eliminate noise variations. The MTF is then obtained as the normalized magnitude of the Fourier transform of the differentiated edge spread function (see **Fig. 5**), and has units of spatial frequency, such as mm^{-1} or line pair/mm (lp/mm).

Calibrating the dpi χ Array

To use the output of the Flashscan 20 flat panel array for quantitative digital radiography and CT we have calibrated raw panel output to a scale that is roughly linear with x-ray intensity. The procedure we have developed differs somewhat from the approach put forth by dpi χ , but is similar in concept. Both procedures derive from the intrinsic properties of the panel as it responds to radiation.

The raw image from the Flashscan 20 flat panel array contains many features characteristic of the construction of the array, and the way in which the a-Si responds to scintillation light. **Figure 6** is an image of a “dark-field,” the image of the panel with no x rays impinging on the detector. Unlike a CCD-based imager,

or an image intensifier, dpi χ has chosen a convention such that pixels in the detector start at the maximum value, somewhere between 3700 and 4000. Notice the differences in digital values for the horizontal bands across the image.

The Flashscan 20 array is put together in 128 pixel row elements, which are then combined to make the full panel. There are small gain and offset variations between the bands as observed in **Fig. 6** where the gray scale lookup table has been set to emphasize these variations. There is a slight banding in the other direction. In addition, there is a small additive bias across the panel. While not as visible in the reduced image in the figure (resampling was required to get the image onto the page), a number of bad pixels (pixels which have a poor or unusual impulse response) are also a part of the panel.

Figure 7 is an image of the “light-field” of the panel acquired at 9 MV at a source-to-imager distance of 6 m. The acquired image appears darker with increases in scintillation light. The features related to the bands are present for increased intensity, although the relative response of each band is a bit different. One band may be close to saturation (very dark), while an adjacent band is up to 500 counts lighter. Consequently, the dynamic range of each bank is different.

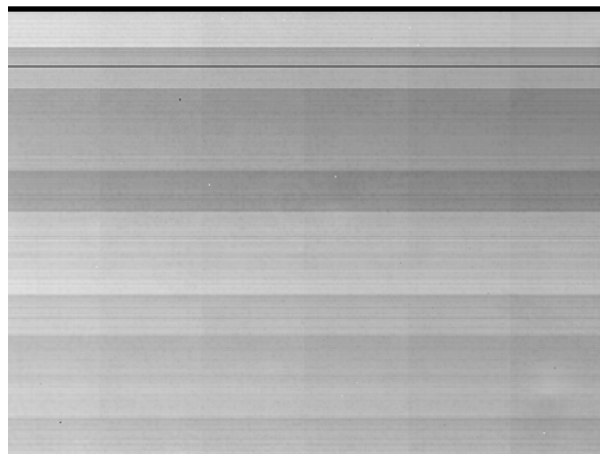


Figure 6. The “dark field” image of the 8-x-10 Flashscan 20 array.

In evaluating individual pixels, it was clear that the response is not linear over the number of possible digital levels. The pixels respond to the scintillation light by losing digital counts, and it is this change which is the digital record of the x-ray image. To evaluate the change in intensity per pixel we have re-normalized the digital levels to be dark field minus signal. **Figure 8** plots the re-normalized digital readout for 3 pixels in the same bank, and **Fig. 9** shows similar data for 4 pixels in a different bank.

Notice the small but significant nonlinearity in the response of the pixels as the panel detects more scintillation light. This effect gets more pronounced for normalized counts greater than 3400. There is a transition in the linearity of the scale for this array, which takes place at about 2000 to 2200 normalized counts (mid-field signal). Another transition takes place at 3300 to 3400 normalized counts (dark-field signal). Dpix does not recommend attempting to calibrate using intensity values greater than 3400. In addition the values in the unnormalized light-field should not be lower than 500 for the lowest valued bank.

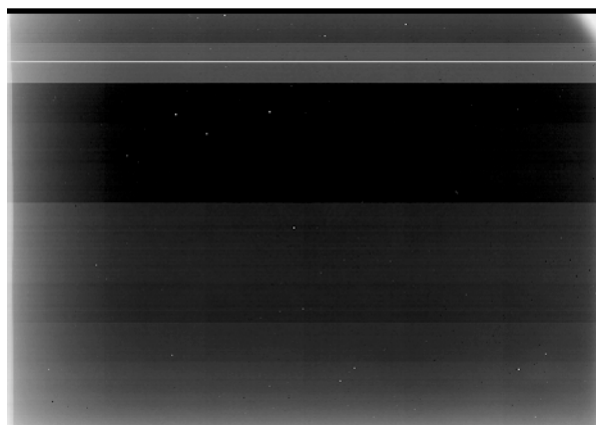


Figure 7. The "light-field" image of the 8×-10 Flashscan 20 array. The light outer boundary on the left side and at the upper right of this image is collimator cutoff.

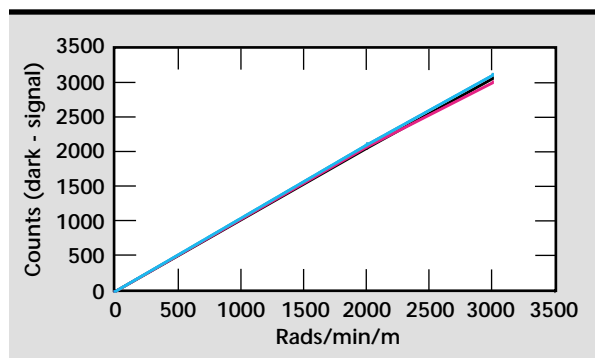


Figure 8. Flashscan 20 panel counts vs radiation intensity for 3 pixels in the same bank.

To produce images that equilibrate the effects of banding, account for the small bias, and correct for the other effects in the raw panel images, dPIX has developed a "two-gain-factor" approach for the a-Si array. First they acquire a light-field image with no bank lower than 500 counts. Then they acquire a mid-field image at somewhere between 2200 and 1200 (50 to 80% change in digital counts from the light field). Finally they acquire a dark-field image. From the three images they calculate two gain coefficients (one from dark and mid, one from mid and light). The gain coefficients are applied per pixel as the raw pixel signal value falls into the dark-mid or mid-light range.

For compatibility with current medical inspection practice, the method chosen by dPIX results in digital images calibrated to look like film (low digital values where there is high intensity, and high digital values for low radiation intensity). Values at high and low ends of the digital scale are clipped to enable the best viewing of the object. For CT applications, we prefer the raw images be calibrated to a scale that is the reverse of film (high digital values where there is high intensity, and low digital values where there is low intensity). An additional requirement for CT is that the digital values not be clipped to some value at either the high or low end of the digital scale. Consequently, we developed a calibration technique that uses the basic scheme of the dPIX approach, but by using the re-normalized data puts the data on a positive scale.

For both approaches bad pixels are handled in a similar fashion. Once a pixel is determined to be bad it is replaced by the average or median value of adjacent good pixels. The dPIX software finds bad pixels with the dark-field image, identifying those locations that have values below a certain level. We are just as concerned about pixels that read too high, as about those that read too low. Consequently, we use the mid-field image and identify bad pixels as those that are different from

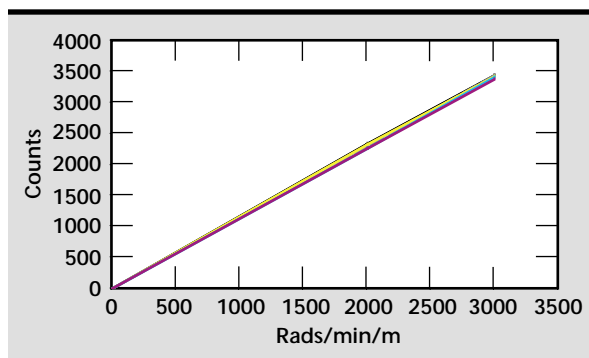
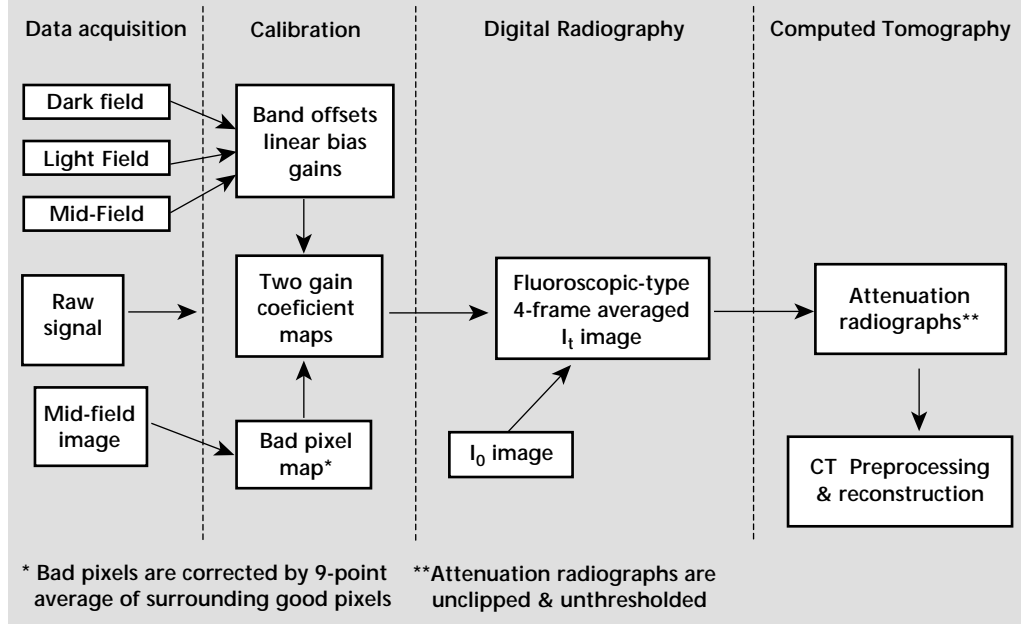


Figure 9. Flashscan 20 panel counts vs radiation intensity for 4 pixels in the same bank.

Figure 10. Block flow diagram of the data processing protocol for digital radiography and CT with the dpiX flat panel imager.



a median of the neighborhood by certain value. We use the median of the good adjacent pixels as the best estimate of the bad pixel replacement values. The use of the median value is part of our attempt to do better at bank boundaries. We also routinely acquire an I_0 image that is the detected level of the radiation without the part in the field of view, and use this image to further process out small offsets in the images. The I_0 image is also important for calculating attenuation radiographs, a necessary step for subsequent CT pre-processing and reconstruction. The processing protocol we use is shown in **Fig. 10**.

Our calibration produces images in counts, which are larger with higher x-ray intensity, and smaller with lower intensity. **Figure 11** (by permission of Ford Motor Company, Dearborn, Michigan) is a calibrated image of a Ford prototype clutch retainer acquired at 4 MV with the dpiX panel. **Figure 12** contains a CT slice from the 3-D CT volume using the calibrated data and rotation-only scanning. The CT slice shows the inner detail of a 150- μm slice of the laser weld joint. A small cupping artifact is present in the data, which is a result of beam hardening. Otherwise, the data is an accurate representation of the internals of this object. The artifact content in CT reconstructed images grows with the proportion of nonlinear effects in the input digital imagery. These CT data and other scans attest to the roughly linear character of the calibration scheme we have developed.

Evaluation Process

Our evaluation process included a study of scintillation screens, plain glass, and bare metals to determine their potential as image forming elements, producing either visible light or secondary electron emission. We determined the MTF by the absorptive edge method at a number of different x-ray energies, including both unfiltered and filtered spectra at 120, 250, and 450 kV, and 4 and 9 MV. Spatial resolution for the unfiltered spectra at 120, 250, and 450 kV was also determined using a diverging line pair gauge. Contrast sensitivity and

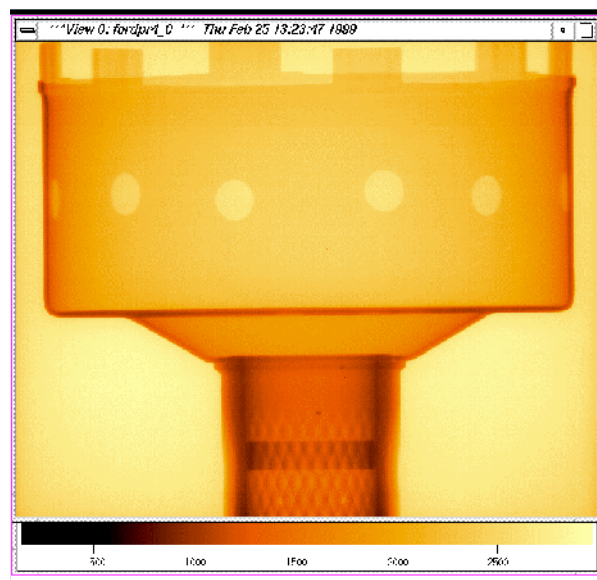


Figure 11. Calibrated image of Ford prototype clutch retainer housing (by permission of Ford Motor Company, Dearborn, Michigan).

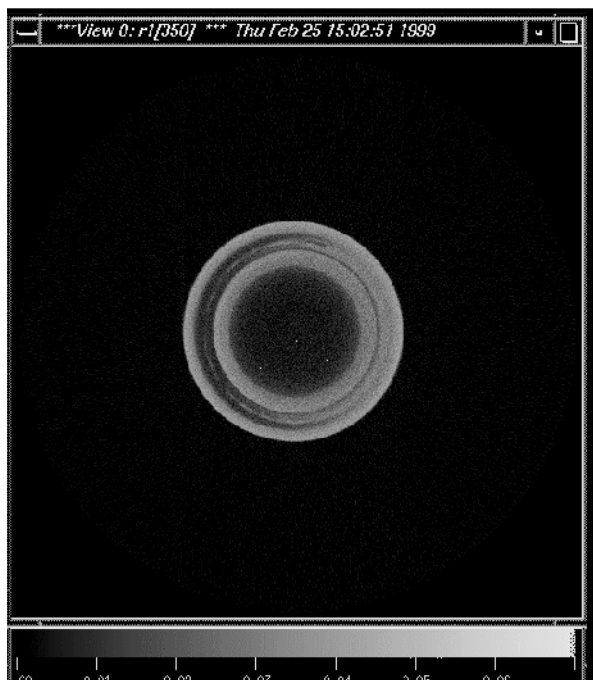


Figure 12. CT slice at laser weld joint of Ford prototype clutch retainer housing (by permission of Ford Motor Company, Dearborn, Michigan).



Figure 13. Photograph of test setup. The metal plates are not visible.

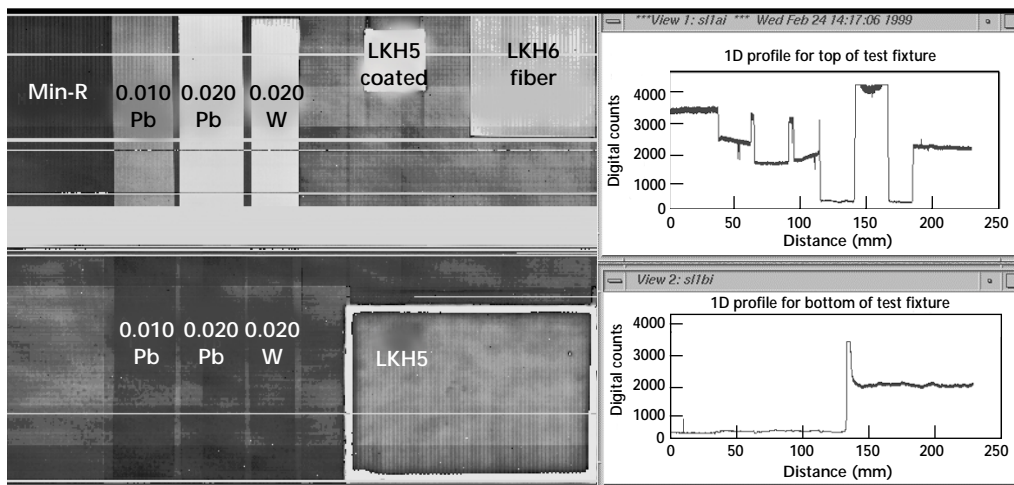


Figure 14. Digital image and horizontal lineouts of image.

latitude were determined with step wedges of various materials. Dark current, image reproducibility, dynamic range, image acquisition speed, throughput, potential for latent image formation, and corrective measures for source instability were also addressed.

Results

A number of different materials—gadolinium-oxyulfide (GdO_2S_2) particulate scintillator screens, high-Z metal sheets, two scintillator glass plates, and a scintillator glass fiber optic plate—were configured with the Flashscan 20. The particulate screens are commercial products composed of GdO_2S_2 powders of different sizes, binder, dyes, and coatings on a plastic substrate. The two scintillating glass plates are commercial, terbium-doped clear glass. One plate had no surface coating and the other had a mirror coating on one side and an anti-reflective coating on the other. The fiber optic screen is made up of the same glass material drawn into 6- μm fibers.

The screens, sheets, and plates were positioned inside the light-tight enclosure of the a-Si imager in direct contact with the imager elements, held in contact by compressive force with a sponge rubber mat. A mosaic array of these materials was configured to obtain relative efficiencies for converting x-ray exposure to image signal. A photograph of the setup is shown in **Fig. 13**. Metal foils were also placed directly against the a-Si diode array to determine sensitivity to electron emission directly from the foils when irradiated by a 9-MV Bremsstrahlung spectrum.

A digital image of the test matrix and horizontal lineouts is shown in **Fig. 14**. Because of wrap-around problems and calibration constraints, no quantitative assessment can be made of relative speeds of the screens.

The conversion mosaic array was tested first at 9 MV with the intention of taking the most promising results and applying them at the lower energies, such as 120 to 450 kV. Results of the conversion efficiency measurements at 9 MV are given in **Table 2**.

We do not observe the Flashscan 20 to be sensitive to electrons emitted by the bare metal, but a metal sheet in combination with scintillating screens does have a small enhancement effect over the screen alone, as expected. The scintillator glass plates, mirror coated and uncoated, and glass fiber plate scintillator are all more effective in producing image signal than the particulate (Min-R) screen but the resolution is not as good as the particulate

screen. From the plain glass results we can conclude that there is no measurable effect from Cerenkov light.

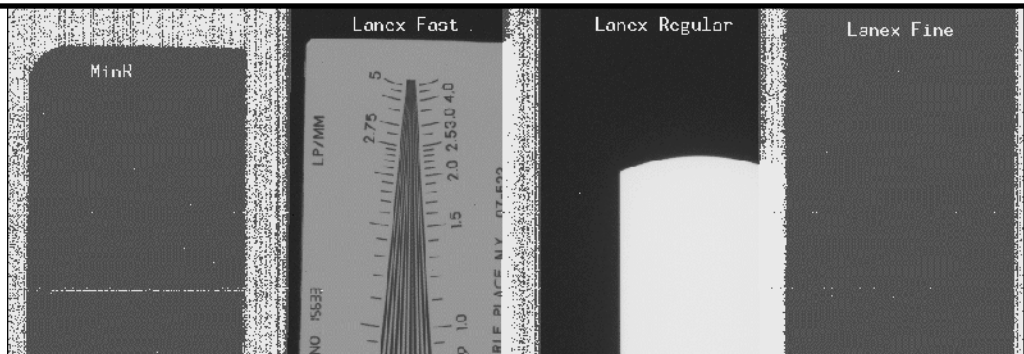
Because the Flashscan 20 proved to be an efficient x-ray imager with the slower but higher resolution GdO₂S₂ particulate screens, a mosaic array of GdO₂S₂ screens only was tested at 120, 250, and 450 kVp, using both filtered and unfiltered x-ray spectra. The screens in this array were Kodak Lanex-Fine, Lanex-Regular, Lanex-Fast, and Min-R. We later discovered, and our studies confirm, that Lanex-Fast and Lanex-Regular are the same material, and that Lanex-Fine and Min-R are the same material with slightly different thickness and backing.

Table 2. Relative efficiency and spatial resolution of different combinations of materials used in the a-Si panel assembly for conversion of x-ray exposure to image signal.

Screen/Material	Supplier	Sheet/Plate thickness (mm)	Relative sensitivity rank order*	Relative resolution rank order*
Min-R screen only	Kodak	N/A	7	1
Min-R Screen + 0.508-in. W sheet	Kodak	0.50	5	2
Min-R screen + 0.508-mm Pb sheet	Kodak	0.50	5	2
Min-R screen + 0.254-mm Pb sheet	Kodak	0.25	4	2
LKH5 glass plate scintillator (2 mm thick)	IQI	2.0	2	Negligible
LKH6 glass fiber scintillator (12 μm dia. fiber, 1.6 mm thick)	IQI	1.6	2	5
LKH5 glass plate scintillator, mirror coated (2 mm thick)	IQI	2.0	1	Negligible
Pb sheet only	N/A	0.50	Negligible	N/A
W sheet only	N/A	0.50	Negligible	N/A
Glass sheet only	N/A	2.0	Negligible	N/A

* Rank order no. 1 indicates best performance.

Figure 15. Image of screen array including Min-R, Lanex-Fast, Lanex-Regular, and Lanex-Fine as obtained with Flashscan 20. Diverging line pair gauge is positioned to image with Lanex-Fine. Tantalum block is positioned to image with Lanex-Regular.



A diverging line-pair gauge, tungsten block and tantalum cylinder were imaged with the array of screens as shown in **Fig. 15** (tantalum cylinder not shown).

A digital image of a line pair gauge taken at 120 kVp is shown in **Fig. 16a**. Lineouts at 2, 3, and 4 lp/mm are shown in **Fig. 16b**. Note that aliasing begins between 3 and 4 lp/mm which is consistent with the pixel pitch and the MTF data presented below.

Images of the tantalum pieces were used to determine the MTF by the edge-spread method. The tungsten pieces provide total absorption, or near total absorption, at all x-ray spectra at operating tube voltages 120 kV to 450 kV. The MTFs for the four screens at 120, 250 and 450 kVp, respectively, are shown in **Figs. 17, 18, and 19**. Note that the Lanex-Fine and Min-R curves are very similar as are the Lanex-Regular and Lanex-Fast.

The MTF results for unfiltered and filtered spectra are shown in **Figs. 20 and 21**, respectively. The MTF for the unfiltered spectra show essentially no energy dependence, and provide useful modulation, for example, greater than 5%, up to 3.5 lp/mm. This indicates that the limiting factor in resolution for these tests is the pixel size of the a-Si array (4 lp/mm). The MTF for the filtered 250 and 450 kV spectra are nearly the same, while the MTF for the filtered 120 kV spectrum is considerably lower.

An important measure for practical use of the a Si imager is the maximum exposure that can be applied to the imager without saturating the electronic storage capacity of the array. The useful range of the imager in our case corresponded to a pixel value of 3400 with no exposure (for example,

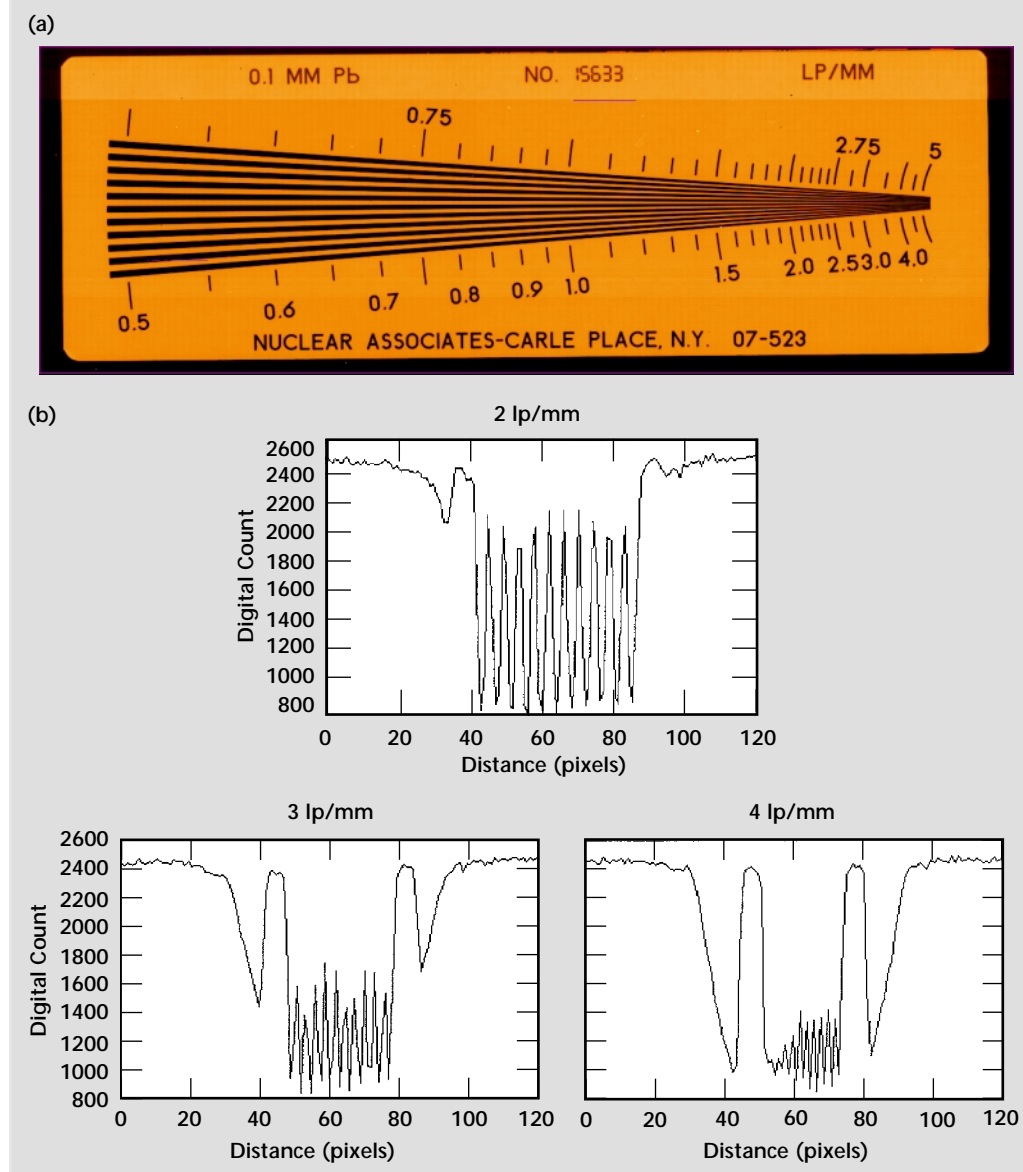


Figure 16. Digital image of (a) line pair gauge and (b) lineouts at 2, 3, and 4 lp/mm.

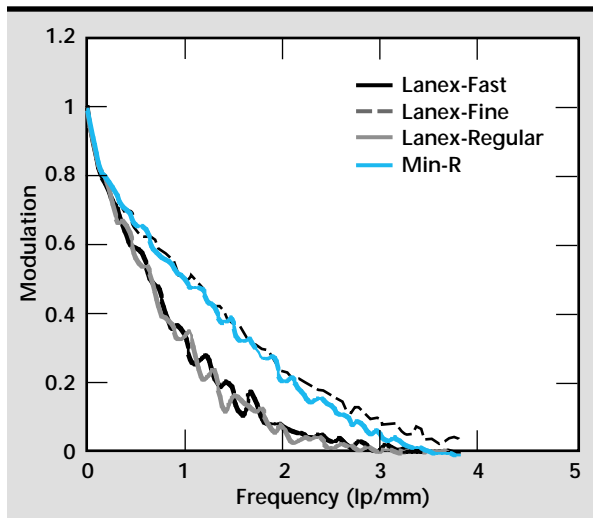


Figure 17. Modulation transfer function of a-Si imager with four different screens at x-ray source energy 120 kVp.

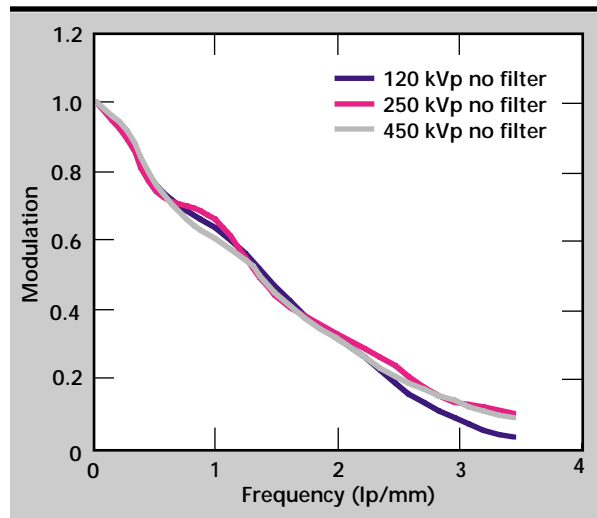


Figure 20. Modulation transfer function of a-Si imager with Min-R screen for unfiltered spectra at 120 kVp, 250 kVp, and 450 kVp.

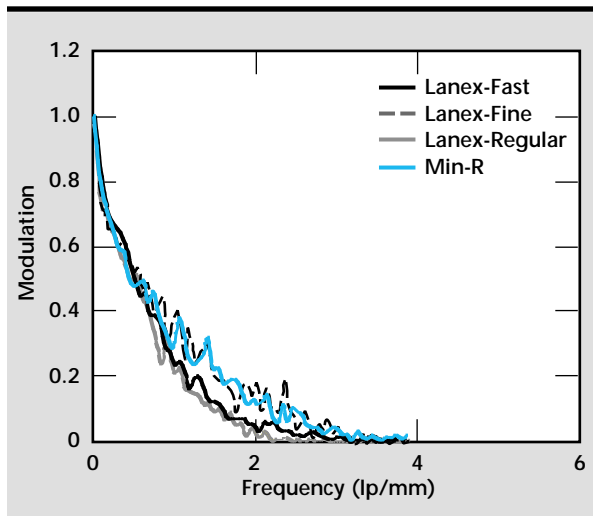


Figure 18. Modulation transfer function of a-Si imager with four different screens at x-ray source energy 250 kVp.

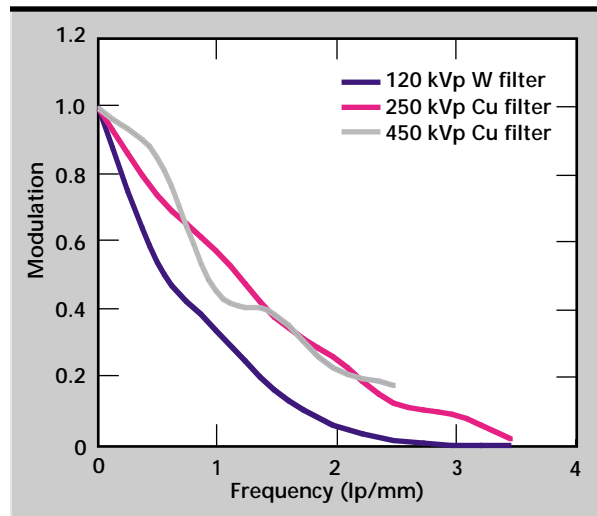


Figure 21. Modulation transfer function of a-Si imager with Min-R screen for filtered spectra at 120 kVp, 250 kVp, and 450 kVp.

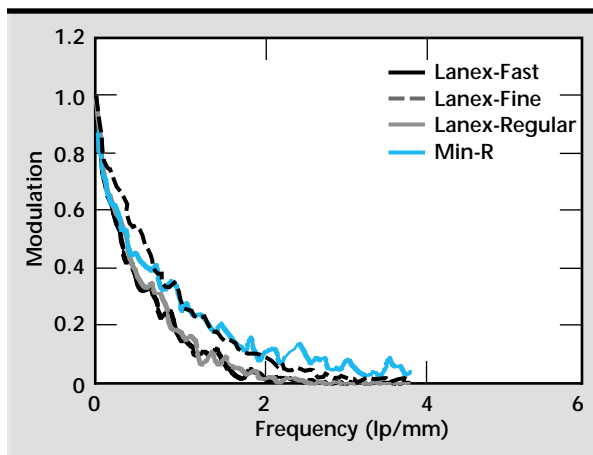


Figure 19. Modulation transfer function of a-Si imager with four different screens at x-ray source energy 450 kVp.

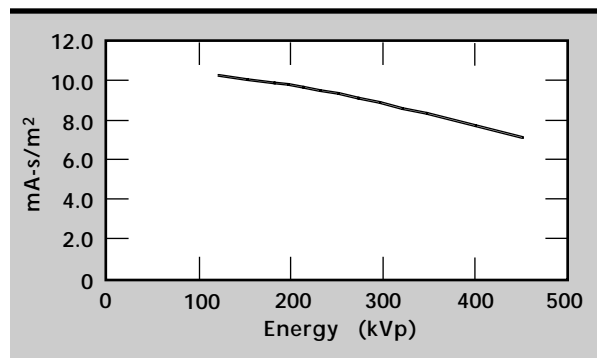


Figure 22. Exposure parameters required to produce light-field image, for example, maximized image without saturation, in terms of x-ray machine settings and source-to-imager distance in units of mA-s/m².

dark-field image as previously described in the calibration section) to a value of 500 with maximum exposure (for example, light-field image previously described in the calibration section). This provides a useful dynamic range of nearly 3000, which is less than the 12-bit (4096) digital capability of the panel, but greater than 11 bits

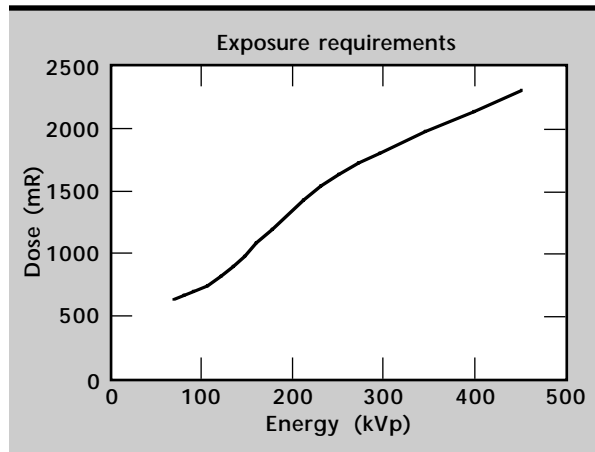


Figure 23. Exposure requirement for unfiltered x-ray spectra to produce light-field image, for example, maximized image without saturation, in terms of accumulated dose (milliroentgen).

(2048). The exposure required to produce the light-field image in terms of x-ray machine settings and source-to-imager distance in units of milliamperes-seconds/square meter (mA-s/m²) is shown in **Fig. 22** for unfiltered source spectra.

The exposure requirements to produce the light-field image in terms of accumulated exposure at the imager is shown in **Fig. 23** for unfiltered source spectra.

Applications

The dpiX a-Si flat panel imager provides a quality large area digital image for a variety of applications. We have used the present 8-in.- \times -10-in. flat panel imager, and additional 12-in.- \times -16-in. imagers for programmatic test objects, automotive components, castings, and structural components.

A 76-mm-diameter steel bridge pin was inspected at 9 MV, using both digital radiography and CT.²⁹ Known defects were detected and measured. A digital radiograph of a bridge pin is shown in **Fig. 24** along with two horizontal slices. Vertical slices are shown in **Fig. 25**. A digital radiograph and a CT slice of a prototype clutch retainer are shown in **Fig. 26**.

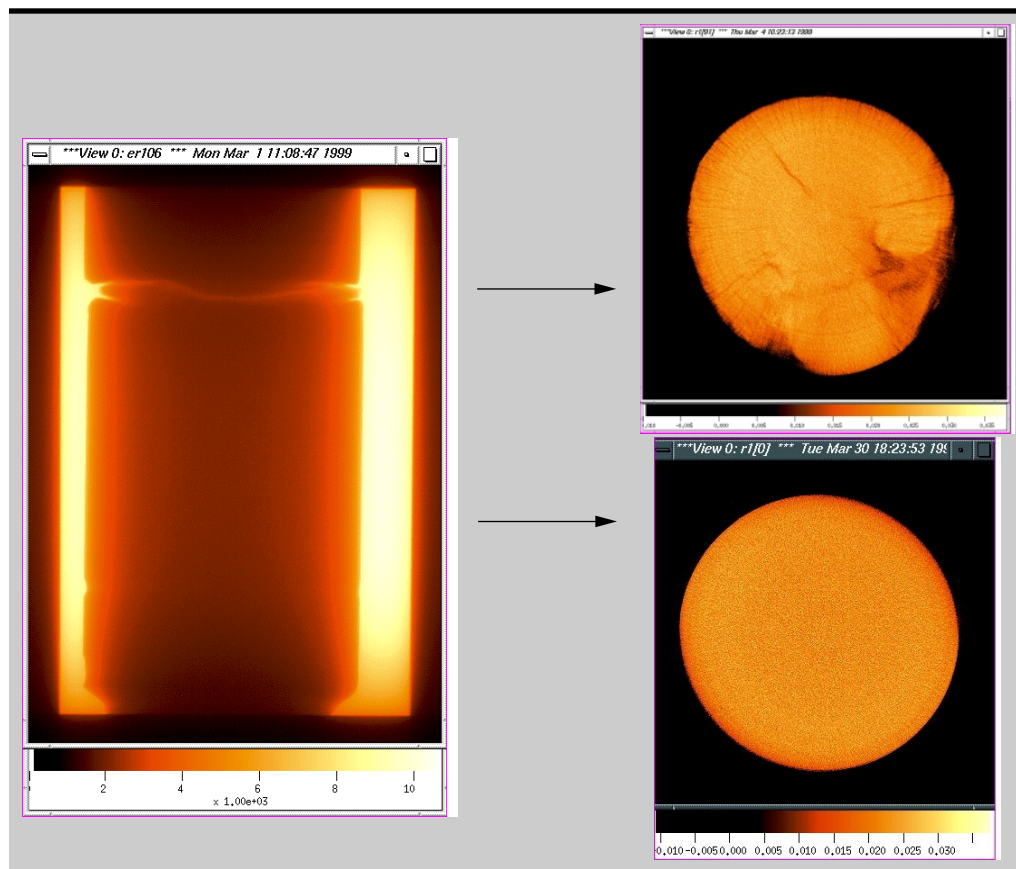


Figure 24. Digital radiograph (left) and CT slices (right) of a bridge pin with a-Si flat panel imager at 9 MV.

Conclusions

The dpi χ a-Si flat panel has been shown to be extremely useful for digital radiography and CT. The image acquisition time, image quality, and field of view (image area) makes possible fast turnaround radiographic evaluation of components, quantitative evaluation of the digital images based on existing image analysis codes, on-line inspection for production applications, and data acquisition for large CT data sets (many angular views). The useful energy range spans all the energies attempted here, 120 kV to 9 MV. The spatial resolution is limited by the pixel size of the imager to approximately 3.5 lp/mm and the dynamic range is approximately 3000. Image areas are available up to 300 mm \times 400 mm, and a mosaic arrangement of 4 panels will give 1200 mm \times 1600 mm image area. Radiation damage is a concern, but we believe recent developments have moved sensitive components sufficiently away from the image area that they can be adequately shielded.

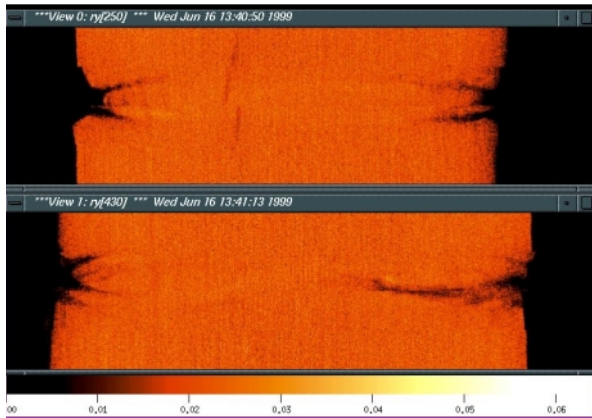
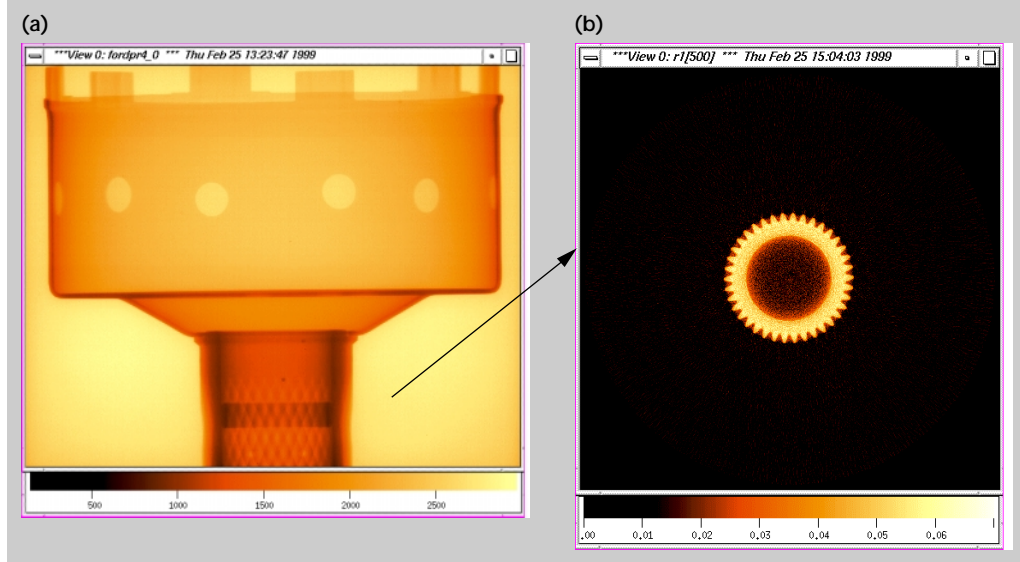


Figure 25. Vertical CT slices from bridge pin data.

Figure 26. Digital radiograph (a) and CT slice (b) of Ford prototype clutch retainer housing (by permission of Ford Motor Company, Dearborn, Michigan) with a-Si flat panel imager at 4 MV.




Acknowledgments

We would like to acknowledge the contributions of E. Updike, K. Morales, and A. Guerrero for data acquisition and test setup configurations, and A. Waters for bridge pin CT reconstructions.

References

1. C. M. Logan *et al*, "MTF results: dpi χ Flashscan 20 imaging array in a 9-MV linac spectrum and comparison to IQI glass/CCD," in press.
2. R. A. Street, S. Nelson, L. Antonuk, and V. Perez-Mendez (1990), "Amorphous silicon sensor arrays for radiation imaging," *Materials Research Society Symposium Proceedings*, Vol. **192**, pp. 441-452.
3. L. E. Antonuk, J. Yorkston, W. Huang, J. Boudry, E. J. Morton, and R. A. Street (1993), "Large-area flat-panel a-Si:H arrays for x-ray imaging," *SPIE Proceedings*, Vol. **1896**, pp. 18-29.
4. R. A. Street and L. E. Antonuk (1993), "Amorphous silicon arrays develop a medical image," *IEEE Circuits and Devices*, pp. 38-42.
5. P. K. Gallagher (1995), "Amorphous silicon arrays promise large-area imagers," *Laser Focus World*, May.
6. W. Que and J. A. Rowlands (1995), "X-ray imaging using amorphous selenium inherent spatial resolution," *Med. Phys.*, Vol. **22**, No. 4, pp. 365-374, April.
7. J. A. Rowlands and D. M. Hunter (1995), "X-ray imaging using amorphous selenium: photoinduced discharge (PID) readout for digital general radiography," *Med. Phys.*, Vol. **22**, No. 12, pp. 1983-1996, December.
8. R. E. Colbeth, M. J. Allen, D. J. Day, D. L. Gilblom, M. E. Klausmeier-Brown, J. Pavkovich, E. J. Seppi,

- and E. G. Shapiro (1997), "Characterization of an amorphous silicon fluoroscopic imager," *Proc. of SPIE Conference on Medical Imaging, Physics of Medical Imaging, SPIE*, Vol. **3032**, February 22–28.
9. D. L. Gilblom (1997), "From amorphous silicon: large-area electronic imagers for x-ray and more," *Advanced Imaging*, pp. 44–48, September.
 10. P. K. Solatani, D. Wynewski, and K. Swartz (1999), "Amorphous selenium direct radiography for industrial imaging," *Proc. of Computerized Tomography for Industrial Applications and Image Processing in Radiology*, Berlin, Germany, March 15–17.
 11. M. J. Yaffe and J. A. Rowland (1997), "X-ray detectors for digital radiography," *Physics in Medicine and Biology*, Vol. **42**, pp. 1–39.
 12. W. Zhao and J. A. Rowlands (1997), "Digital radiology using active matrix readout of amorphous selenium: theoretical analysis of detective quantum efficiency," *Med. Phys.*, Vol. **24**, No. 12, pp. 1819–1833, December.
 13. L. E. Antonuk, Y. El-Mohri, A. Hall, K-W Jee, M. Maolinbay, S. C. Nassif, X. Rong, J. H. Siewerdsen, Q. Zhao, and R. L. Weisfield (1998), "A large-area, 97 μm pitch, indirect-detection, active matrix, flat-panel imager (AMFPI)," *Proc. of SPIE Conference on Medical Imaging, Physics of Medical Imaging, SPIE*, Vol. **3336**, pp. 2–13, February 22–24.
 14. C. Bueno and G. A. Mohr (1998), "Advanced digital x-ray radiographic systems," *Proc. of ASNT Fall Conference and Quality Testing Show*, pp. 121–123, October 19–23.
 15. R. E. Colbeth, M. J. Allen, D. J. Day, D. L. Gilblom, R. A. Harris, I. D. Job, M. E. Klausmeier-Brown, J. M. Pavkovich, E. J. Seppi, E. G. Shapiro, M. D. Wright, and J. M. Yu (1998), "Flat-panel imaging system for fluoroscopy applications," *Proc. of SPIE Conference on Medical Imaging, Physics of Medical Imaging, SPIE*, Vol. **3336**, pp. 376–387, February 22–24.
 16. M. E. Klausmeier-Brown, M. J. Allen, S. J. Boyce, R. E. Colbeth, D. L. Gilblom, I. D. Job, M. Koenig, J. M. Pavkovich, M. Wright, and J. M. Yu (1998), "Real-time image processing in a flat-panel, solid-state, medical fluoroscopic imaging system," *Proc. of SPIE Conference on Real-Time Imaging III, SPIE*, Vol. **3303**, January 26.
 17. C. M. Logan, J. J. Haskins, K. E. Morales, E. O. Updike, J. M. Fugina, A. D. Lavietes, D. J. Schneberk, G. J. Schmid, K. Springer, P. Soltani, and K. Swartz (1998), "Evaluation of an amorphous selenium array for industrial imaging," Lawrence Livermore National Laboratory, Livermore, California (UCRL-ID-132315).
 18. D. Mah, J. A. Rowlands, and J. A. Rawlinson (1998), "Sensitivity of amorphous selenium to x-rays from 40 kVp to 18 MV: measurements and implications for portal imaging," *Med. Phys.*, Vol. **25**, No. 4, pp. 444–456, April.
 19. G. Pang, W. Zhao and J. A. Rowlands (1998), "Digital radiology using active matrix readout of amorphous selenium: geometrical and effective fill factors," *Med. Phys.*, Vol. **25**, No. 9, pp. 1636–1646, September.
 20. E. Samei, M. J. Flynn, and D. A. Reiman (1998), "A method for measuring the presampled MTF of digital radiographic systems using an edge test device," *Med. Phys.*, Vol. **25**, No. 1, pp. 102–112, January.
 21. J. H. Siewerdsen, L. E. Antonuk, Y. El-Mohri, J. Yorkston, and W. Huang (1998), "Signal, noise power spectrum, and detective quantum efficiency of indirect-detection flat-panel imagers for diagnostic radiology," *Med. Phys.*, Vol. **25**, No. 5, pp. 614–628, May.
 22. J. H. Siewerdsen and D. A. Jaffray (1999), "A ghost story: spatio-temporal response characteristics of an indirect-detection flat-panel imager," *Med. Phys.*, Vol. **26**, No. 8, August.
 23. R. E. Colbeth, V. N. Cooper III, D. L. Gilblom, R. Harris, I. D. Job, M. E. Klausmeier-Brown, M. Marc, J. Pavkovich, E. J. Seppi, E. G. Shapiro, M. D. Wright, and J. M. Yu (1999), "Characterization of a third generation, multi-mode sensor panel," *Proc. of SPIE Conference on Medical Imaging, Physics of Medical Imaging*, Vol. **3659**, pp. 491–500, February.
 24. K. M. Gibbs, H. Berger, T. Jones, J. Haskins, D. Schneberk, and J. Brenizer (1999), "Flat panel imaging of thermal neutrons," *Proc. of ASNT Fall Conference and Quality Testing Show*, pp. 140–142, October 11–15.
 25. T. S. Jones (1999), "Evaluation of digital x-ray imaging systems for US Air Force applications," *Proc. of ASNT Fall Conference and Quality Testing Show*, pp. 137–139, October 11–15.
 26. C. M. Logan and A. E. Scach von Wittenau, "Back shield albedo effects on imagery with a dpiX Flashscan 20 using a 9 MV Bremsstrahlung spectrum," Lawrence Livermore National Laboratory, Livermore, California, in press.
 27. R. L. Weisfield, M. A. Hartney, R. A. Street, and R. B. Apte (1998), "New amorphous-silicon image sensor for x-ray diagnostic medical imaging applications," *Proc. of SPIE Conference on Medical Imaging, Physics of Medical Imaging*, Vol. **3366**, pp. 444–452, February 22–24.
 28. D. E. Perkins, R. R. Ryon, J. J. Haskins, and K. W. Dolan (1991), "Calculation of x-ray tube spectra on the Macintosh," *Proc. of ASNT Spring Conference*, March.
 29. A. M. Waters, H. E. Martz, C. M. Logan, E. Updike, and R. E. Green, Jr. (1999), "High energy x-ray radiography and computed tomography of bridge pins," Lawrence Livermore National Laboratory, Livermore, California (UCRL-JC-132822), May. 



High-Frequency Laser-Based Ultrasound for NDC Applications

Robert D. Huber and Graham H. Thomas
*Manufacturing and Materials Engineering Division
Mechanical Engineering*

Howard Lee
Defense and Nuclear Technology

Christopher Richardson and Professor James Spicer
*The Johns Hopkins University
Baltimore, Maryland*

We have demonstrated the feasibility of using a pump-probe system to generate and detect very high-frequency ultrasound. We have investigated materials such as Mo/Si multilayers. Frequencies as high as 892 GHz were detected, and the effects of 100-nm-diameter defects were observed. High-frequency laser-based ultrasound has proven useful for nondestructive characterization applications.

Introduction

Many new high-technology materials and structures have critical dimensions that can be quite small, down to the nanometer level, and therefore the critical size for defects of such materials and structures is also quite small. To ensure the integrity of these materials, nondestructive characterization techniques with extreme resolution are desired. Extremely high-frequency ultrasound is one possibility for characterizing these nanoscale materials, which may include thin films for optical coatings, multilayer materials for fast electronics and mask blanks for the Extreme Ultraviolet Lithography (EUVL) program at Lawrence Livermore National Laboratory (LLNL). However, traditional contact ultrasound above 100 MHz can be quite difficult because of various limitations. Ultrafast laser-based ultrasound offers a way to generate and detect ultrasound of very high frequencies (>100 GHz), and therefore has the resolution required to characterize nanoscale materials.

A major difficulty in using very high-frequency ultrasound, regardless of how it is generated, deals with the increase in attenuation as the frequency of the ultrasound increases. Ultrasound at frequencies above 100 GHz will propagate only extremely short distances. The use of transducers becomes increasingly difficult as the frequency is increased since the

energy must be coupled from the transducer into the material. Impedance mismatches between transducers and materials become critical, and couplant layers of any thickness can attenuate the wave to a useless level before it enters the material to be investigated.

By using a pulsed laser to generate the ultrasound, the ultrasound is generated directly in the material, avoiding the problems associated with coupling the ultrasound into the material. And, by using a laser-based system to detect the ultrasound, there is no loading of the surface by transducers, which can greatly affect the ultrasound. There is also no need to couple the ultrasound into a detector, thus avoiding the coupling problems on the detection side as well.

The current state of the art for ultrafast laser-based ultrasound uses a pump-probe technique^{1,2} in which a short duration laser pulse is split to provide both a pump beam to generate the ultrasound, and a probe beam to detect the ultrasound. **Figure 1** shows the basic set-up for a pump-probe system. Unlike traditional ultrasonic testing which can gather amplitude versus time data in a single shot, the pump-probe technique gathers data for single points in time with respect to time zero (pumping of the sample). Information from different points in time are gathered, and then the information is assembled to form an amplitude versus time plot for the ultrasonic displacement of the material. The

pump-probe technique uses a variable optical delay that consists of a retro-reflector mounted on a linear translation stage. For our tests, the optical delay can be used to gather data up to 300 ps after the pumping of the sample.

For this technique, the pump and probe beams are focused to very small spot sizes (micrometers). However, this dimension is quite large compared to the thickness of the samples that are usually investigated using this technique. The depth of absorption is quite shallow compared to the focused size of the laser beam, and so the interaction volume is disk-shaped. The pump and probe beams are co-located on the sample, and many aspects of the testing can be considered to be one-dimensional. For a material consisting of a thin layer on a substrate, if the pump laser pulse is absorbed entirely in the layer, the ultrasound generated in the sample propagates normally into the material and then reflects off the layer-substrate interface. The ultrasound can then be detected when it reaches the free surface of the layer. If the ultrasonic velocity of the material is known, the thickness can be calculated very accurately from the time-of-flight information gathered from the pump-probe run. The pump-probe technique has been used to measure layer thicknesses from as small as 0.5 nm to a few hundreds of nm.¹⁻⁷

Because the pump-probe technique cannot gather data in a single shot, it is impractical to use this technique to scan very large areas. With improvements to lasers and other hardware, the time to gather data from a single point on a material has been reduced, but further reduction is required to make scanning

large areas practical. Also, LLNL programs such as EUVL need to scan large numbers of samples, and therefore rapid scan times are required. We have proposed a novel white light detection scheme whereby an entire amplitude versus time trace can be gathered from a single laser pulse. This technique takes the single frequency probe pulse, and converts it to a white light pulse that is then directed towards the sample. The various spectral components of the white light pulse are delayed and reach the sample at different times over the continuum of frequencies of which the light is composed. The white light pulse is then sent to a spectrometer, which outputs an amplitude versus time trace based on the amplitude and arrivals of the components of the white light pulse. We hope to obtain funding to investigate this novel technique, and believe that this work will be a major contribution in the field of ultrafast laser-based techniques.

Basically, the pump-probe technique measures the change in reflectivity of the sample as a function of time. Energy from the pump pulse is absorbed by the material, and this energy is converted to heat. This localized change in temperature of the material can lead to a localized change in stress which can propagate through the material as an ultrasonic wave. There can also be a thermal pulse which propagates through the material as a function of the thermal properties of the material. Changes in temperature and pressure of materials can lead to changes in reflectivity. Since the pump-probe technique measures only the change in reflectivity, the change due to temperature must be separated from the change due to the passage of an ultrasonic wave. For the detection of ultrasound, the pump-probe technique depends on materials showing a strong piezorefectivity effect. For materials that show weak piezorefectivity, an interferometer must be used as the detection mechanism. This would involve a change to the set-up shown in **Fig. 1**.

We have been working with members of the EUVL project at LLNL to discuss material characterization concerns of that program. EUVL is a promising contender for next generation lithography technologies. Unlike traditional lithography, EUVL operates in the extreme ultraviolet regime, ~10 to 14 nm in wavelength. One critical problem in the program is producing defect-free mask blanks. Currently, the mask blank is composed of 41 layer pairs of Mo/Si deposited on Si wafers, the total thickness of the multilayer being about 280 nm. The program is interested in finding defects in these multilayer structures, both on the substrate, within the multilayer, and on the surface. Currently, commercially available optical scattering inspection tools are used

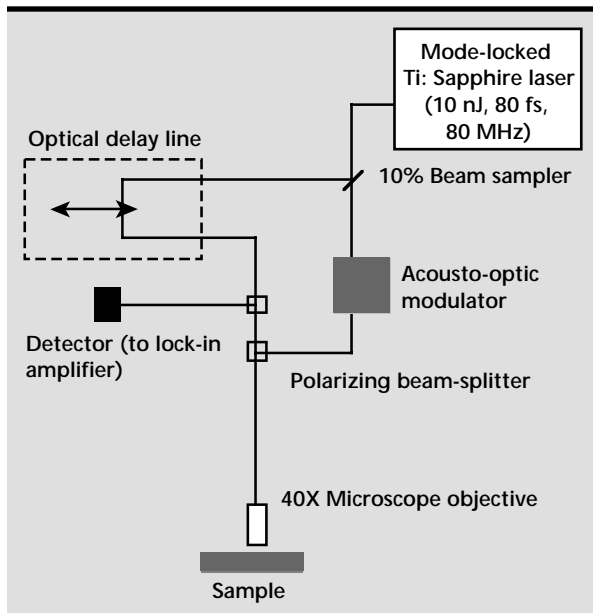


Figure 1. Pump-probe system.

for full mask blank inspection and atomic force microscopy (AFM), scanning electron microscopy (SEM), and EUV scatter are used to look at specific defects. The critical defect size predicted by modeling is around 50 nm. Ultrafast laser-based ultrasound is capable of generating and detecting frequencies high enough to provide the resolution for these dimensions. Ultrafast laser-based ultrasound has the possibility of becoming a process-monitoring technique during the growth of these multilayers if it can meet the characterization requirements for these multilayer materials.

However, there is much work to do to get to that point. Large increases in the rate of data acquisition are required since the current wafers are 6 in. in diameter, and the goal is to move to 8-in. diameter wafers. The probe beam in the pump-probe system is focused to about 1 μm . Scanning a large area the size of a multilayer wafer with such a small footprint is quite a challenge, and the only way that this may become practical is for the data to be acquired in a single-shot mode such as with the white light detection scheme. The white light detection could reduce the data acquisition time for one location from the few minutes that are required for the pump-probe technique to less than one second. The EUVL program has a goal of scanning 1 wafer/min, but presently would accept a rate of 5 to 10 wafers/h.

Progress

The initial goal of this project was to investigate ultrafast laser-based ultrasound to see how it may benefit various LLNL programs. In collaboration with The John Hopkins University, we set up a pump-probe system, and used it to investigate materials of importance to LLNL, such as Mo/Si multilayers.

One goal of the team is to take this technique beyond its current research role. To make this technique more practical for use outside of the laboratory, it is necessary to reduce the time required to gather data. This would allow the technique to move toward the scanning of objects, since images of entire objects are usually desired for the display of information. The idea of using a white light continuum for detection of the ultrasound was developed. Once a white light detection system is set up, data gathered using the more traditional pump-probe technique which uses a single frequency of laser light in the detection pulse would be compared to the data gathered using the white light technique. The equipment to conduct the white light detection has been assembled, and we plan to implement this technology in the Fall of 1999.

During the summer of 1999, the pump-probe system was set up, and data was successfully gathered on several materials of interest to the EUVL program. We exceeded our initial goal and set up a pump-probe system which was state-of-the-art. At the present time, the system is still set up, and could be used to gather data on various materials. We would like to run more tests on EUVL mask blanks, as well as materials of interest to other LLNL programs using also the more traditional pump-probe set up.

Experimental Results

The two main materials used to investigate the pump-probe technique this summer were Si wafers and Mo/Si multilayers. Silicon wafers are used to provide a good substrate for multilayer materials. These wafers are generally too thick for ultrasound generated by the pump-probe technique to propagate through the thickness and then be detected at the surface after reflection from the back side because of the attenuation of these very high-frequency ultrasonic waves. However, these substrates work quite well to help in the initial set-up of the system since one can monitor the change in reflectivity of the sample due to heating by the probe beam.

The Mo/Si multilayered wafers are interesting materials to work with for the laser-based generation of ultrasound. The bilayers of Si and Mo are on the order of 7 nm in thickness, with the Mo being approximately 3 nm and the Si being approximately 4 nm. Almost all of the optical energy is absorbed by the Mo, with very little absorption occurring in the Si. The absorption of the optical energy by the Mo takes place over several layers, not just in the first layer. Because the laser pulse is absorbed primarily in the Mo layers, they begin to increase in temperature directly after the laser pulse strikes the materials, while there is little increase in temperature in the Si layers. This sets up a temperature gradient between the layers and thermal diffusion then takes place to even out the temperature distribution through the layers near the surface. Because of the differential energy absorption, the ultrasound generated is greatly affected by the layer thicknesses in that ultrasound of frequencies with wavelengths corresponding to the Mo/Si bilayer thickness can be generated. Lower frequencies will also be generated. The highest frequencies will be attenuated very rapidly.

Figure 2 shows a long time trace (~ 300 ps) of the change in reflectivity of a Mo/Si multilayer, as gathered using the pump-probe system. The figure plots the change in reflectivity with respect to the

reflectivity of the sample versus time. This figure shows that there is a rapid increase in the reflectivity of the sample directly after heating by the pump beam. This initial change in reflectivity results from the increase in temperature of the material. On this long time scale, there is no ultrasound visible.

However, a higher resolution scan (shorter time scale) was then run. One variable in the data acquisition using this technique is the number of averages taken at each location. Increasing the number of averages increases the signal-to-noise ratio, but increases the time required to obtain the data. The

Figure 2. Pump-probe trace of Mo/Si multi-layer.

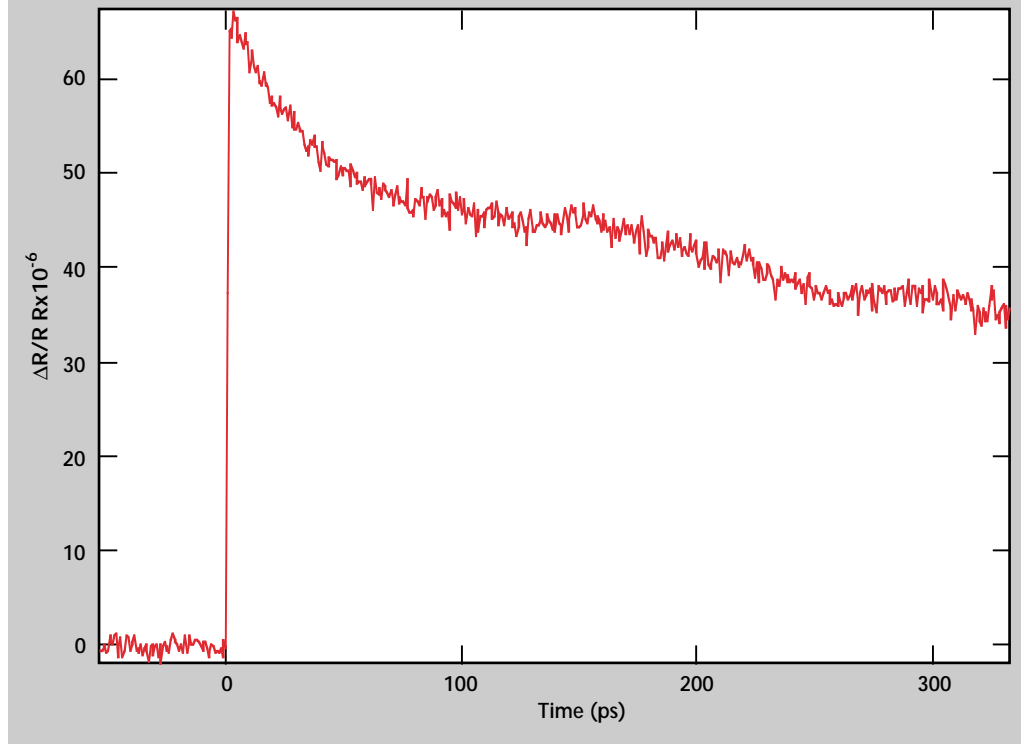
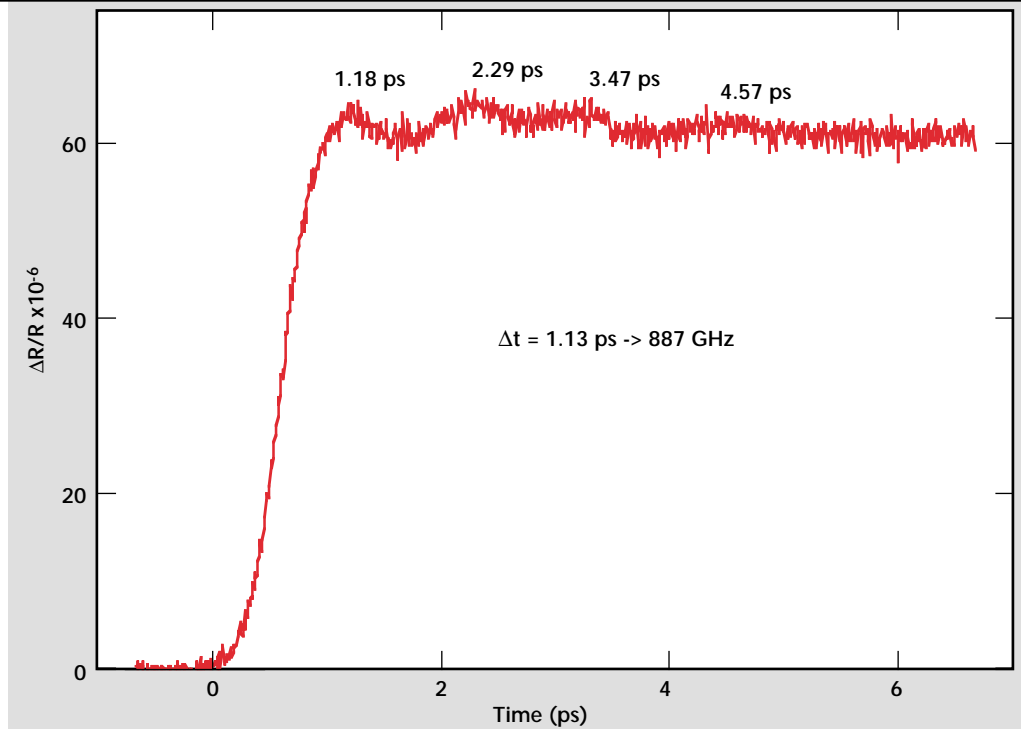


Figure 3. High resolution (short time) trace of Mo/Si multi-layer.



delay increment is also variable, and the size of the increment will affect the resolution.

The results of the higher resolution scan are shown in **Fig. 3**. The ripples seen in the data on this time scale correspond to ultrasound. The arrival times of the ultrasound in picoseconds are shown on the figure. The ultrasound occurs directly after the heating pulse. A fast Fourier transform (FFT) was then run on the data to determine the frequency composition of the ultrasound. The FFT is shown in **Fig. 4**. This figure shows significant energy at frequencies as high as 892 GHz. This frequency is around five orders of magnitude higher than that found in typical ultrasonic characterization of materials. It is believed that these high frequencies result from the differential absorption of the pump beam by the Mo and Si layers, and that varying the thicknesses of these layers would lead to a change in the detected frequencies.

A test was then run on a Mo/Si multilayer wafer that had 100 nm gold spheres embedded at the substrate-multilayer interface to simulate defects. This and the other samples used in this study were all fabricated at LLNL. Currently, all of the EUVL wafers are grown on top of Si substrates. The gold sphere inclusion samples provide wafers with known defects.

Figure 5 shows pump-probe traces from three different spots on the wafer. Two traces are nearly identical, with the third showing a considerably different behavior. The two similar traces are quite

different from the typical response shown by the Mo/Si multilayer while the third trace appears quite similar to the response of the multilayer without the gold sphere inclusions (**Fig. 2**). This could be indicative of the effects of a conductor, in this case the gold spheres, on the thermal behavior of the wafers which thereby affects the change in reflectivity of the material at those locations. The traces believed to show the effects of the gold spheres are labeled “defect spot” in the figure. The trace showing the typical multilayer response is labeled “multilayer.” This shows the potential of using this technique to find defects located at the substrate-multilayer interface.

Conclusions

We successfully constructed a pump-probe system to investigate the feasibility of generating and detecting very high-frequency ultrasound in materials important to LLNL programs. Frequencies as high as 892 GHz were detected. The effects of 100-nm-diameter buried “defects” on received signals were seen. We believe that we will be able to decrease greatly the time required for data acquisition through the implementation of a white light detection technique which we hope to implement soon. High-frequency laser-based ultrasound is clearly a useful technique for NDC applications, and will only increase as technology and new materials are developed.

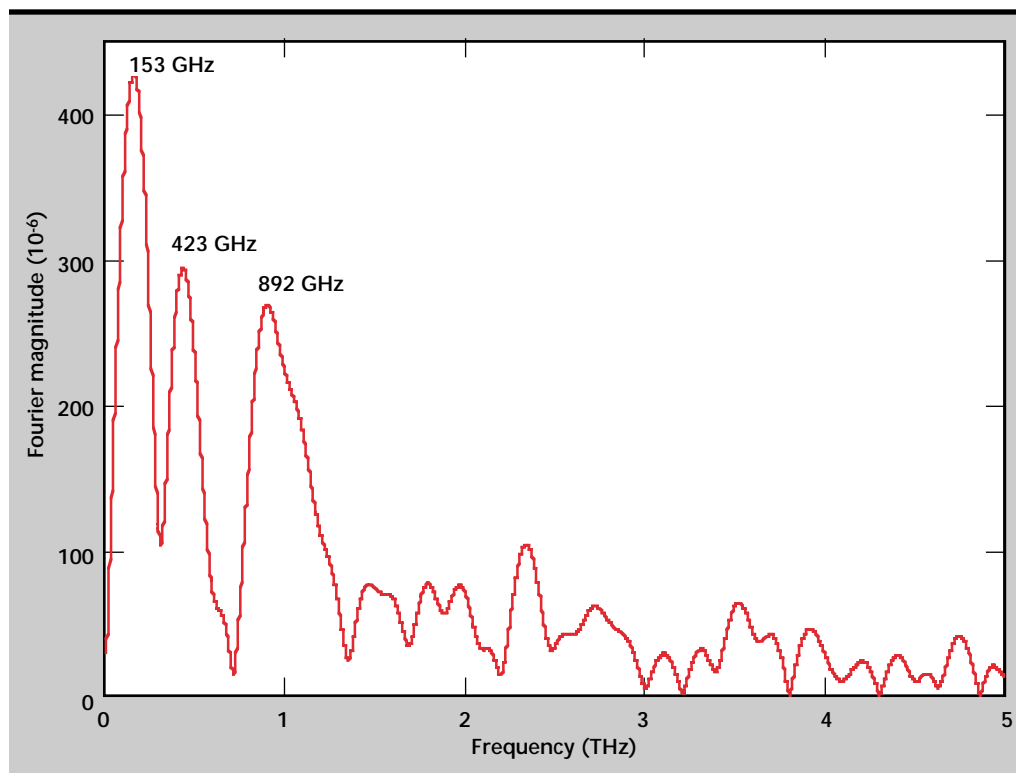
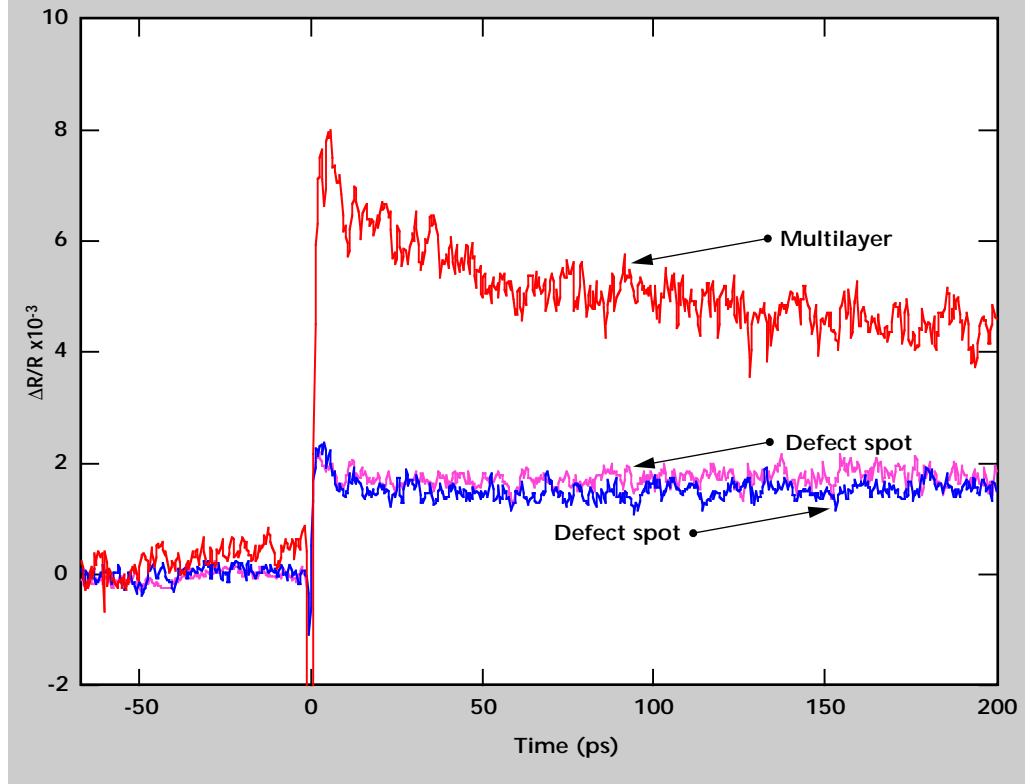


Figure 4. FFT of data shown in Fig. 3.

Figure 5. Data from multilayer material with 100-nm gold sphere inclusions, demonstrating successful detection of simulated defects using the pump-probe technique.



Future Work

Because of the success we achieved on this project, we will seek funding to continue, developing a dedicated ultrafast laser-based ultrasonic characterization system which will allow us to look at various materials of importance to LLNL and to the country.

Future work will focus on the white light detection scheme which holds the promise of greatly increasing the rate of data acquisition, thus making scanning practical. Successful implementation of this detection scheme would be a major contribution to the ultrafast phenomena field.

Acknowledgments

The authors would like to thank members of the EUVL Mask Project of the Information Science and Technology Program at LLNL for providing samples for this work.

References

1. K. Fiedler (1996), "The interferometric detection of ultrafast pulses of laser generated ultrasound," Ph. D. Thesis, The Johns Hopkins University, Baltimore, Maryland.
2. C. Richardson (1998), "Theoretical and experimental ultrafast laser ultrasonic inspection of extended interfaces," Master's Essay, The Johns Hopkins University, Baltimore, Maryland.
3. H. T. Grahn, H. J. Maris, J. Tauc, and K. S. Hatton (1988), *Appl. Phys. Lett.*, Vol. **53**, p. 2281.
4. H. T. Grahn, D. A. Young, H. J. Maris, J. Tauc, J. M. Hong, and T. P. Smith, III (1988), *Appl. Phys. Lett.*, Vol. **53**, p. 2023.
5. H. N. Lin, R. J. Stoner, H. J. Maris, and J. Tauc (1991), *J. Appl. Phys.*, Vol. **69**, p. 3816.
6. C. A. Paddock and G. L. Easley (1986), *J. Appl. Phys.*, Vol. **60**, p. 285.
7. G. Tas, R. J. Stoner, H. J. Maris, G. W. Rubloff, G. S. Oehrlein, and J. M. Halbout (1992), *Appl. Phys. Lett.*, Vol. **61**, p. 1787.

ew Developments in RECON

Jessie A. Jackson
Laser Engineering Division
Electronics Engineering

Over ten years ago Lawrence Livermore National Laboratory (LLNL) began research and development in computed tomography (CT). One product of this work is a package of reconstruction and simulation codes called RECON. RECON has been successfully used for nondestructive characterization, but is in need of revision to keep up with advances in CT and user-friendly interfaces. Some reconstruction codes need to be modified and new ones need to be added. However certain code-wide upgrades must be completed before this can happen. The user interface has been redesigned and a new cone-beam reconstruction code has been implemented with this new user interface.

Introduction

Computed Tomography (CT) is a nondestructive imaging technique for determining a 3-D characterization of an object from a series of 2-D radiographs. For over ten years the Nondestructive Evaluation (NDE) Section at LLNL has used CT for the inspection of industrial materials, objects and assemblies.^{1,2} During this time NDE personnel built an extensive CT system, including a suite of CT reconstruction and simulation codes called RECON.

RECON is available as copyrighted software from the Technology Transfer Office at LLNL.³ The RECON codes have been used extensively for processing and reconstructing radiographic projection data.⁴ However, the code has suffered from a lack of maintenance, documentation and reliability. Also, since the time when RECON was designed computer systems have changed, some of the original design criteria are no longer applicable, and there are many new display and imaging tools available. An effort has begun to upgrade, modernize, and further document RECON.

NDE CT System

There are three major functional parts to the current NDE CT system: the acquisition or simulation of 2-D radiographic data, the reconstruction of a 3-D object from the 2-D data, and the ability to display and examine both 2-D and 3-D data.

The system accomplishes these functions using both hardware and software. The hardware in the

system consists of scanners and computers. The scanners include radiographic sources, stages, and digital detectors used for the manipulation of the object and the acquisition of 2-D radiographs. The computers are used for acquiring, processing, analyzing and displaying data. The software includes codes to control the scanners for acquisition of data and the creation of information and data files, the RECON codes for simulating radiographs and reconstructing images, and a software package called VIEW⁵ for displaying and analyzing digitized images. From the beginning a set of operating conventions, nomenclature, and software standards was adapted which all scanners, simulators and reconstruction codes follow.⁶

The CT scanners each produce their own format of raw data files, which are initially processed by dedicated programs to eventually produce a standard CT parameter file and data files. **Figure 1** shows the interconnection between the scanners, RECON, VIEW and the data files.

The CT parameter file is saved in an ASCII file, referred to as an SCT file. This file contains all necessary information from a scan regarding the configuration of the acquisition system, such as geometric information, dimensions, energies, number of rotations, position of the object, and size of pixels. A new SCT file is created at each processing step with information about the processing just performed as well as all the past processing. This allows a record of processing to be maintained for each data file. An SCT file is also created by RECON when the simulation codes are used to create radiographic data.

The data files are stored in VIEW format using two files for each set of data. The data itself is saved in a binary file called an SDT file. Each data file is accompanied by an ASCII file called an SPR file, containing the dimensional information of the binary file, the type of data, real or integer, how many dimensions, the size of each dimension, the pixel size and the origin of the data. As seen in **Fig. 1**, VIEW can also be used to create object data files to be used as input to the RECON simulation codes. In this case the user must manually create an SCT file. It is important to note that even though RECON is being upgraded the output data produced by the scanners is not changing, so the input to RECON will continue to be in the SCT/SPR/SDT format.

Status of RECON

RECON consists of a number of interconnected codes. There are a variety of reconstruction codes for such applications as filtered back-projection (FBP), convolution back-projection (CBP), constrained-conjugate-gradient parallel and fan beam, and active and passive CT (A&PCT). The simulation codes create simulated radiographs from object descriptions or pixelized images. The bulk of this code is written in the C programming language, while some algorithms are written in FORTRAN. RECON was built to operate on UNIX workstations

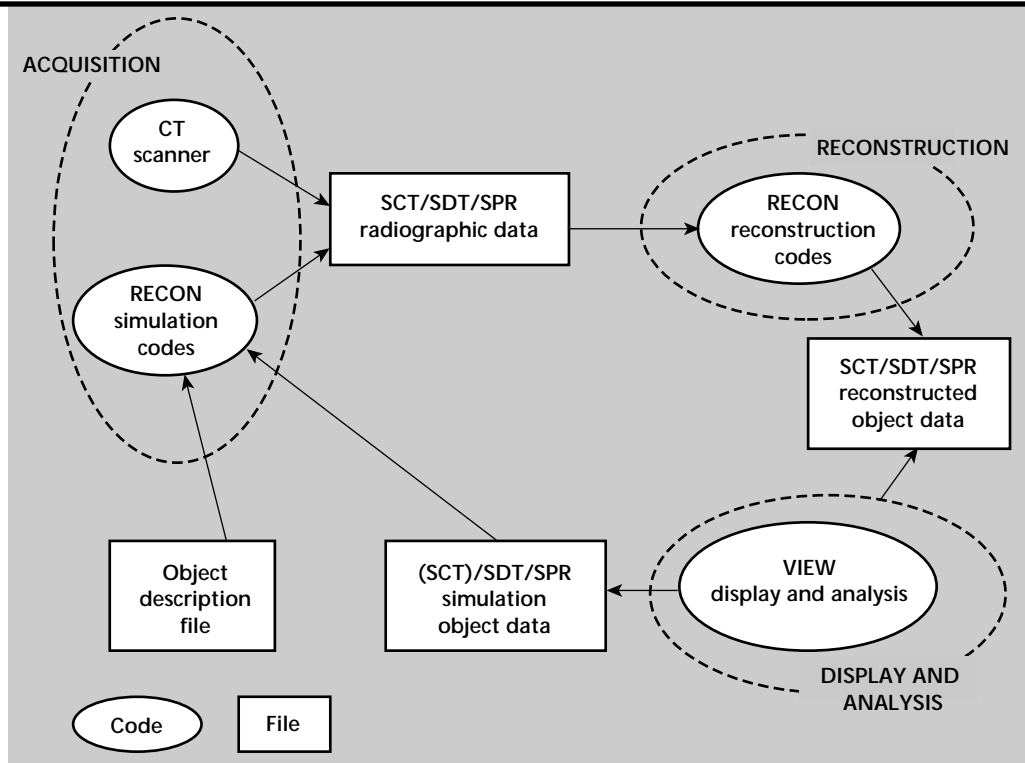
and VAX computers. The code currently has UNIX system calls in it, so RECON must be run on UNIX platforms. The RECON codes were designed for compatibility with the VIEW signal and image processing software, though VIEW software is not required to use the RECON codes.

Currently each application is compiled into separate executable programs. There is a manager program that allows the user to select and start an application. This process is UNIX-dependent. Each application can also be started independently of the manager program. In either case, at start-up RECON reads in a user-specified SCT file. A user interface is provided to allow the user to modify CT parameter values interactively before starting the application process. The user interface is time-consuming and some new options do not work consistently or correctly. RECON currently reads and writes data in VIEW format. Each application has to read and write the CT parameters and data. At present there are a number of input/output (I/O) codes and although the codes are used in all the applications they are scattered throughout each application.

The current structure of the RECON code is complex and highly interconnected, and since there is little documentation it is difficult to learn.

The above problems have made RECON less useful than is acceptable.

Figure 1: CT System showing interconnects among components.



Progress

In addition to fixing problems and adding new reconstruction techniques there are a number of improvements that need be included to make RECON state-of-the-art. These improvements involve the portability and modularity of the code.

To assure compatibility with a wide variety of users, RECON must be portable to computers other than UNIX platforms, such as Macs and PCs. This can be accomplished by building a version of RECON that can be used on any platform that runs C-language executables. There are also a number of software packages available that provide elegant user interfaces and data I/O. However, since often these packages have to be purchased it can not be assumed that every machine that would use RECON would have them available. To satisfy as many users as possible it would be desirable to be able to create versions of RECON to run on machines with different capabilities.

The first step in upgrading RECON is to develop a plan that will accommodate the desired functionality.

RECON Redesign

The structure for the upgraded RECON is shown in **Fig. 2**. The interfaces among the functions are clear and concise. As in the original design each CT application would be compiled into its own

executable. The user interface and the CT parameter and data I/O codes would then be common to all the applications. There are two obvious advantages to this design.

One advantage is that any module for data or parameter I/O can be exchanged for one with different capabilities without affecting the application processing. For example, for a user with a UNIX machine with no special display software, a line-input user interface could be replaced with an X-Window interface. For a Mac without X-Windows, a system could be built with a line-input user interface.

Another example involves the package of codes called Interactive Data Language (IDL). IDL could be used to create a window interface for the CT parameters, and windows for displaying the data, as well as providing data I/O for data of many types of formats. A limitation of IDL is that it is a commercial product that not all RECON users may have. An IDL program will run without modifications on UNIX machines, Macs and PCs. A RECON code constructed as shown in **Fig. 2**, would easily allow the building of a version of RECON with the CT parameter, user interface, and data I/O sections of the code replaced with an IDL interface, as shown in **Fig. 3**.

Another advantage to this design is that the upgrade work can take place in two stages. The first stage would be the implementation of the user interface and

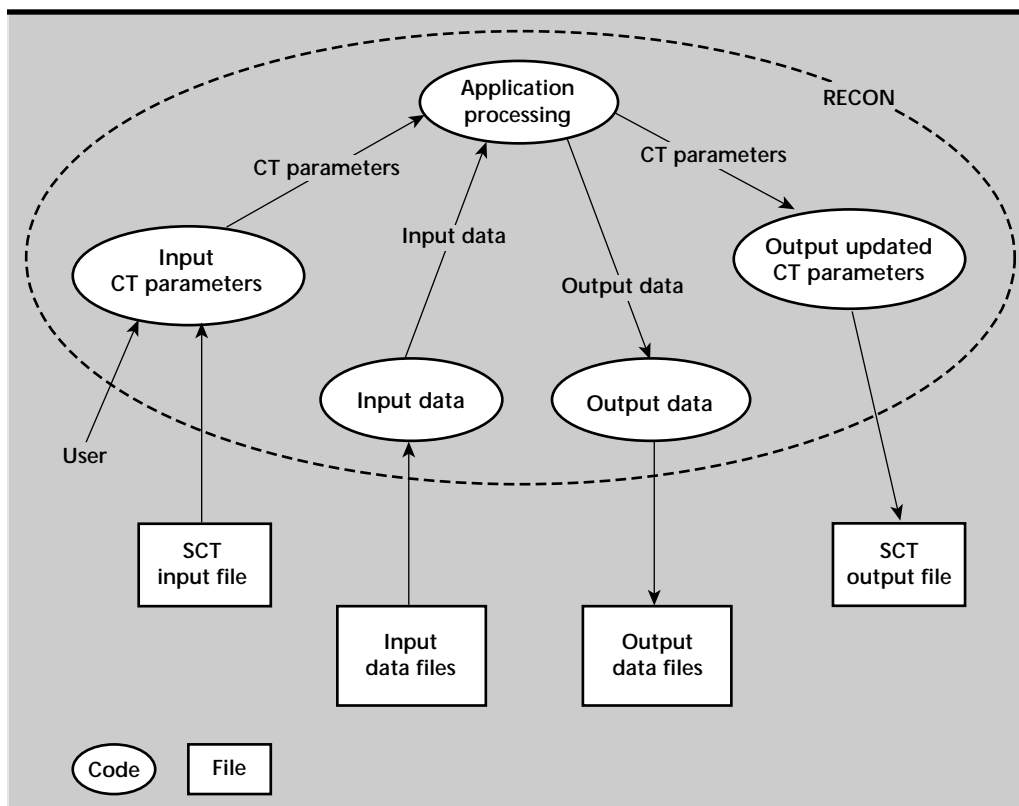
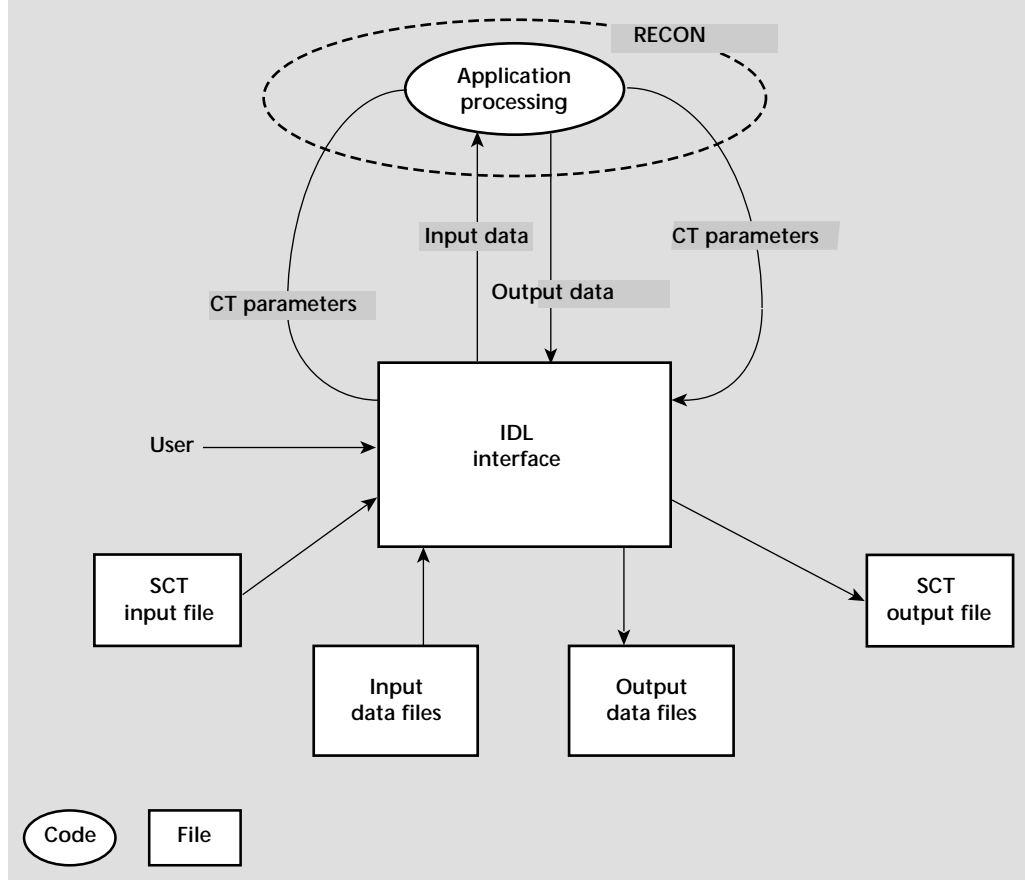


Figure 2: Upgraded RECON Data Flow Diagram.

Figure 3:
IDL/Upgraded
RECON Data Flow
Diagram.



CT parameter and data I/O. Then each application can be modified. This will allow the users access to completed applications before the entire process is complete.

RECON Development Plan

In planning the development of the RECON upgrade the following assumptions and design goals have been established.

Assumptions: (1) RECON will continue to use SCT file formats to input CT parameter information; (2) data I/O will still need to be available in VIEW formats and others to be determined; (3) no major changes will be made to the existing algorithms.

Design goals: (1) clean up and simplify the codes by making the codes more object-oriented and making the data and CT parameter I/O modular; (2) make the code C-language only so that it can be easily ported to Macs and PCs by removing all UNIX system calls and minimizing the use of FORTRAN; (3) improve the user interface, both the reliability and ease of use; (4) document the software; (5) document the CT algorithms; (6) restructure the codes to make future maintenance easier; (7) develop a modular method of building versions

for different hardware platforms; (8) develop an IDL interface for RECON; (9) possibly develop an X-window interface for the UNIX machines, and (10) write modules for data I/O in formats other than VIEW.

RECON Implementation Status

A new line-input C-language-only user interface is complete. Many of the data I/O routines for VIEW data files have upgraded. A new constrained-conjugate-gradient cone beam (JCONE-CCG) algorithm has been implemented with the new user interface and data I/O.

Future Work


The next phase of this project will be to finish the work of modularizing the interfaces to the applications. Then the data I/O routines for VIEW data files will be completed. The JCONE-CCG code will be ported to a Mac and a PC to test the compatibility of RECON on a non-UNIX platform. An IDL interface for JCONE-CCG will also be developed to test the usefulness of IDL as an interface for RECON. The user interface and data I/O will be documented.

Then the process of converting each application will begin. The user interface for each code will be designed. The new application module will be created and the algorithm and the code will be documented. This process will continue application by application.

Acknowledgments

The author would like to thank R. Roberts, J. Haskins, H. Martz and P. Roberson for their knowledge, support and encouragement in this effort. The author also appreciates the support given by LLNL's NDE Section, Materials and Manufacturing Engineering Division, Mechanical Engineering Department and the Center for NDC.

References

1. S. G. Azevedo, H. E. Martz, J. M. Brase, and K. E. Waltjen (1988), "Computed tomography," *Engineering Research, Development, and Technology*, Lawrence Livermore National Laboratory, Livermore, California (UCRL-53868-88), June.
2. J. M. Brase, K. E. Waltjen, and H. E. Martz (1988), "Research in computed tomography," *Engineering Research, Development, and Technology*, Lawrence Livermore National Laboratory, Livermore, California (UCRL-53868-87).
3. S. G. Azevedo (1991), "Model-based computed tomography for nondestructive evaluation," Ph.D. thesis, University of California at Davis, (also Lawrence Livermore National Laboratory (UCRL-LR-106884), March 1991).
4. S. G. Azevedo, H. E. Martz, and G. P. Roberson (1990), "Computerized tomography reconstruction technologies," November/December, *Energy and Technology Review*, Lawrence Livermore National Laboratory, Livermore, California (UCRL-52000-90-11-12).
5. "The VIEW signal and image processing system," J. M. Brase, V. J. Miller, and M. G. Weiting (1988), Lawrence Livermore National Laboratory, Livermore, California (UCID-21368), March.
6. S. G. Azevedo, H. E. Martz, M. F. Skeate, D. J. Schneberk, and G. P. Roberson (1990), "Computed tomography software and standards," Lawrence Livermore National Laboratory, Livermore, California (UCRL-ID-105132), February. 

Component Gap Detection by Infrared Imaging

Charles S. Landram and Richard W. Martin
*New Technologies Engineering Division
 Mechanical Engineering*

Nancy K. Delgrande and Philip F. Durbin
*Manufacturing and Materials Engineering Division
 Mechanical Engineering*

The depth of gaps located below a lamp-heated surface can be determined from infrared (IR) surface temperature images following a single pulse of heat. The gaps are assumed to reside at a fixed depth in a plane parallel to the surface. The magnitude of the image spatial contrast (in temperature) and the time at which it is the sharpest (brightest) provide two unique quantities whose measurements can be used to determine gap depth. This determination requires (direct) numerical solution to the unsteady, multidimensional heat conduction equation based on a tentative buried gap shape similar to that observed at the surface. The procedure is illustrated for a cylindrical gap buried 3/8 in. from the surface of a 3-in. slab of stainless steel. Also considered are detection of gaps interfacing cylindrical shells and cracks perpendicular to the surfaces of thin shells.

Introduction

Methods for detecting subsurface cavities from outer surface IR images have been developed for internally heated (or cooled) cavities or the volumetrically heated containing solid.¹⁻⁴ For the heated cavity, its fluid temperature and heat transfer coefficient must be specified as a means of providing a known steady-state heating rate. Experimental implementation is difficult owing to the need to provide intrusive cavity heating and instrumentation for determining imposed heat cavity, heat flux, or power density within the solid.

When the cavities are defects, such as delamination gaps between composite material layers that should otherwise be well bonded, the gaps are thin and lie at a subsurface depth in a plane parallel to the outer surface. These kinds of defects have been experimentally revealed by flash heating the outer surface followed by observation of resulting delayed IR images.⁵ In this nonintrusive transient method, the surface images are observed long after the impulsive heating occurs to avoid irradiance of the camera from sources other than sample emission.

The purpose of this work is to determine the gap depths that can be resolved, quantifying these in terms of their size parallel to the surface, the thermal

properties of the solid, the energy flux imposed, and the heat losses from the heated surface. This determination requires numerical solution to the unsteady heat conduction equation applied to the solid, and validation with experimental data.

Progress

Figure 1 illustrates the presence of a thin, subsurface defect at depth L , and residing in a plane parallel to the surface. The defect has a contour of

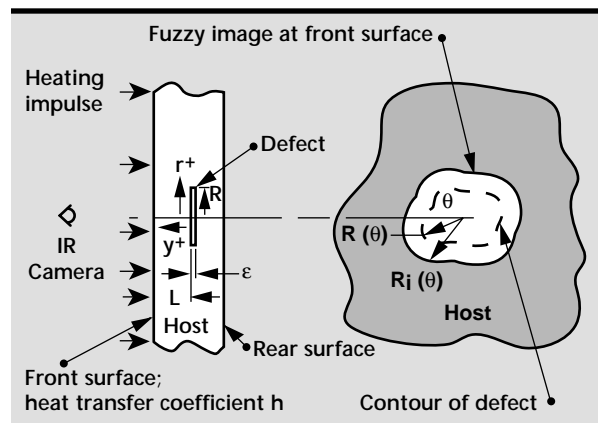


Figure 1. Model and coordinate system for subsurface defect.

$R(\theta)$ as shown. The defect is considered an adiabatic void since the contained gas (air) has less than three orders of magnitude smaller thermal conductivity than that of the solid (host). When the surface is impulsively heated, a thermal diffusion front is propagated axially from the surface towards the defect in the $-y^+$ direction. As the front approaches the defect, the conductive heat flux changes direction and transfers radially along the face of the defect, $y^+ = 0$, in the r^+ direction. Near the outer edge of the defect, $r^+ = R$, the radial heat flux merges with the axial heat flux in $r^+ > R$, and the combined flux flows around the backside of the defect and toward the inner regions of the solid.

This transport distributes a temperature along the front face of the defect. The temperature is greatest at $y^+ = r^+ = 0$ and decreases along $y^+ = 0$ monotonically with increasing r^+ in $0 < r^+ < R$. This local rise in temperature near the defect is propagated back to the front surface at $y^+ = L$ as an attenuated and broadened surface temperature spatial perturbation, which is represented by the observed image.

In addition to the spatial transport, temporal events are also important. The impulsive surface heating causes elevated solid temperatures in early times during which the remainder of the solid including the defect remain near the initial (ambient) temperature. In very late times the entire system equilibrates to the ambient temperature. It will be shown that the images can only be captured in intermediate times and that particular times occur when the images are brightest.

Formulation

The unsteady, multi-directional heat conduction equation applied to the solid regions of **Fig. 1** and written in dimensionless coordinates is given by

$$\frac{\partial v}{\partial t} = \frac{\partial^2 v}{\partial y^2} + \frac{1}{r} \frac{\partial}{\partial r} \left(r \frac{\partial v}{\partial r} \right) + \frac{1}{r^2} \frac{\partial^2 v}{\partial \theta^2} \quad (1)$$

where the dimensionless temperature field is $v = v(y, r(\theta), t)$. The internal boundary conditions on the faces of the defect require the normal temperature gradients to vanish there. Initially, $v(y, r(\theta), 0) = 0$. The external boundary conditions are given as follows:

$$\frac{\partial v}{\partial y} + Bi v = \begin{cases} -1/t_0, & 0 < t < t_0 \\ 0, & t > t_0 \end{cases} \text{ on } y = 1 \quad (2)$$

where Bi is the front surface Biot number, and t_0 is the dimensionless time over which the impulse

occurs. The back side of the solid was taken as semi-infinite; that is, $v \rightarrow 0$ as $-y \rightarrow \infty$. This condition was appropriate for the plate thickness considered and tested. At radial positions far from the defect, that is, for $r \gg R/L$, the following exact solution holds if $t \gg t_0$:

$$v = \frac{1}{\sqrt{\pi t}} \exp \left[-(1-y)^2 / (4t) \right]. \quad (3)$$

Had two different materials comprised the slab of **Fig. 1**, well-bonded along $y = 0$, but possessing the same defect, it would be necessary to apply appropriately scaled versions of **Eq. 1** to both materials and couple their solutions at the contacting surface by continuity of temperature and normal heat flux.

Implementation

In general, $R(\theta)$ and L are sought from surface images observed at $y = 1$. As illustrated in **Fig. 1**, the surface image contour $R_i(\theta)$ is slightly enlarged relative to the actual defect contour $R(\theta)$, but the two will have similar shapes. Their mean circumferential values are respectively denoted \bar{R}_i and \bar{R} . From the observed image, the function $g(\theta)$ is defined by

$$g(\theta) = \frac{R_i(\theta)}{\bar{R}_i} \quad (4)$$

subject to the image area constraint

$$\frac{1}{2\pi} \int_0^{2\pi} g^2(\theta) d\theta = 1. \quad (5)$$

Therefore by similarity,

$$R(\theta) = g(\theta) \bar{R}. \quad (6)$$

Henceforth $g(\theta)$ is considered known from **Eqs. 4** and **5**, but \bar{R} is taken as unknown. For time scales much greater than that for impulsive heating, solutions to **Eqs. 1** and **3** depend on just two parameters, \bar{R}/L and Bi , the former having been introduced by enforcement of the adiabatic condition on the faces of the thin defect and the latter by **Eq. 2**. Since Bi depends on the unknown depth L , it is tentatively set to zero; then once L is found with this restriction, Bi is updated, and the process (to be presented) is repeated until convergence is obtained by the method of successive approximations. Therefore, for fixed values of Bi , and chosen values of \bar{R}/L , direct solution to **Eqs. 1** and **3** can be obtained numerically for the dimensionless temperature field in the solid, $v(y, r(\theta), t)$.

The important result from the solution is the surface image contrast factor defined as $u(t)$:

$$u(t) = v_{s1}(t) - v_{s2}(t) \quad (7)$$

where

$$v_{s1}(t) = v(1, 0, t)$$

and

$$v_{s2}(t) = v(1, \infty, t).$$

On physical grounds, as discussed previously, it is evident for impulsive heating that $u(0) = u(\infty) = 0$ and that at intermediate times u achieves a maximum, $u_{\max} = u(t_{\max})$ at which time

$$du/dt = 0 \text{ when } t = t_{\max} \quad (8)$$

The surface contrast factor is obtained for an array of \bar{R}/L values. Curve fits f_1 and f_2 are respectively determined for u_{\max} and t_{\max} in terms of polynomial curve fits in \bar{R}/L for fixed Bi. Returning to the dimensional definitions for temperature T and time τ , these curve fits can be written as:

$$u_{\max} \equiv \frac{(T1 - T2)_{\max}}{q_s \tau_0 / \rho c L} = f_1(\bar{R}/L) \quad (9)$$

and

$$t_{\max} \equiv \tau_{\max} \alpha / L^2 = f_2(\bar{R}/L). \quad (10)$$

The surface energy flux $q_s \tau_0$ is obtained by separate calibration to be discussed, and $(T1 - T2)_{\max}$ and τ_{\max} are the measured contrast temperature at the time it is the brightest. Since f_1 and f_2 are known, simultaneous solution of **Eqs. 9** and **10** provide unique values for the two unknowns \bar{R} and L at the tentatively selected value of Bi = 0. With this value of L , the Biot number can be evaluated and the process repeated until convergence is achieved. In the following application, the converged value of Bi = 0.014 was rapid and required only a single iteration.

Application to Plates

The method is demonstrated for the case of a defect in the shape of a disk so that all dependence on the circumferential direction θ is removed in **Eq. 1**, and the function g in **Eqs. 4** and **5** is identically unity.

Computational Methods. The finite element code TOPAZ2D⁶ was used to numerically resolve

the axisymmetric, 2-D temperature field, $v(y, r, t)$, centered at the origin of the disk. Two different meshes were used. The first was for an infinitesimally thin disk ($\varepsilon = 0$) having finite R and L in the solid, whose outer solid regions for the radial, r , and axial directions, $-y$, could be considered infinite. The second mesh more faithfully modelled the actual experimental case which was a 0.32-cm-thick gap, having an outer radius boundary of 5 R in a slab of thickness 7.62 cm with adiabatic boundary conditions at radial and axial extremities. Results obtained from these two different meshes did not differ significantly, so neither defect thickness nor outer boundary placement were deemed to be very important within the range of values considered. In the case tested, upon which discussion is deferred, the solid was 304 stainless steel, with a disk gap of radius 2.54 cm at a depth of 0.9525 cm.

In the case of the mesh whose radial and axial dimensions were semi-infinite, the mesh was spatially truncated in r where the numerical solution agreed to within 1% of the exact solution there (**Eq. 3**) and in $-y$ to within the same accuracy with $v = 0$ there. Mesh size was also varied, especially near the defect, to find the required size for adequately resolving the temperature distribution. The steepest temperature gradients were found near $y = 0$, on the front side of the defect, along about $0.7 < r^+ / R < 1$ where the mesh was made relatively small. As many as 101 total front-face defect nodes were used, and as many as 7011 total nodes were used within the entire solid.

A fixed dimensionless time step of between 0.5 and 1 was used, and numerical output was found to be insensitive to the value. In the experimental case, these time steps correspond to between about 0.05 to 0.1 s. Some care was required to accurately capture the effects of the impulsive heating (see **Eq. 2**). To avoid having a very small time step initially, the problem was started at $t = 0.05$. Prior to this time **Eq. 3** gives the starting solution since in this early time the diffusion front is far from the defect. Also, front surface heat losses can be ignored during this early time.

Numerical Results. For this application, the numerical results for $u(t)$ are shown in **Fig. 2** for several values of R/L at Bi = 0. For each R/L the time t_{\max} at which u has the maximum, u_{\max} , is clearly evident. Values of t_{\max} and u_{\max} are monotonically increasing functions of R/L as demonstrated by the points shown in **Figs. 3** and **4**. In the range $0.5 < R/L < 4$, curve fits for f_1 and f_2 in **Eqs. 9** and **10** were found to be:

$$u_{\max} = f_1(R/L) = \sum_{n=0}^4 a_n (R/L)^n \quad (11)$$

and

$$t_{\max} = f_2(R/L) = \sum_{n=0}^2 b_n (R/L)^n \quad (12a)$$

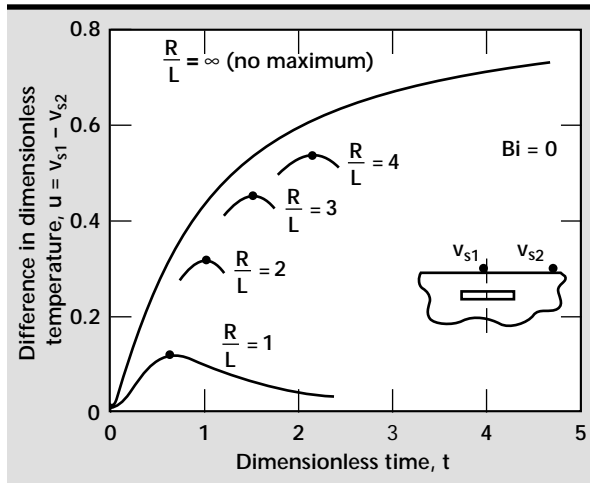


Figure 2. Locus of image contrast maxima.

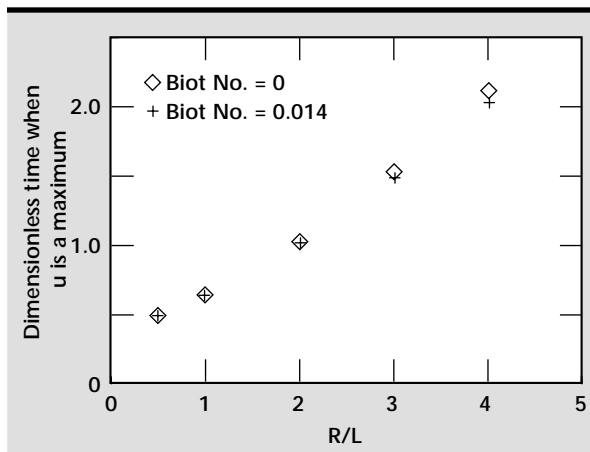


Figure 3. Time for optimal image.

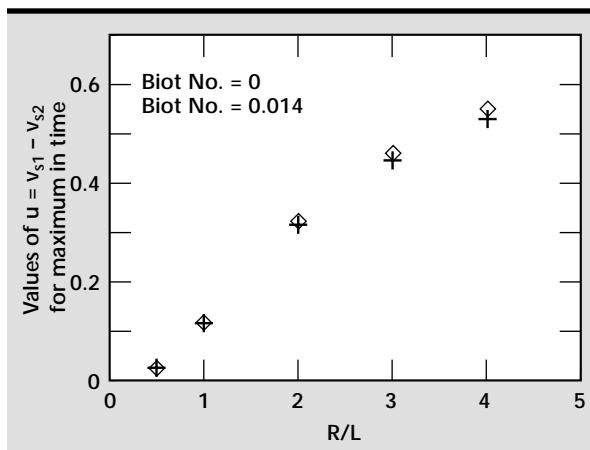


Figure 4. Optimum image contrast.

where the coefficients are given in **Table 1** for $Bi = 0$. The inverse of **Eq. 12a** is obtained as

$$R/L = \frac{-b_1}{2b_2} + \sqrt{\left(\frac{b_1}{2b_2}\right)^2 + \left(\frac{\alpha\tau_{\max}}{L^2} - b_0\right)/b_2} \quad (12b)$$

Application to Curved Surfaces

We also applied the methods to solids other than the flat plate. A cylindrical shell composite was tested and simulated numerically using TOPAZ2D.⁶ The cylinder had a 4-in. nominal diameter and was composed of an outer shell of one material and an inner shell of another. The shell thicknesses are shown in **Fig. 5a**. The two shells had a 0.003-in. interference fit producing a 450-psi pressure where they contacted. There were two parallel circumferential gaps, each about 0.75 in. wide, intentionally made by machining the inner shell, as illustrated in **Fig. 5a**. To be discussed subsequently are the images observed in **Fig. 5a**, which are revealed only along the cylinder's centerline, and their corresponding contrast plotted in **Fig. 5b**. The analytical curve shown in **Fig. 5b** was obtained by ignoring temperature drops across each of the thin shells separating the gap and using Laplace transform methods to solve the resulting differential equations describing unsteady axial conduction within each shell. The methods in obtaining the numerical results curve in **Fig. 5b** were similar to those previously discussed for the flat plate except that an insulated boundary at the inner surface of the inner shell was used for the thin shells and different thermal properties were considered for each shell.

In **Fig. 6** results are shown for calculations performed that simulate a spherical shell composite having a gap between two shells at the apex viewed by the camera. The shell materials and thicknesses were similar to those shown in **Fig. 5a** for the cylinder. The purpose of these calculations was to determine the importance of lamp orientation in sensing gaps for curved parts.

Table 1. Coefficients of Eqs. 11–12a for $Bi = 0$.

N	a_n	b_n
0	-0.000398	0.36
1	-0.02622	0.24
2	0.20242	0.05
3	-0.06958	
4	0.007283	

Application to Cracks

When a crack develops in a material perpendicular to its surface, impulsive lamp heating is an ineffective means of crack detection. For these cases, we evaluated the benefits of steady-state heating and cooling of the material's edges that roughly parallel the length of the crack. The computational

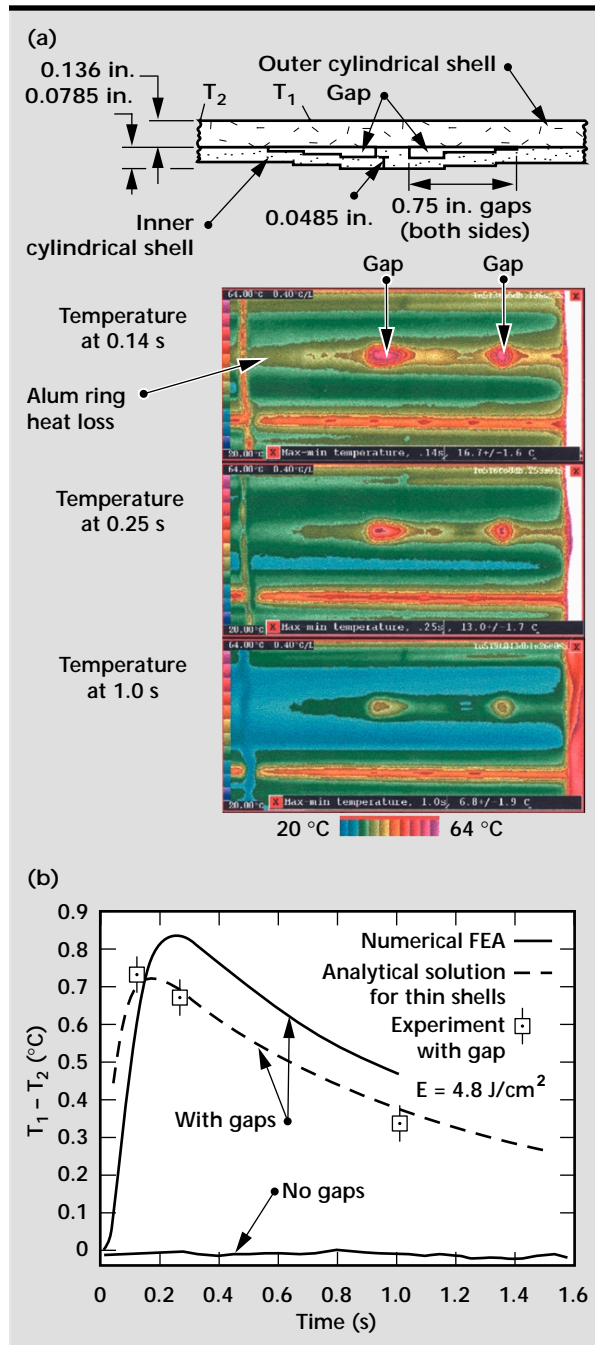


Figure 5. Application to cylindrical shells. (a) Section of composite shell thickness with gaps and images seen by camera; (b) calculated and measured contrast of gap images at top dead center.

model that precedes future experiments is illustrated in Fig. 7. Shown is a segment of a disk of the material under consideration having a circumferential crack whose length runs 10% of its radial location. The center is heated 30 °C higher than the outer periphery is cooled. The hot and cold heat sources may be as simple as heated or chilled rubber water bottles that could be reoriented 90° to

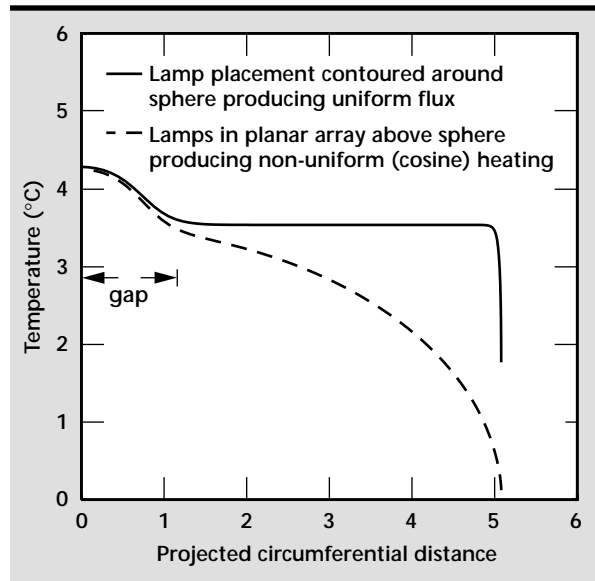


Figure 6. Impact of lamp orientation on gap detection for the sphere.

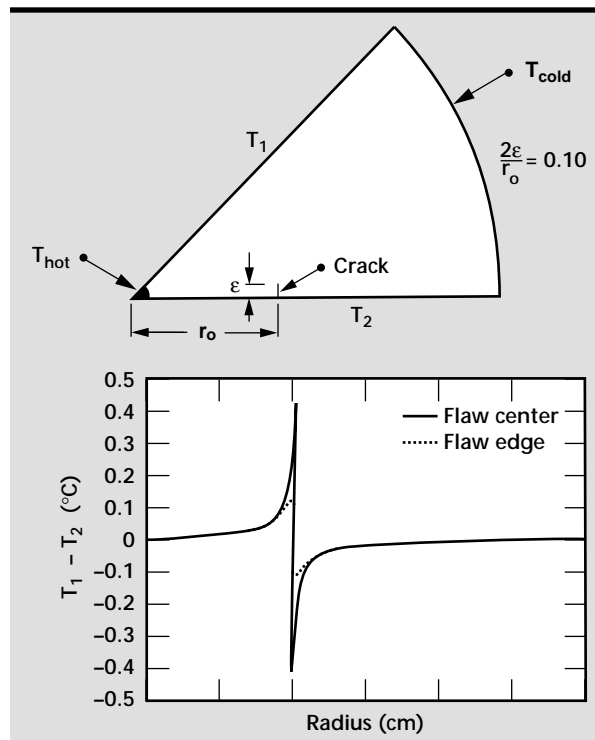


Figure 7. Sensing cracks perpendicular to shell surfaces.

also reveal radially running cracks. The camera would see a simulated contrast as shown in **Fig. 7**, which is within the limits of the measurements.

Experiment

Plate with Defect. The dual-band (centered at about 5 and 10 μm) infrared system,⁷ obtained from Bales Scientific, Inc., has a shrouded, four-lamp array in a square pattern in a plane above and parallel to the surface of the test specimen which was a 12.7-cm-radius stainless disk of thickness 7.62 cm. The stainless steel test specimen containing the circular gap defect was fabricated by back-drilling from the rear face of the 7.62-cm-thick specimen and partially filling with a 2.54-cm-radius stainless slug having a slight interference fit around the periphery. The resulting gap thickness of 0.32 cm was small compared to the gap radius of 2.54 cm. The resulting gap depth was 0.9525 cm. The energy flux imposed on the specimen was 4.84 J/cm^2 , and the lamps were on for about 4 ms. To experimentally resolve the curves shown in **Fig. 2**, their peak values should be no smaller than about 0.6°C since relative temperature differences of about 0.1°C can just be resolved. The gap dimensions illustrated here produced results approaching this measurement limit. Results obtained for smaller depths or

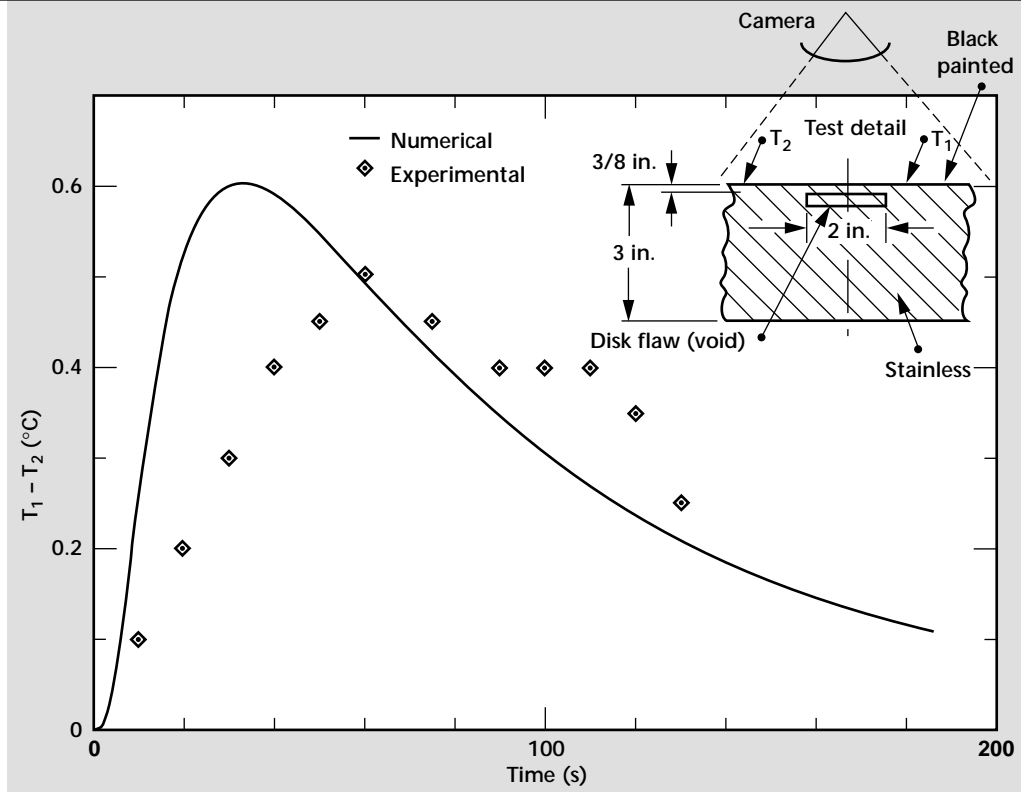
larger gap radii than those considered here are more easily obtained.

For this system, a high emittance (emissivity) coating is desired to mitigate test surface reflected irradiance originating from the heated shroud and from the lamps which are cooling. In the interest of nondestructive evaluation, we require that the coating be easily removed without damaging the surface finish. For this reason, a water-based, black poster paint was brushed on as the coating material. Both the surface of the test specimen as well as that of the calibration plate, a 0.9-cm-thick 6061 aluminum slab, were covered by the same coating. The calibration plate was used to determine the energy flux, which was needed for the analysis in obtaining the product $q_s\tau_0$ which is used to compare experimental and computational results and in the depth determinations.

Cylindrical Shell Composite. The aforementioned cylindrical composite was also tested with the same lamp array used for the plate. Because of the planar lamp array, the cylindrical surfaces were not uniformly heated. The uppermost portion of the cylinder facing the lamp was heated more than lower portions having a less favorable view of the lamps. Discussion is deferred on the consequences of this non-uniform heating.

For reasons also to be discussed subsequently, tests on the cylindrical composite were performed both with and without the black poster paint external coating.

Figure 8. Comparison between numerical solution and experimental results for the plate.



Results

Plate. The calculated and measured transient image temperature contrast, $T_1 - T_2$, is compared in **Fig. 8** for the applicable Biot number of 0.014. The corresponding surface images are shown in **Fig. 9** at times before, during, and after the times when the experimental contrast is near its peak. The comparison in **Fig. 8** reveals that the experimental data lag the calculated results in times prior to about 60 s, which has the effect of increasing the experimental value of τ_{\max} and decreasing the experimental value of $(T_1 - T_2)_{\max}$ relative to their calculated values, as shown in **Table 2**.

The calculated results in **Fig. 8** do not include the presence of the surface coating in retarding the surface images which are produced by conducting subsurface information through the coating. Separate calculations have shown this is

an important effect that depends on coating thickness and thermal conductivity and is responsible for the early-time mismatch between experimental and computational results. Use of a more suitable removable coating having good optical as well as thermal properties is therefore desirable.

Depth Detection. As a consistency check on the method for depth detection, the computed results from **Table 2** were first used to obtain depth L and gap radius R from simultaneous solution of **Eqs. 11** and **12b**. The results for R and L were within 1.8 and 1.9% of their respective actual values, these errors reflecting minor curve-fitting errors associated with **Eqs. 9** and **10**. This same evaluation was repeated using the measured values of **Table 2**, and the results are shown in **Table 3** (second row). Because of the previously discussed coating conductive losses, the depth and gap radius detected using the experimental data are greater than their actual values.

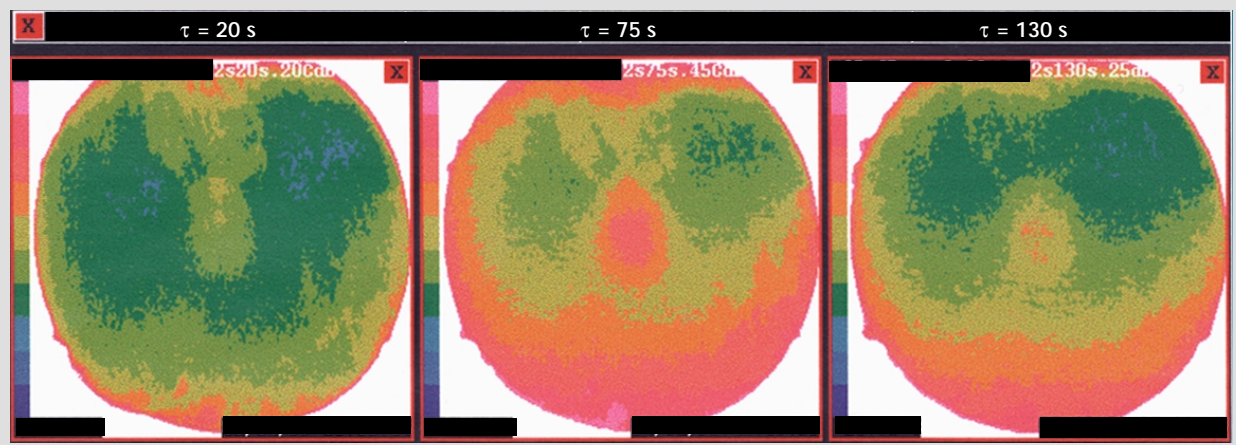


Figure 9. Images before, during, and after peak contrasts.

Table 2. Peak image contrast and time for $Bi = 0.014$, energy flux = 4.84 J/cm^2 , $R = 2.54 \text{ cm}$, $L = 0.9525 \text{ cm}$ in stainless steel.

	Peak contrast, $(T_1 - T_2)_{\max}$ ($^{\circ}\text{C}$)	Time at peak contrast, τ_{\max} (s)
Computed, no conductive coating, temperature drop	0.60	29
Measured, with coating	0.50	60

Table 3. Depth detection; image radius observed, $R^i = 2.65 \pm 0.1 \text{ cm}$.

Method	Depth, L (cm)	Radius, R (cm)
Actual	0.9525	2.54
Simultaneous solution to Eqs. 11–12b	1.24	3.86
Find L from Eq. 11 using $R^i = 2.65 \text{ cm}$	1.06	2.65

An alternative depth estimate based on the experimental data was also made and is reported in the third row of **Table 3**. Here only **Eq. 11** is enforced, and, instead of using **Eq. 12b**, the observed image radius of approximately 2.65 cm is used to obtain the depth L . The error made in this surface image size observation is estimated to be ± 0.1 cm. This produces a much closer depth prediction of 1.06 cm, about 11% higher than the actual depth.

Detection Limits. Equation 11 was evaluated for $L = L(R)$ and the results were plotted in **Fig. 10**. In this portrayal, a fixed value of $(T_1 - T_2)_{\max} = 0.87^\circ\text{C}$ was used as a measure of a contrast that could easily be seen when the system is used in a routine inspection mode. The product of density and specific heat capacity for most metals above room temperature is about $3.5 \text{ J/cc}^\circ\text{C}$, which was also used in constructing **Fig. 10**. At a particular energy flux, depths above the curve are not detectable; those below the curve provide surface images that can be seen. These curves represent the detection limits for metals.

Curved Surfaces. The apparent gaps revealed by the images in **Fig. 5a** appear as spots rather than expected circumferential rings. One possible explanation for the spots is that the lamps, which are arrayed as a planar heating source above the cylinder, produce circumferential temperature gradients that cause the gaps to be undetected except at the centerline where these gradients are small. This effect is demonstrated for the sphere in **Fig. 6**.

Figure 5b demonstrates that predicted and measured contrast factors are in good agreement both with respect to magnitude and time. (The better agreement for the analytical solution is fortuitous

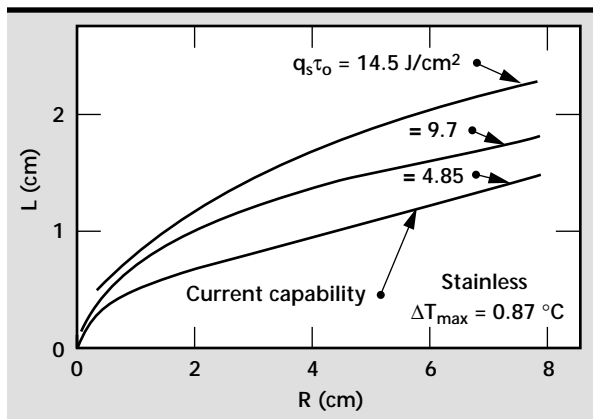


Figure 10. Detection limits for metals at 0.87°C peak contrast (depths L above the curves are not detectable).

because the numerical solution more faithfully represents the thermal problem than does the analytical solution whose approximations were previously described.) The time scales of **Fig. 5b** are less than about 1 s owing to the thin shells having a small thermal capacitance. These times are much smaller (on the order of minutes) than those for the thicker flat plate (see **Fig. 8**).

It is important to mention that the experimental results for the cylinder were obtained for an unpainted, bare outer surface. The painted cylindrical surface produced such weak images that they could not be seen, this caused by the aforementioned coating insulating effect which is significantly exacerbated in the short time scales of 1 s. Even though the measured contrast factor (ordinate of **Fig. 5b**) agreed well with predicted results, we as yet cannot rule out that some or much of the images seen may be artificial and due to reflected irradiance originating from the cooling, unshuttered lamps.

Conclusions


The following conclusions are drawn relating to impulsive surface heating and image observation:

1. Surface images are created by the multidimensional heat flow around the subsurface flaw (gap).
2. An optimum, opportune time, dependent on host thermal diffusivity among other parameters, occurs when the brightest image appears.
3. Subsurface depths are over-predicted, this caused by an insulating effect of the coating used.
4. Detection limits are governed by instrument sensitivity, flaw geometry (depth and transverse size), host density and specific heat capacity and energy flux imposed; the limits are independent of host thermal conductivity.
5. With all other parameters fixed, an increase in energy flux does not return a proportionate increase in detection depth.
6. Curvature effects need to be accommodated by arraying the lamps to conform to the body shape.
7. Low thermal conductivity coatings applied to thin, metallic shells seriously retard the images.
8. If a suitable coating cannot be found for thin shells, it will be necessary to a) blacken (and possibly water-cool) the shroud surrounding the test section and b) shutter the lamps. A shutter must operate within about 100 ms.

Future Work

We have two major challenges: (1) lamps should be arrayed to conform to component shapes, thereby achieving a more uniform heating; and (2) an optical coating needs to be identified that possesses good heat conduction properties yet is removable without surface damage. In absence of such a coating, the lamps will require shuttering and the shroud will need to be water-cooled.

References

1. C. K. Hsieh and K. C. Su (1980), *ASME Trans., J. Heat Trans.*, Vol. **102**, p. 324.
2. C. K. Hsieh and K. C. Su (1981), *ASME Trans., J. Heat Trans.*, Vol. **103**, p. 42.
3. C. K. Hsieh and A. J. Kassab (1986), *Int. J. Heat Mass Trans.*, Vol. **29**, p. 47.
4. C. K. Hsieh, C-Y. Choi and K. M. Liu (1989), *J. Nondestr. Eval.*, Vol. **8**(3), p. 195.
5. D. J. Roth, J. R. Bodis and C. Bishop (1997), *Res. Nondestr. Eval.*, Vol. **9**, p. 147.
6. A. B. Shapiro (1986), Lawrence Livermore National Laboratory, Livermore, California (UCID-20824).
7. L. A. LeSchack and N. K. Del Grande (1976), *Geophys.*, Vol. **41**(6), p. 1318. 

Quantitative Tomography Simulations and Reconstruction Algorithms

Harry E. Martz, Jr.
Center for Nondestructive Characterization

Dennis M. Goodman and Jessie A. Jackson
Laser Engineering Division
Electronics Engineering

Clinton M. Logan
Manufacturing and Materials Engineering Division
Mechanical Engineering

Maurice B. Aufderheide, III and Alexis Schach von Wittenau
Defense and Nuclear Technology

James M. Hall
Physics

Dale M. Sloan
Computation

We are researching, developing, and implementing quantitative imaging tools (radiographic simulations and image reconstruction algorithms) with three main goals in mind. First, they will allow optimization studies to be made for tomography equipment to optimize geometry, source, and detector choices. Second, the simulation tools will allow more accurate corrections to be made to experimental radiographs resulting in very accurate tomographic image reconstructions. Third, these tools will be integrated with existing reconstruction routines to build state-of-the-art forward-modeling tomographic image reconstruction codes. These codes will use a constrained-conjugate-gradient (CCG) algorithm to perform reconstructions with complete and limited numbers or portions of views. By merging the simulation capability with the CCG reconstruction technique, we will have a physics-based, forward-model image reconstruction code.

Introduction

Transmission radiography and tomography are important diagnostic tools at the heart of Lawrence Livermore National Laboratory (LLNL)'s effort to meet the DOE DP-10 Advanced Radiography Campaign goals. This campaign seeks to improve radiographic simulation and analysis so that radiography can be a useful quantitative diagnostic tool for stockpile stewardship.

This project will advance tomographic imaging capabilities in LLNL programs. Current radiographic accuracy does not allow us to satisfactorily separate experimental effects from

features of the radiographic or tomographic reconstructed object image. This can lead to difficult and sometimes incorrect interpretation of radiographic and tomographic image results.¹⁻³ By improving our ability to simulate the whole radiographic and tomographic system, it will be possible to examine the contribution of system components to various experimental effects, with the goal of removing or reducing them. By merging this simulation capability with a maximum likelihood constrained-conjugate-gradient (CCG) reconstruction technique, we will have a physics-based, forward-model image reconstruction code.

Forward-modeling techniques are being explored in a variety of places. This project is unique in its physics simulation approach, in its use of CCG to reconstruct 2-D and 3-D meshes, and in the breadth of data to which it will be applied and tested. This includes x-ray, neutron⁴⁻⁶ and proton radiographic data. The ability to make quantitative attenuation-image reconstructions will be attractive to many applications leading to new collaborations in earth science, plant science, medicine, material development, manufacturing, and defense.

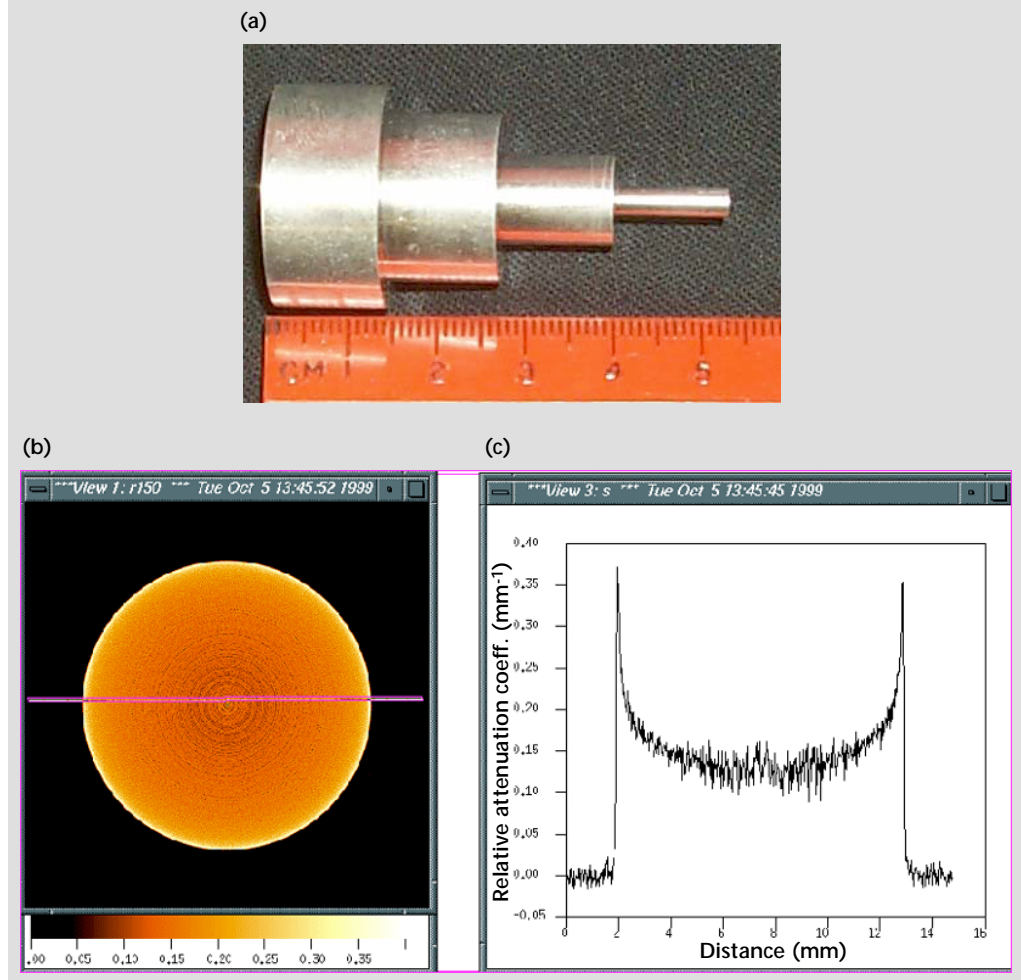
Current computed tomography (CT) image reconstruction back-projection methods make strong assumptions about the radiographic projection data. These assumptions include energy-independent photon attenuation cross-sections, no detector or source-spot blur, no scattering, no noise or artifacts. None of these assumptions is strictly correct. Radiation attenuation cross-sections depend strongly on energy and material composition; detector and source-spot blur is usually significant; scattering is present; noise and artifacts are common.

Some of these assumptions can be treated in the forward model of a reconstruction algorithm. In this project, we seek to improve the accuracy of CT from transmission radiographs by studying what physics is needed in the forward model.

Presently, accuracy in attenuation estimates of roughly a few percent is possible, over a volume whose length is on the order of 1/1000 the object characteristic length. A simple example of a magnesium (Mg) phantom is shown in **Fig. 1**. The tomography projection data was acquired using KCAT, a CT scanner that consists of a 160-kV microfocus x-ray source and a scintillator lens coupled to a CCD camera detector system. The source-to-detector distance for the Mg phantom study was 92 mm, with the object 15 mm in front of the detector. The source was set to 75 kV and 0.12 mA and was filtered with 76 μm of Al. The total data acquisition time was ~ 5 h for 360 projections over 360° . The data was reconstructed using a convolution back-projection (CBP) algorithm. The CT image shown in **Fig. 1** to first order appears to be a uniform x-ray attenuating disk as expected. The CT image also shows a nice sharp

Figure 1.

(a) Photograph of a Mg phantom for the Mg tensile bar CT study. The phantom is made of 99.9% pure Mg of density 1.74 g/cm^3 . From left to right the outer diameter of the rod is 25.28, 19.05, 10.16, and 3.31 mm. (b) CBP reconstructed image for the Mg phantom. (c) The 1-D profile for the line shown in the CT image.



edge. However, closer analysis of the image and the profile reveals that there are ring and cupping artifacts. The ring artifacts are reduced by processing the sinogram⁷ before image reconstruction. The ring-removed CT image is shown in **Fig. 2a**.

The cupping artifact results in relative linear attenuation coefficient values that are greater than 100% (near the edges) of the mean, $0.14 \pm 0.02 \text{ mm}^{-1}$. (The means and standard deviations in this report were determined from a 374×337 extracted rectangle from within the CT slice plane.) This profile should be flat since the phantom is 99.9% Mg with uniform density.

This so-called cupping artifact is due to x-ray beam-hardening and scattering. Most of this can be accounted for by applying a beam-hardening correction¹ as shown in **Fig. 2c**. Even when this data is corrected for rings and beam hardening the standard

deviation within the uniform part of the CT image (see central portion of the profile in **Fig. 2d**) is on the order of 17%, $0.29 \pm 0.5 \text{ mm}^{-1}$. We are developing and applying better simulation and reconstruction tools to make a more complete characterization of the system and its components, and are striving to achieve accuracies to better than 1%. It is possible to attempt this goal now because radiographic simulation, CT, and computers have matured sufficiently.

Technical Approach

Radiography Modeling. This project has two main aspects. First, we are accurately modeling the process of x-ray transmission radiography, enabling us to accurately assess and mitigate experimental effects that compromise CT image reconstruction from radiographs. This modeling effort uses three

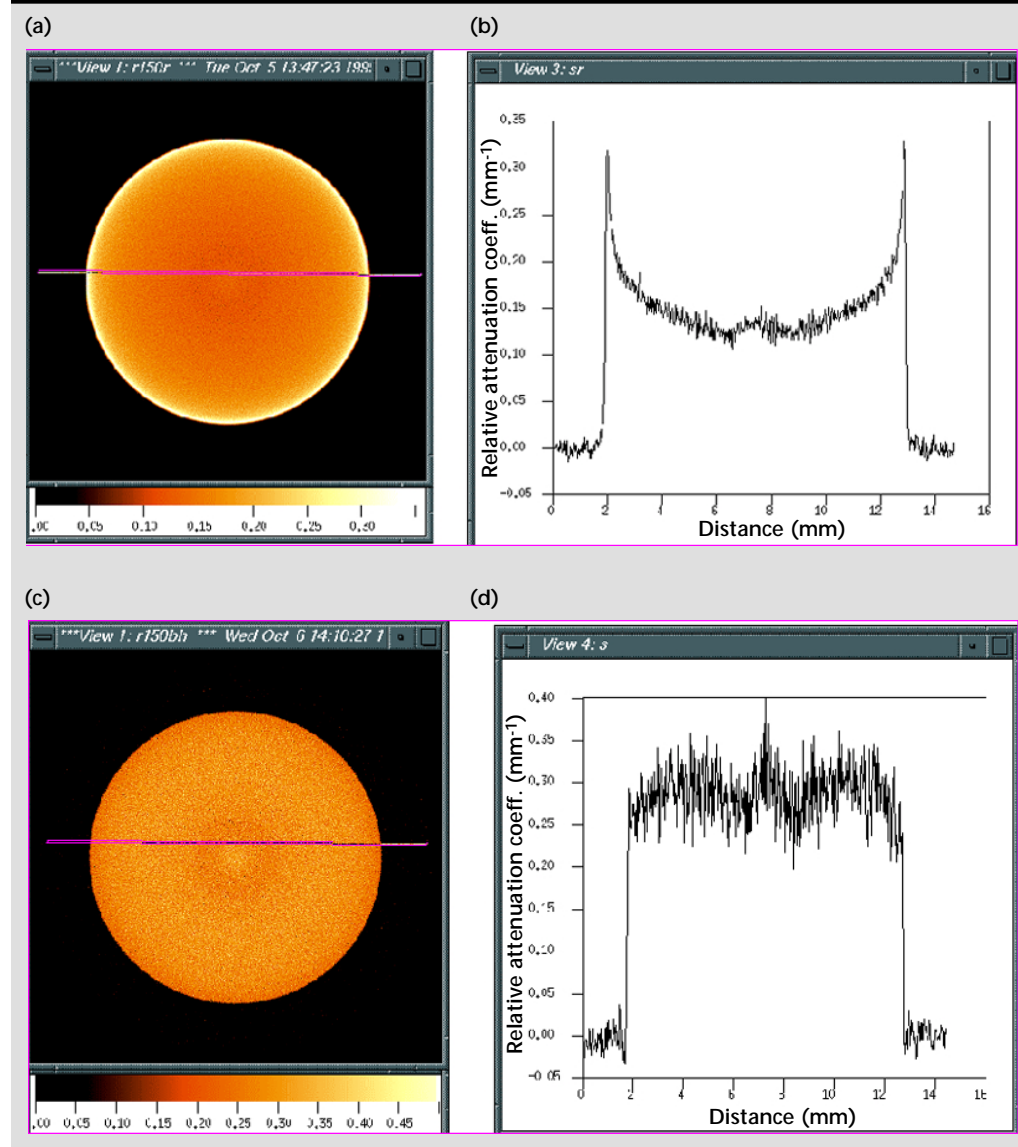


Figure 2. (a) CBP reconstructed image after ring removal applied to the sinogram for the Mg phantom. (b) The 1-D profile for the line shown in the CT image. (c) CBP reconstructed slice after ring removal and beam hardening was applied to the sinogram for the Mg phantom. (d) The 1-D profile for the line shown in the CT image.

simulation codes, HADES,⁸ COG,⁹ and MCNP.¹⁰ Our suite of experimental digital radiography (DR)/CT systems and image reconstruction algorithms are being used to study how experimental effects produce reconstruction artifacts. Radiographic simulation tools have been used to a limited extent^{8,11-14} for assessing experimental effects and have been helpful in analyzing experimental CT images. In this project we will extend our simulation capabilities.

HADES is a radiographic simulation code that uses ray-tracing techniques to compute radiographs through a mesh.⁸ The full geometry of cone beams is treated exactly. A variety of meshes, including 3-D Cartesian meshes, can be ray-traced by the code. In addition, objects such as spheres, cones, cylinders, and plates can be added to the problem as defined by the user. Blur from detectors and finite-spot-size sources is included in the simulation by convolution. Sources of any arbitrary input spectrum can be specified and the spectrally dependent transmission is computed using energy groups.

Using exposure conversion curves, HADES is able to compute, for a given input photon fluence and spectrum, the energy deposited at the detector plane, adding the appropriate statistical fluctuations, if requested. HADES also can simulate GeV-proton radiography and will soon have a low-energy neutron simulation capability. Because HADES uses ray-tracing techniques, it can simulate radiographs very quickly. Hence it is useful as an iterative tool.

Some aspects of x-ray physics are not adequately included in HADES, particularly scattering, secondary Bremsstrahlung, and detailed detector response. A Monte Carlo approach, such as COG, is needed to better understand how scattering and secondary Bremsstrahlung may be incorporated into HADES.

COG is a detailed Monte Carlo neutron, photon and electron transport code capable of providing accurate answers to complex deep-penetration (or shielding) problems.⁹ Unlike many of its predecessors, COG is free of the physics compromises and approximations traditionally used in radiation-transport codes. The COG code is fully 3-D, uses point-wise-correct cross-sections and exact angular scattering functions and provides the user with a full range of statistical biasing options to speed up problem solving. Problem geometries can be set up manually using simple but powerful constructs (more than 30 complex pseudo-surfaces such as boxes, spheres, cylinders, and cones are included in COG's geometry package as elementary types) or developed using CAD tools and then transformed automatically into the proper input format. Geometrical elements in a problem can be visualized

in both cross-sectional and perspective views to ensure fidelity, and complex geometries can be debugged on a standard desktop computer. COG allows users to score the results of a simulation using a number of built-in detector types (for example, boundary crossing detectors, reaction detectors, point flux estimators, or pulse detectors) or specialized, user-written detector packages linked in at run time (for example, radiographic imaging detectors).

The ultimate accuracy of a COG simulation is limited only by the accuracy of the data contained in its reference libraries. COG's accuracy and reliability have been verified by extensive benchmarking on radiation shielding and nuclear criticality problems relevant to LLNL programs.

In this project, we are extending the existing radiographic imaging capability of COG to handle a wider range of object thicknesses (for example, optically thick objects, greater than 3 to 4 mean free paths). Accurate Monte Carlo imaging requires a very large number of simulation particle histories. For example, on the order of 10^{10} histories are required to simulate a 1-k \times 1-k detector with 1% statistics. This will require Accelerated Strategic Computing Initiative (ASCI) level computational resources.

We are simulating radiographs of phantoms using COG, MCNP and HADES. COG and MCNP are being used to determine what experimental factors have the largest effect on the blur and scattering profiles. The source and detector blur and aspects of the problem that do not have a large effect on scattering can be iterated many times with HADES, while still including COG's or MCNP's blur and scattering profiles. This required developing a data link between the Monte Carlo codes and HADES so that the Monte Carlo estimates of scattering can be incorporated into HADES simulations. In addition, the Monte Carlo codes are used to calibrate any approximate blur and scattering treatments implemented by HADES. The Monte Carlo and HADES simulated radiographs are validated by comparison with DR using phantoms.

Phantoms. Key parts of this work are the DR and CT phantoms or test objects, helpful in understanding and validating the simulation codes. The phantoms were designed to meet several criteria: ability to be simulated by COG, MCNP and HADES; ease of fabrication; adaptability to different types of problems; and presentation of a challenging imaging situation.

CT Algorithms. The second aspect of this project involves merging the improved version of HADES with a recently developed CT method based on our CCG optimization algorithm.¹⁵ This approach expresses the image reconstruction problem as a large matrix equation relating a model for the object being reconstructed to its projections (radiographs).

The CCG algorithm is used to seek a maximum likelihood solution. The search continues until the match between the measured projections and the calculated projections is satisfactory. A flow diagram of the tomographic image reconstruction process to recover an object function from radiographic projections is shown in **Fig. 3**.

CT reconstruction involves solving an inverse problem that yields an image or recovered object, which is in some sense a best match to the observed data. The goal is to obtain a good estimate of the true object \mathbf{o} . The problem of reconstructing an object from the observed data can be described as follows: given the observed data vector \mathbf{p} , reconstruct an estimate of the object, represented by the vector $\hat{\mathbf{o}}$, that produced this data. The statistical relationship between $\hat{\mathbf{o}}$ and \mathbf{p} can be written as $L(\mathbf{p}, \hat{\mathbf{o}})$, where $L(\cdot, \cdot)$ is a negative log-likelihood function.¹⁶ The function $L(\cdot, \cdot)$ is determined by the physics of the property being measured, the geometry of the measurement system, and the statistics of the noise corrupting the data. The maximum likelihood solution for estimating \mathbf{o} from \mathbf{p} is

$$\hat{\mathbf{o}} = \underset{\tilde{\mathbf{o}}}{\text{Argmin}} \{L(\mathbf{p}, \tilde{\mathbf{o}})\}, \quad (1)$$

where the vector $\hat{\mathbf{o}}$ yielded by the Argmin operator is the value of $\tilde{\mathbf{o}}$ that minimizes $L(\mathbf{p}, \tilde{\mathbf{o}})$.

The difficulty with this estimate of \mathbf{o} is that most inverse problems are ill-posed in the sense that small changes in \mathbf{p} may produce large changes in $\hat{\mathbf{o}}$. This is especially true of limited data CT reconstructions. Consequently, $\hat{\mathbf{o}}$ typically is too large and very noisy. A common method for obtaining better estimates is the regularization or penalized likelihood approach that adds Euclidean norm and/or absolute value norm terms to $L(\mathbf{p}, \hat{\mathbf{o}})$. These terms penalize

large $\hat{\mathbf{o}}$. Frequently regularization is not sufficient to yield a high quality reconstruction, so any additional prior information about the unknown must be included. Many properties such as energy, absorption, and reflection are inherently non-negative, and adding this constraint often greatly enhances reconstruction quality. Furthermore, there often are physical reasons for placing upper bounds on the estimate. The result is upper and lower bounds for each component of the object vector $\hat{\mathbf{o}}$. If we denote the set of \mathbf{o} vectors that obey the bound constraints by S , then our modified maximum likelihood problem is

$$\hat{\mathbf{o}} = \underset{\tilde{\mathbf{o}} \in S}{\text{Argmin}} \left\{ L(\mathbf{p}, \tilde{\mathbf{o}}) + \eta \|\tilde{\mathbf{o}}\|_1 + \lambda \|\tilde{\mathbf{o}}\|_2 \right\}, \quad (2)$$

where η and λ are Lagrange multipliers that control, respectively, the degree of absolute value norm and Euclidean norm regularization.

A second problem is the dimensionality of **Eqs. 1** or **2**. The discretized object usually contains 10^5 to 10^7 pixels (voxels) resulting in an \mathbf{o} vector of the same length. Conventional nonlinear minimization algorithms use Newton or quasi-Newton techniques that require storing an approximation to the inverse of the matrix of second partials of $L(\mathbf{p}, \hat{\mathbf{o}})$ with respect to $\hat{\mathbf{o}}$. Because even a $10^5 \times 10^5$ matrix is too large to store in memory, these techniques are not appropriate for the inverse problems we are considering.

In the case of an unconstrained problem, such as **Eq. 1**, either the conjugate gradient algorithm, which in effect builds up second derivative information without directly storing it, or limited-memory quasi-Newton algorithms, which store a low rank approximation to the inverse matrix of second partials, are the methods of choice when the dimensionality is too large for conventional quasi-Newton methods.

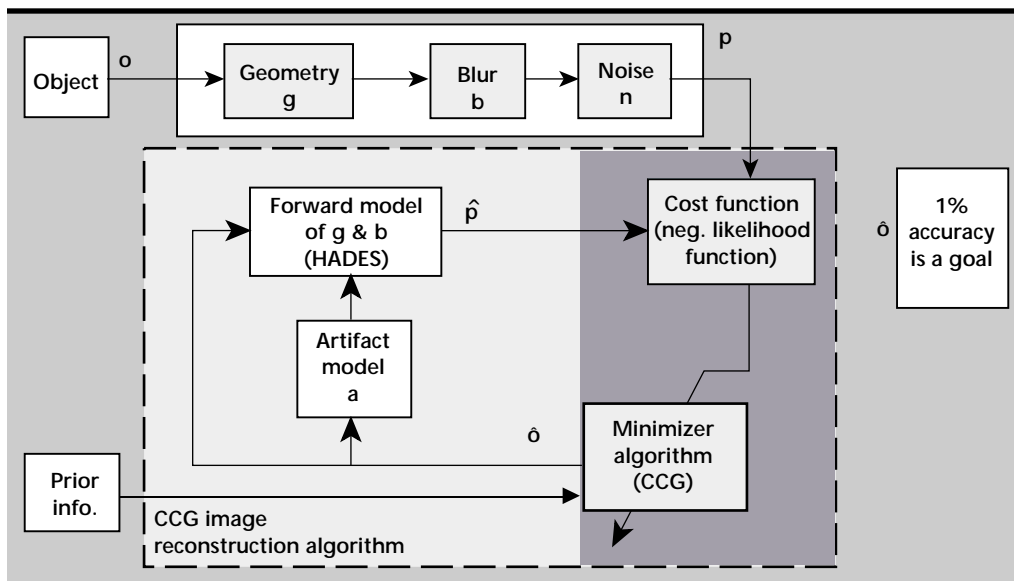


Figure 3. Flow diagram of the process for recovering an object function from radiographic projection data using the CCG image reconstruction algorithm. Details of this diagram are provided in the text. The circumflex ($\hat{\cdot}$) appearing over some parameters indicates they are estimated quantities.

For constrained problems, such as **Eq. 2**, conventional optimization techniques usually allow only one variable per iteration to attain a bound, so for very large bounded inverse problems these techniques are very slow since they spend too much effort finding bounds. Consequently, standard approaches to inverse problems use the projection onto convex sets (POCS) algorithm,¹⁷ the expectation-maximization (EM) algorithm,¹⁸ or variants of the algebraic reconstruction technique (ART).¹⁷ These methods can attain multiple bounds in an iteration, but they essentially use a steepest descent strategy and converge very slowly, sometimes not at all.

We have developed an extension of the conjugate gradient algorithm that incorporates bound constraints on the variables.¹⁵ It is unique in that it incorporates a bending line search, which allows multiple variables per iteration to attain bounds. Given the dimensionality of our problems of interest, this is a major advantage over the conventional techniques. Our algorithm has been applied with great success to a variety of practical problems.^{15,19}

We have also developed a limited memory quasi-Newton algorithm that uses the same bending line search as our CCG algorithm, using matrix updates.²⁰ The choice of algorithm is problem dependent. Our conjugate gradient algorithm requires an accurate line search to ensure fast convergence. Fortunately, it is possible to take advantage of the special structure of most tomography problems to greatly reduce the effort required by the line search.²¹ On the other hand, when symmetries or complicated prior information are applied to the reconstruction problem, or when blurring occurs in the projection data, the special structure may no longer apply, and our quasi-Newton algorithm is usually a better choice.

CT Imaging Artifacts. Our work on improving the accuracy of tomographic reconstructions is highly dependent on improved reconstruction algorithms. This year we have concentrated on three issues: reducing artifacts, mitigating the effects of beam hardening, and compensating for blur. These issues are highly complex, and we will continue our work on them in FY-00.

The problems our techniques have been designed to handle can be described as follows. First there is a deterministic model of the relationship between the unknown object and the projection data:

$$\hat{\mathbf{p}} = h(\hat{\mathbf{o}}) \quad (3)$$

where the vector $\hat{\mathbf{o}}$ represents an estimate of the unknown object we wish to reconstruct, and h is a function that represents such effects as geometry, g , and absorption that lead to the expected data $\hat{\mathbf{p}}$ that would result if $\hat{\mathbf{o}}$ were the true object. The actual

observed data is \mathbf{p} , and the estimate of the true object is obtained by using an optimization algorithm to adjust $\hat{\mathbf{o}}$ so that $\hat{\mathbf{p}}$ is a best fit to the actual data according to some criterion function, say

$$f(\mathbf{p}, \hat{\mathbf{p}}). \quad (4)$$

where the choice of the criterion function depends on the statistics of \mathbf{p} . Consequently, our reconstruction problem involves minimizing with respect to a function of the form

$$L(\mathbf{p}, \hat{\mathbf{o}}) = f(\mathbf{p}, h(\hat{\mathbf{o}})). \quad (5)$$

If $L(\mathbf{p}, \hat{\mathbf{o}})$ is the negative log-likelihood function, the recovered object is the maximum likelihood estimate of the unknown.

Artifacts in a reconstructed object are frequently caused by outliers in the observed projection data \mathbf{p} . These outliers can result from mismodeling the imaging system, bad detectors, and “hits” from extraneous radiation. The maximum likelihood method is generally highly sensitive to outliers. Robust statistical methods²² involve modifying $f(\mathbf{p}, \hat{\mathbf{p}})$ to make the resulting estimator much less sensitive to outliers, yet have it perform almost as well as maximum likelihood in the absence of outliers. For tomography systems that are photon rich, the typical assumption is that noise on the observed projection data \mathbf{p} is, in the absence of outliers, Gaussian with constant variance. The maximum likelihood principle leads to applying a least-squares fit between the observed data \mathbf{p} and the modeled data $\hat{\mathbf{p}}$. The squared error function is

$$f(\mathbf{p}, \hat{\mathbf{p}}) = \sum_{i=1}^N r_i^2 = \mathbf{r}'\mathbf{r}, \quad (6)$$

where the *residual* vector $\mathbf{r} = \mathbf{p} - \hat{\mathbf{p}}$ is one indication of mismatch between the observed data and the model of the data. Unfortunately, this criterion function is very sensitive to outliers. For example, suppose $N=10,000$ in **Eq. 6**, and the magnitude of a typical component of the residual is 1.0, except for one component r_k whose value is 100.0. Then r_k contributes roughly as much to the squared error as do all the other components combined, and the minimization algorithm will try very hard to match the outlier at the expense of all the other data points.

The most common robust criterion is

$$f(\mathbf{p}, \hat{\mathbf{p}}) = \sum_{i=1}^N g(r_i), \quad (7a)$$

where

$$g(r) = \begin{cases} r^2 & \text{if } |r| \leq c \\ 2c|r| - c^2 & \text{if } |r| > c \end{cases}. \quad (7b)$$

The function $g(r)$ transitions smoothly from a squared penalty to a linear penalty, thereby reducing the influence of large residuals. The choice of c is data dependent.²² We have demonstrated both that CCG is very effective in minimizing **Eq. 5** when **Eq. 7** is the criterion function and that this approach greatly improves reconstruction quality in the face of outliers. The effectiveness of CCG has permitted—to our knowledge—the first successful application of robust statistical techniques to tomographic inverse problems.

Adding a saturation region to **Eq. 7b** for very large data mismatches results in the criterion function:

$$g(r) = \begin{cases} r^2 & \text{if } |r| \leq c \\ 2c|r| - c^2 & \text{if } c < |r| \leq d \\ 2c|d| - c^2 & \text{if } |r| > d \end{cases} \quad (8)$$

This function is even more robust in the face of very large outliers than is **Eq. 7b**. Unfortunately, using **Eq. 8** makes $L(\mathbf{p}, \hat{\mathbf{o}})$ a nonconvex function of $\hat{\mathbf{o}}$; consequently, it has local minima. Typically, using $g(r)$ as in **Eq. 8** and starting with $\hat{\mathbf{o}} = \mathbf{0}$ results in convergence to a local minimum and a meaningless reconstruction.

One solution is first to solve the problem using **Eq. 7b**; then use the resulting $\hat{\mathbf{o}}$ as a starting point for the problem defined by using **Eq. 8**. We have found this approach to be satisfactory, although there is no guarantee of convergence to the exact global minimum.

This year we have demonstrated that robust techniques show great promise for artifact reduction in tomography, but much work remains to be done. We intend to study other robust criteria. For example, changing the saturation region in **Eq. 8** to a zero response region would force the reconstruction algorithm to pay no attention whatever to very large residuals, but local minima would be an even more serious problem. In the cases of photon-starved x-ray tomography, neutron and proton tomography, and emission tomography, the appropriate noise model is Poisson, not Gaussian. The residuals do not appear directly in the Poisson likelihood function, so the functions in **Eqs. 7b** and **8** are not immediately useful. In particular **Eq. 7a** must be replaced by

$$f(\mathbf{p}, \hat{\mathbf{p}}) = \sum_{i=1}^N p_i \log \hat{p}_i - \hat{p}_i, \quad (9)$$

to obtain the maximum likelihood estimate.²³ There is no clear best approach to making the Poisson likelihood function robust though several possibilities exist.^{22,23}

Beam Hardening. Another cause of artifacts in reconstructions is due not to data errors but to mismodeling. The model for the intensity or energy,

I_1 , deposited on a detector for a polychromatic x-ray source for a single ray projection is given by

$$I_1 = I_0 \int T(E) \exp \left\{ - \int_L a(l, E) dl \right\} dE, \quad (10)$$

where I_0 is the incident intensity or energy on the object, $a(l, E)$ is an attenuation function that depends both on the position l along the ray and the spectral frequency or energy E , and $T(E)$ is the spectral energy distribution function of the x-ray source.²⁴ The value of $a(l, E)$ at each point l along the ray depends on the densities and absorption characteristics at spectral frequency E of each material present at location l . Most reconstruction algorithms neglect the effects of a polychromatic source and use the simplified model

$$I_1 = I_0 \exp \left\{ - \int_L a(l) dl \right\}. \quad (11)$$

Unfortunately, the absorption of most materials is a strong function of x-ray spectral frequency with absorption generally being higher at lower spectral energies. Consequently the spectral distribution at the detector is different from that at the source. This phenomenon is called beam hardening or spectral hardening, and use of **Eq. 11** rather than **Eq. 10** can lead to severe artifacts (see **Fig. 1**). If we let the data vector be the logarithm of the detector data described by **Eq. 11**, then the discretized version of **Eq. 11** leads to the following simple linear model for **Eq. 3**:

$$\hat{\mathbf{p}} = \mathbf{B}\hat{\mathbf{o}}, \quad (12)$$

where the matrix \mathbf{B} represents the geometric relationship between object voxel and detector position. The usual approach to reducing the effects of beam hardening artifacts is to solve the problem defined by **Eq. 12**, correct for beam hardening in the logarithmic data vector, and then solve the problem once again by fitting the corrected data vector (see **Fig. 2c** and **d**).

In the first half of this year we developed a much better approach to avoiding beam hardening artifacts using the original detector data (we took no logarithm) and a discretized version of **Eq. 10** for **Eq. 3**. For the single material case, the model was

$$\hat{p}_i = \sum_{k=1}^{Nfreq} I_k \exp \{ - \mu_k \mathbf{b}_i \hat{\mathbf{o}} \}. \quad (13)$$

In **Eq. 13** we divided the x-ray frequency spectrum into $Nfreq$ bins so that I_k was the incident energy in the k^{th} bin and μ_k is the mass absorption coefficient for the k^{th} bin. The row vector \mathbf{b}_i is the i^{th} row of the geometry matrix \mathbf{B} , and $\hat{\mathbf{o}}$ is the unknown vector of material densities.

We have implemented this model, and we have demonstrated that it is a superior method for mitigating the effects of beam hardening on reconstructions of simulated data. We achieved this success because both our CCG and our limited-data quasi-Newton algorithms were able to deal with this highly nonlinear model, whereas the usual steepest descent approaches typically failed.

We also considered the multiple material case in which \mathbf{o} becomes:

$$\mathbf{o} = \begin{bmatrix} \mathbf{o}^1 \\ \vdots \\ \mathbf{o}^{Nmat} \end{bmatrix}, \quad (14)$$

where there are $Nmat$ materials, and o_j^m is the density of the m^{th} material in the j^{th} voxel.

This leads to the model

$$\hat{p}_i = \sum_{k=1}^{Nfreq} I_k \exp \left\{ \sum_{m=1}^{Nmat} \mu_k^m \mathbf{b}_i \mathbf{o}^m \right\}, \quad (15)$$

where μ_k^m is the absorption of the m^{th} material in the k^{th} spectral bin. Unfortunately, the multiple material problem is highly ill-posed and our algorithms converged slowly to poor reconstructions. This is not surprising: by assuming $Nmat$ materials we increase the number of unknowns by a factor of $Nmat$ over the single material case, but the amount of data stays the same.

In the case where the region of each material in the object is known, our bound constraints can be used to make the problem better behaved. If these

regions are not known, spectrally selective detectors can be used to increase the amount of data at each detector location. We successfully used spectrally selective detectors to solve an important waste drum tomography problem.^{25–27} This work is currently being commercialized. Not only will this approach mitigate beam hardening, it also has the possibility of localizing or detecting materials in an unknown object. We will continue this work in FY-00.

Blur reduction. For many tomography problems blurring of the projection data is a serious issue. This blurring can be induced by finite beam spot size and other phenomena in the imaging system. This year for the blurring problem we neglected beam hardening issues and focused solely on the linear model described by Eq. 12. Blurring may be removed with a deconvolution algorithm prior to applying a reconstruction algorithm; however, an approach that is both more computationally efficient and more appropriate statistically is to fold both the blur model and the projection model into the deterministic model of the relationship of the object and the data shown in Eq. 3. Let the noise-free and blur-free projection model be given by

$$\mathbf{u} = \mathbf{B}\mathbf{o} \quad (16)$$

where \mathbf{B} is the geometry matrix defined earlier. Now let the blurring model be given by:

$$\hat{\mathbf{p}} = \mathbf{C}\mathbf{u}, \quad (17)$$

where $\hat{\mathbf{p}}$ is the modeled blurred projection data and

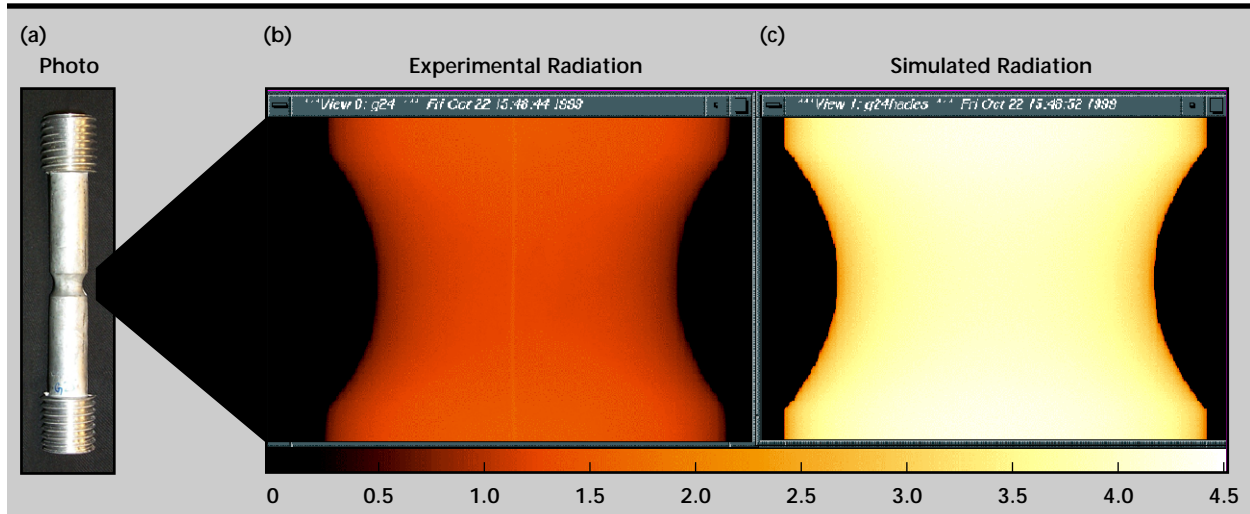


Figure 4. (a) Photograph of a cast Mg-alloy tensile bar. The bar is 11.5-cm long with a maximum diameter of 1.8 cm. (b) An experimental radiograph of a Mg tensile bar obtained by KCAT with a 75-kV source and a 0.08-mm Al filter. (c) A HADES simulated radiograph of the Mg-alloy tensile bar obtained with a 75-kV source and 0.08-mm Al filter.

\mathbf{C} is a matrix representing the point spread function (PSF) that caused the blur. **Equation 3** now becomes

$$\hat{\mathbf{p}} = \mathbf{A}\hat{\mathbf{o}}, \quad (18)$$

where $\mathbf{A}=\mathbf{CB}$. Because **Eq. 18** must be computed many times in either of our two optimization algorithms, computational efficiency is a serious issue. **Equation 16** represents a collection of line integrals, so \mathbf{B} usually is very sparse. Furthermore, if the blurring function is shift invariant, which is usually the case for x rays and some times the case for neutrons but not the case for protons, then **Eq. 17** can be calculated using FFTs. Therefore, calculating **Eq. 16** and then **Eq. 17** may be more efficient than implementing **Eq. 18** directly.

This year we have developed a FFT-based implementation of **Eq. 17** and its adjoint (which our algorithms also require) and we have used this implementation to develop a highly effective deconvolution algorithm that permits use of all the possible criterion functions that we have described above. We have successfully applied this algorithm to astronomical data. In the future we intend to merge our blurring model with the beam hardening models described above.

First Year Accomplishments

Implementation of HADES. HADES has been ported to computers to be used for radiographic and tomographic simulation studies. The first project for which the code has been used is to model a Mg alloy (AM60, ~6% Al) tensile bar. Cast light metals, Al and Mg, are being used in

an ever-increasing number of applications to reduce automobile weight for improved gas mileage and lower emissions. The tensile bars are used for material strength testing. Notched Mg tensile bars are being characterized by radiographic and tomographic imaging before and after mechanical testing.²⁸ The damage in these bar specimens will first be determined using CT and subsequently by metallography analysis intended to benchmark the CT technique.

Low-energy radiographs have been taken of the bars for tomographic image reconstruction as shown in **Fig. 4b**. HADES is being used to generate synthetic radiographs of notched Mg bars with defects, to determine the smallest defects that can be characterized by CT. This will help understand the CT performance, and segmentation methods of CT data and conversion to finite-element analysis (FEA) meshes.

We simulated a radiograph of a pure Mg tensile specimen using the actual object and scanner (512×768 pixels, 0.0218-mm pixel size, 77-mm source-to-object distance and 92-mm source-to-detector distance (sdd)) geometries. The source was modeled at 75 kV with 0.08-mm Al filter. The detector efficiency was determined and included into the HADES simulation. The PSF of the detector was not determined and thus was not included into the HADES simulation. The resultant simulated radiograph is shown in **Fig. 4c**. We are currently incorporating the actual CT spectrum and detector response.

Experimental Set-Up. For our experimental work we have focused on using LLNL's 9-MV LINAC.

Recently, commercial detector arrays have become available that are based on fabrication methods developed for flat-panel displays. Early this fiscal year we began evaluation of an amorphous-Si (a-Si) array made by *dpix*²⁹ for use with the 9-MV Bremsstrahlung spectrum. These preliminary results are so exciting (see **Fig. 5**) that we have decided to use the *dpix* "Flashscan 20" detector for our experimental work.

The Flashscan 20 is a flat-panel array of light-sensitive photodiodes using thin film transistors. The Si is amorphous, resulting in good radiation resistance. The active area of the 12-bit a-Si array is $19.5 \text{ cm} \times 24.4 \text{ cm}$, with 1536×1920 pixels of size $127 \times 127 \text{ }\mu\text{m}$. This array must be used with a scintillator to convert x-ray radiation energy to visible light. We have selected a commercial mammography "screen", Min-R, as having the best spatial resolution and sensitivity for this application.³⁰

Phantoms. We selected the following test objects:

Cu-step wedge—We designed and fabricated a

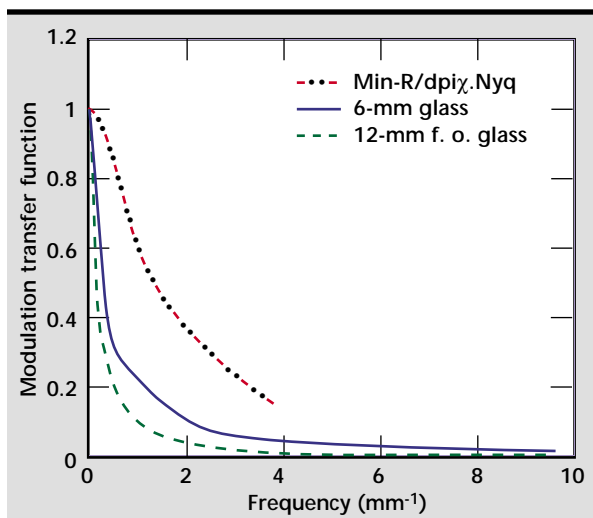


Figure 5. Experimentally determined MTF of a radiographic 3.175-mm-thick depleted-U edge for the Min-R/*dpix* detector system and two scintillator/lens/CCD detector systems at LLNL.

step wedge with Pro-E software, fabricated from certified CDA 110 Cu, inspected and density verified. The wedge is 101.7 mm wide and 175.0 mm long. A solid model with as-inspected thickness for each step is shown in **Fig. 6**. A full inspection report with perpendicularity and parallelism is available by request to logan2@llnl.gov.

Ta edge—An edge is a widely used configuration with which to evaluate the frequency response of an imaging system. The edge-spread function (ESF) and the modulation transfer function (MTF) are derived from the image of an edge. Ideally one desires the edge to be very highly attenuating for the incident x rays and to be of zero thickness to eliminate alignment errors. We chose Ta with 8-mm thickness as an attainable compromise. Because 9-MV radiation is so penetrating and because nearly every primary interaction results in secondary photons and particles that can reach the detector, an MTF derived from an edge image contains many effects not present at lower energy. This measure of 9-MV imaging performance cannot be compared to similar measurements at lower energy or even 9-MV measurements done with a different object.

Ta slug—We have an existing Ta cylinder that is 24.7 mm in diameter and 20.6 mm long. For imagers at 450-kV tube potential and below, the length of this object is sufficient for it to be effectively opaque (attenuation $>10^5$). This object is present in some images at 9 MV, but we do not consider it opaque at this energy.

Nail CT Phantom—This is a CT phantom of steel nails, and steel and Al bolts arranged for easy interpretation of CT artifacts if alignment errors exist.

D-38 CT Test Object—Its main interest to this project is the larger features and the fact that it is made of dense material.

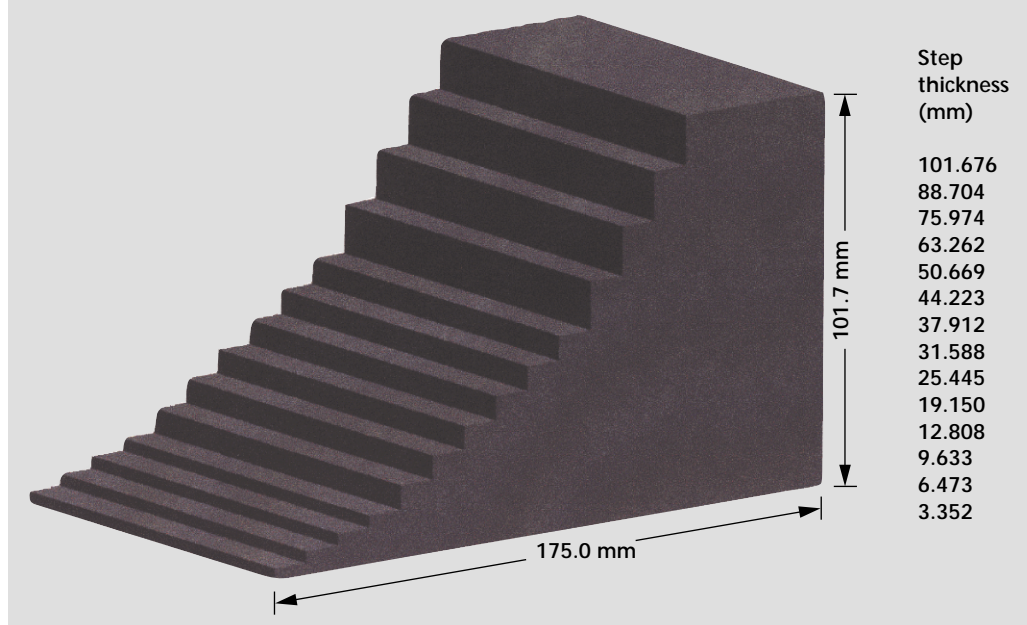
BTO—This is a high-opacity, axially-symmetric, British-made test object (BTO). Its main interest to this project is the simplicity of the geometry, high opacity (100 g/cm^2) and the fact that many labs in the US and UK are imaging this object.

W shell—This object is widely used in imaging applications.

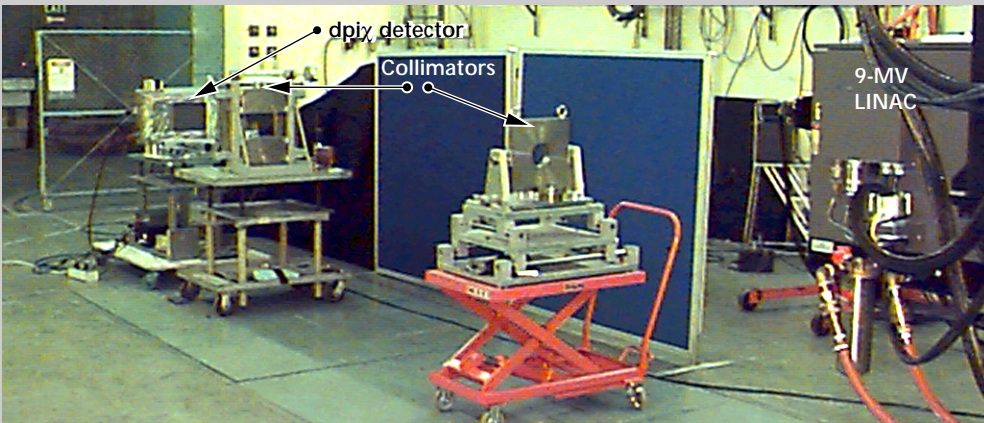
Opaque Rod—This object is important to provide a means of estimating room return and detector scatter. For this purpose, it is placed between the source and detector so as to block direct primary radiation from the detector. As with many other aspects of x-ray imaging, this can be difficult when using a 9-MV spectrum. The rod is W in the form of a right circular cylinder with ~ 150 -mm length. By making the diameter large, ~ 50 mm, we ensured that the region near the center of the rod x-ray shadow is nearly free from object scatter as well.

Experimental Results. We acquired a series of radiographic images with 6-m sdd and two different object-to-detector distances (odd), 1 and 0.5 m. Photographs of the experimental DR and CT set-up are shown in **Fig. 7**. For the Cu-step wedge, we also acquired data at 0-m (on the detector) and 0.2-m odds. The Cu-step wedge was positioned with the flat surface of the wedge towards the detector. For the Ta edge we acquired data at 0- and 1-m odds. Two data sets with the Ta edge in the vertical and horizontal directions were obtained for each distance to determine any difference in the detector response. The opaque rod, and Ta edge and slug radiographs were

Figure 6. CAD drawing of the Cu-step wedge with as-built dimensions overall and for each step. An L-bracket was also fabricated of Al to support the Cu-step wedge and to minimize x-ray scatter (not shown).



(a)



(b)

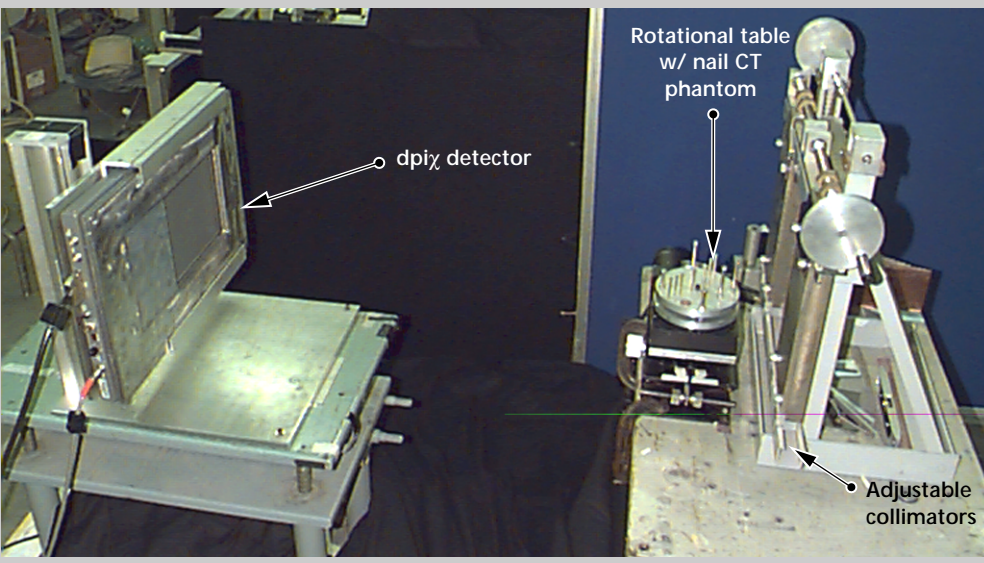
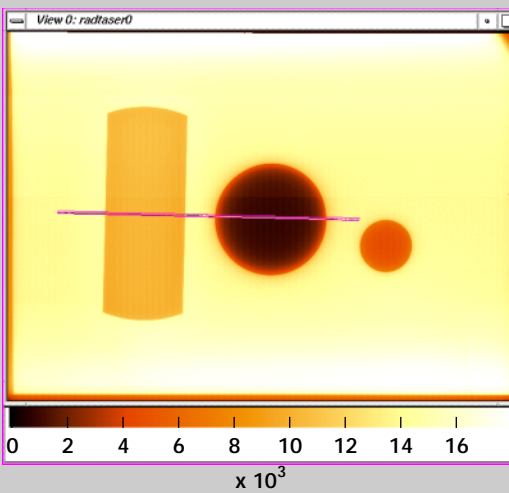


Figure 7.

(a) Photograph of the 9 MV LINAC and Min-R/dpix experimental set-up.

Overall view of the setup. (b) Close up of the detector and rotational table with nail CT phantom.

(a)



(b)

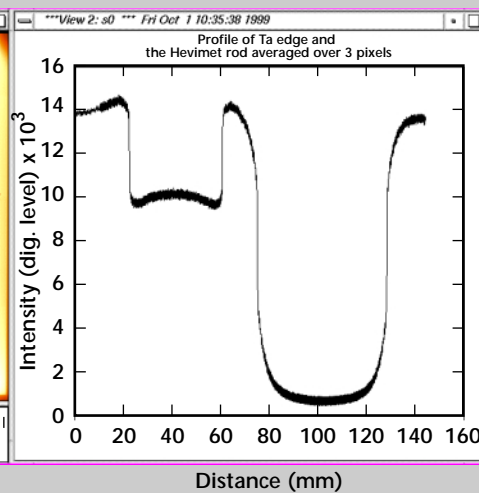


Figure 8.

(a) Representative experimental 9-MV radiograph of the Ta edge (left) and slug (right), and opaque rod (middle). These phantoms were located on the detector front surface supported by foam for an object-to-detector distance of 0 m.

(b) Profile of the Ta edge and opaque rod.

acquired at 0-m (see **Fig. 8**) and 1-m odd. We also acquired CT data of the nail CT phantom. For this data the center-axis-of-rotation of the CT system was located at a 1-m odd.

We used the opaque rod to understand scatter in the detector and to measure back shield albedo influence on the *dpi* χ imager. An important finding of this work³¹ is that the observed signal in the shadow of the opaque rod is 8% of the unattenuated signal, even with no back shield albedo contribution. This work also establishes design guidance for shield design and placement.

Simulation and Experimental Results. Models of the test object's structure have been generated for the HADES ray-tracing simulation code. To validate these models a monoenergetic (4 MV) photon source and perfect detector were used to generate most of the simulated radiographs. Simulated and experimental radiographs for the nail CT phantom are shown in **Figs. 9** and **10**, respectively. **Figure 10** also shows representative experimental results at 9 MV of a convolution back-projection reconstructed image of the nail phantom. Simulated radiographs for different assemblies of the D38 CT test object are shown in **Fig. 11**. Simulated and experimental radiographs of the BTO are shown in **Figs. 12** and **13**, respectively. Some of the simulated radiographs were reconstructed into tomograms such as the BTO as shown in **Fig. 12**. HADES, COG, and experimental radiographs for the Cu-step wedge are shown in **Fig. 14**.

The simulated radiographic and tomographic images were compared with the original mechanical drawings for each of the test objects. This validates the complete simulation process of going from mechanical drawings through simulated radiographs to reconstructed tomograms. Now that we have agreed upon the experimental source (9 MV) and detector (Min-R/*dpi* χ) for the radiographic system more realistic calculations are being performed. Other effects, such as energy distribution of the source, finite source spot size, detector response, and scattered radiation, are being treated as well.

The energy distribution of the radiation source used by HADES can be read from a user-specified input file corresponding to the radiation source of interest. Radiation distributions corresponding to any particular accelerator are obtained from full-physics Monte Carlo simulations, using machine drawings and materials specifications supplied by the manufacturers (**Fig. 15**). The source spot is assumed to be Gaussian, and its effect is included either by blurring the simulated image or, as of this year, by directly tracing multiple rays from the

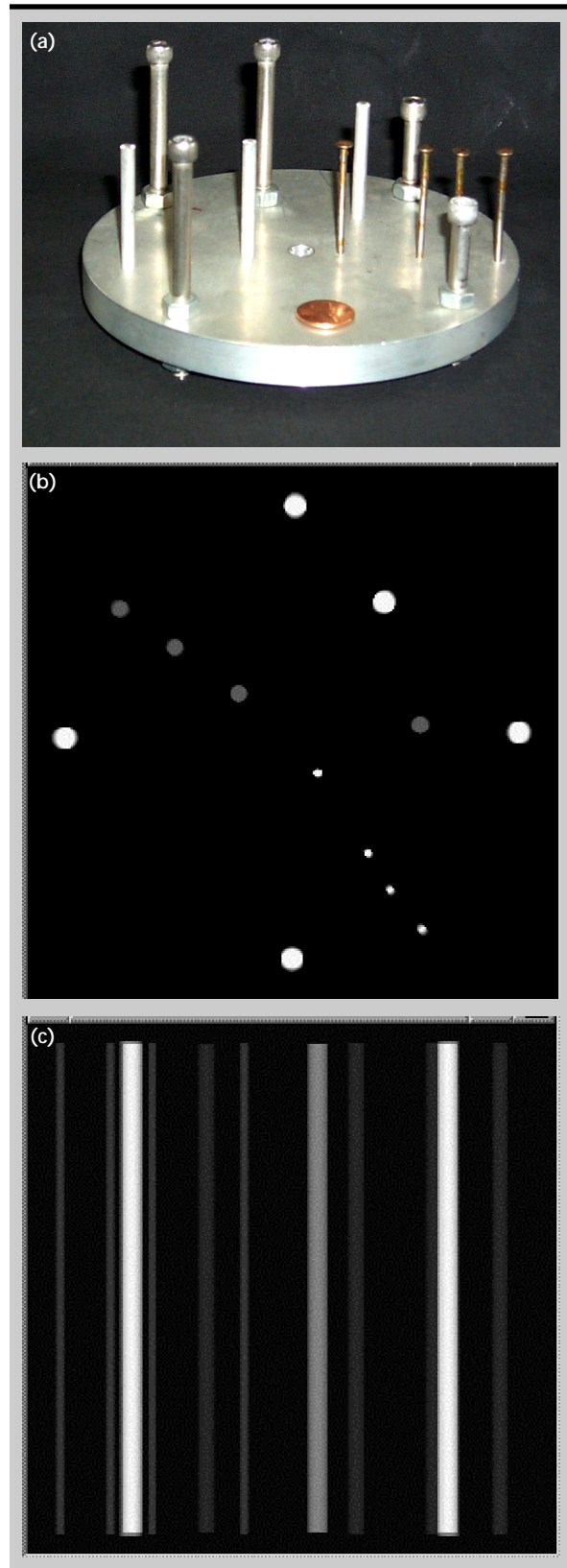


Figure 9. (a) Photograph of the nail CT phantom. Two HADES simulated monoenergetic 4-MV radiographic images [(b) top view and (c) side view] of the nail CT phantom.

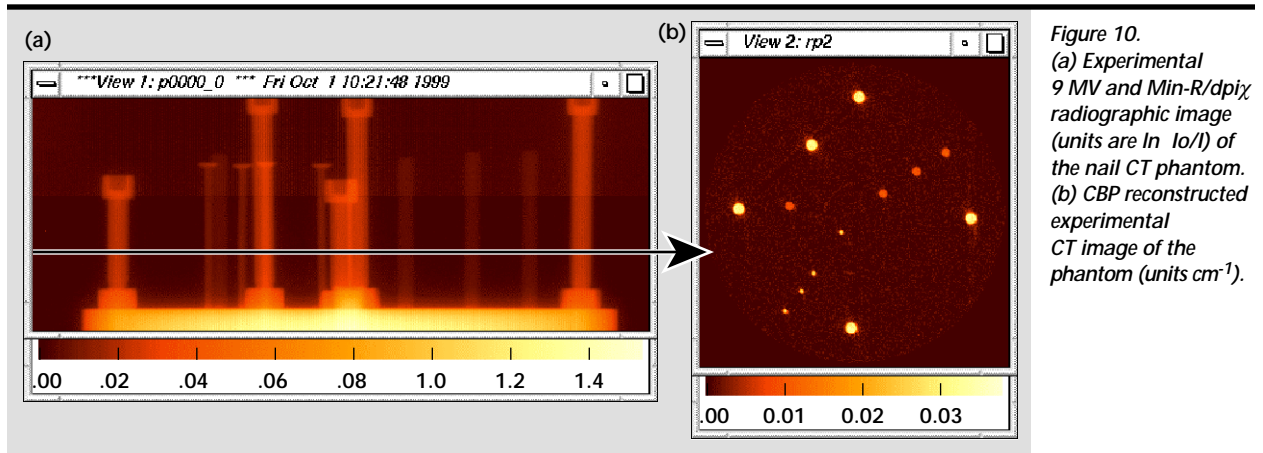


Figure 10. (a) Experimental 9 MV and Min-R/dpix radiographic image (units are $\ln I_0/I$) of the nail CT phantom. (b) CBP reconstructed experimental CT image of the phantom (units cm^{-1}).

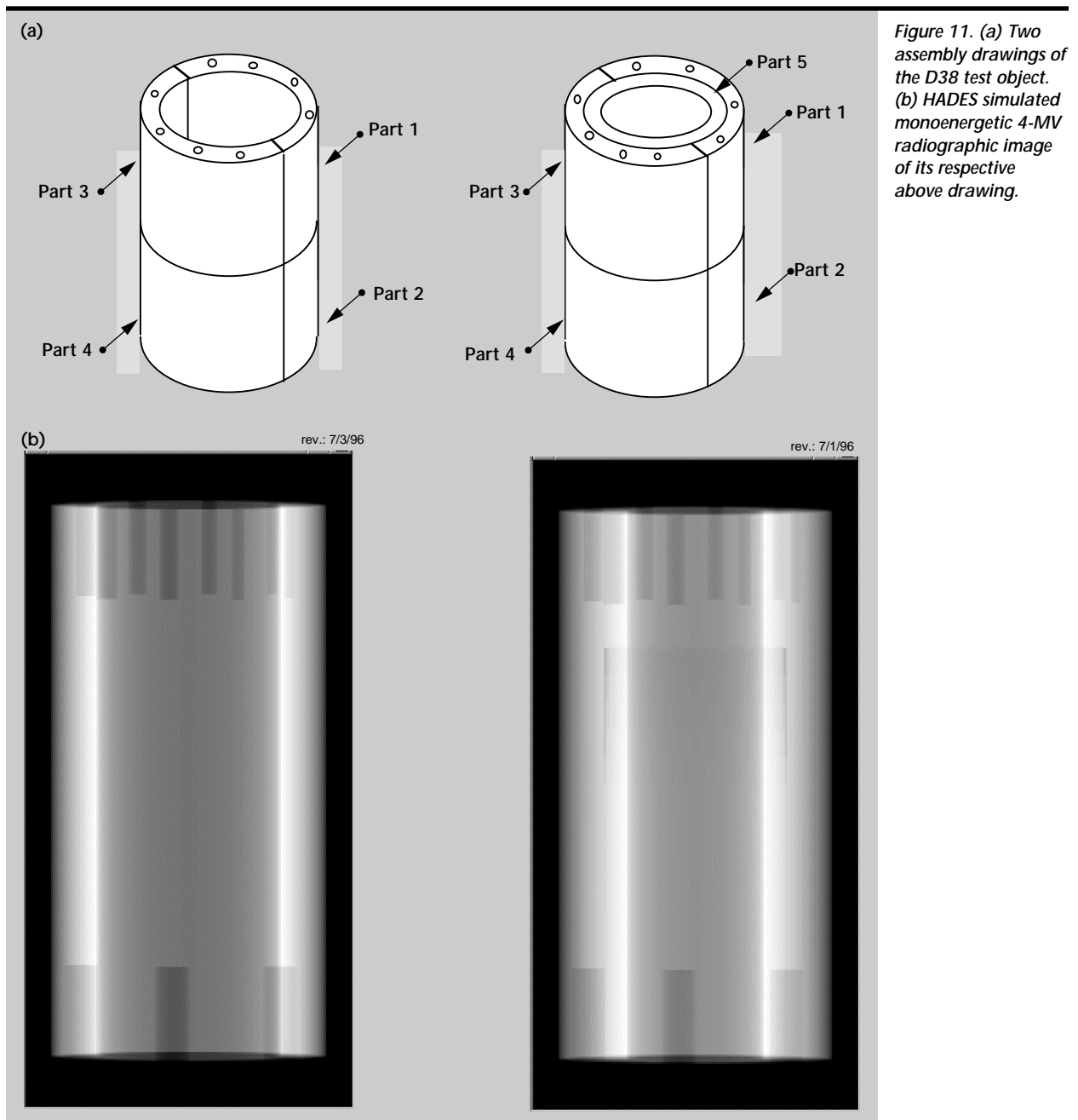


Figure 11. (a) Two assembly drawings of the D38 test object. (b) HADES simulated monoenergetic 4-MV radiographic image of its respective above drawing.

Figure 12.

(a) Photograph of the BTO. (b) HADES simulated monoenergetic 4-MV radiograph. (c) A representative reconstructed tomogram at the central vertical plane of the BTO.

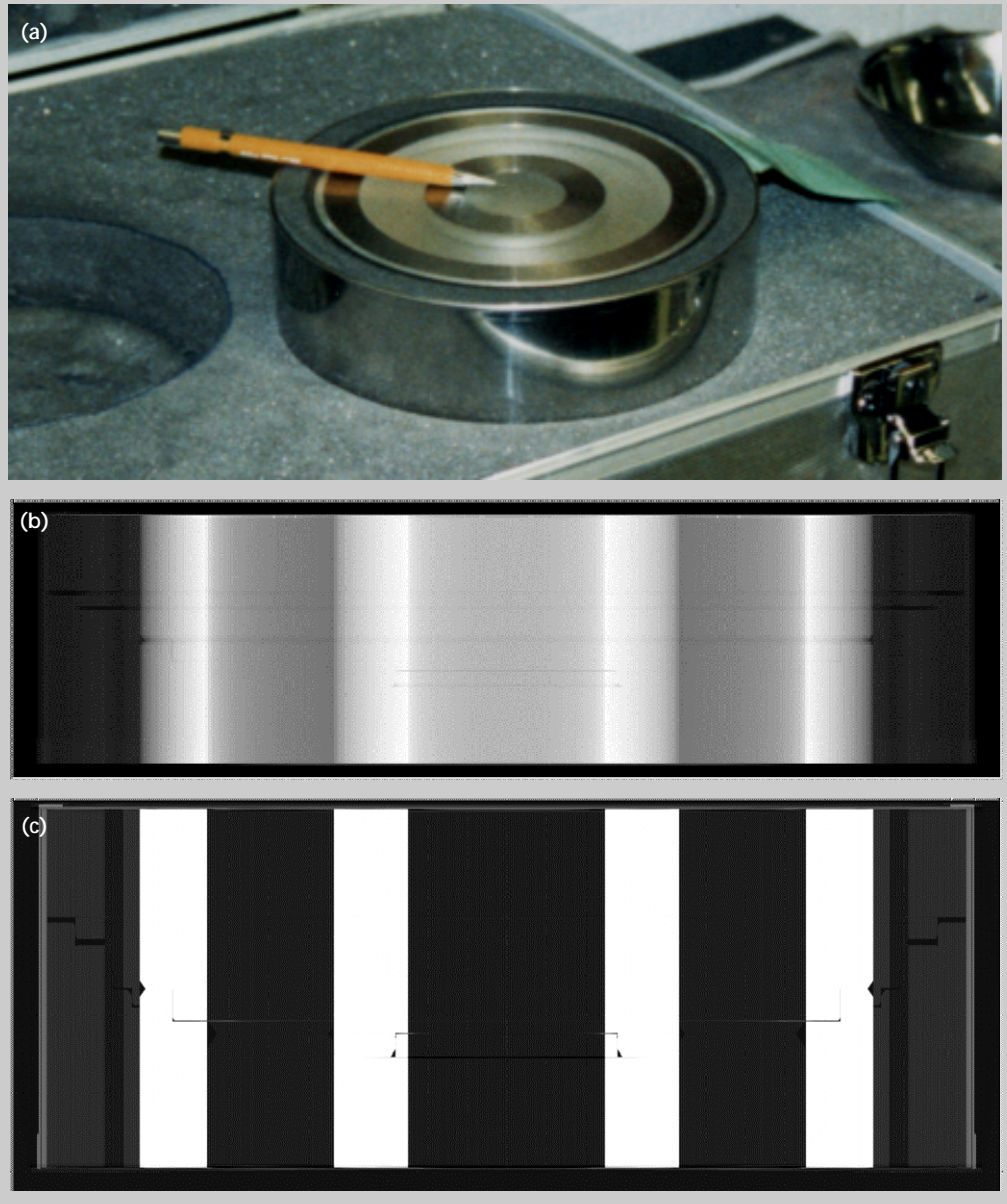
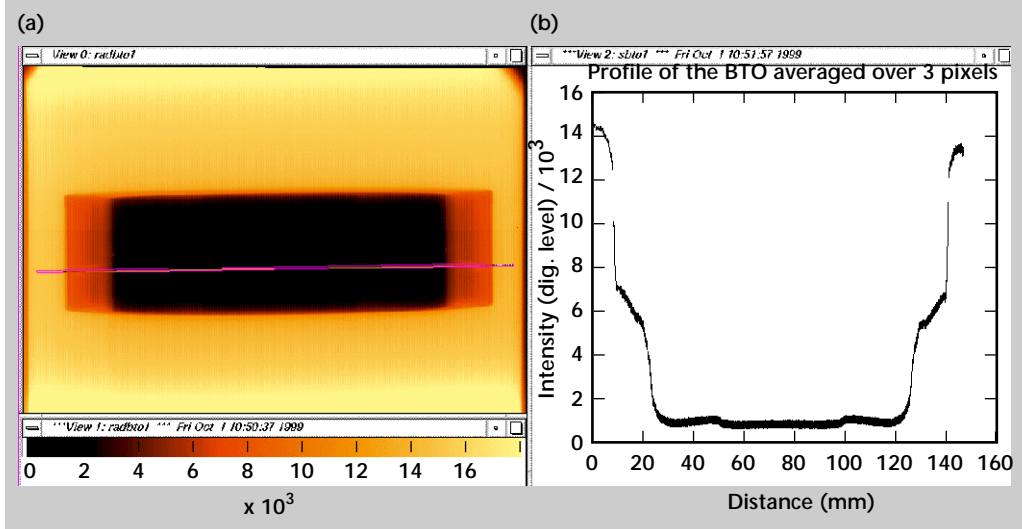


Figure 13.

(a) Representative 9 MV and Min-R/dpix experimental radiographic image (in digital detector level units) of the BTO. The grey scale was adjusted to enhance the outer portion of the BTO. (b) Profile from the line in the radiograph that reveals some of the internal details within the BTO.



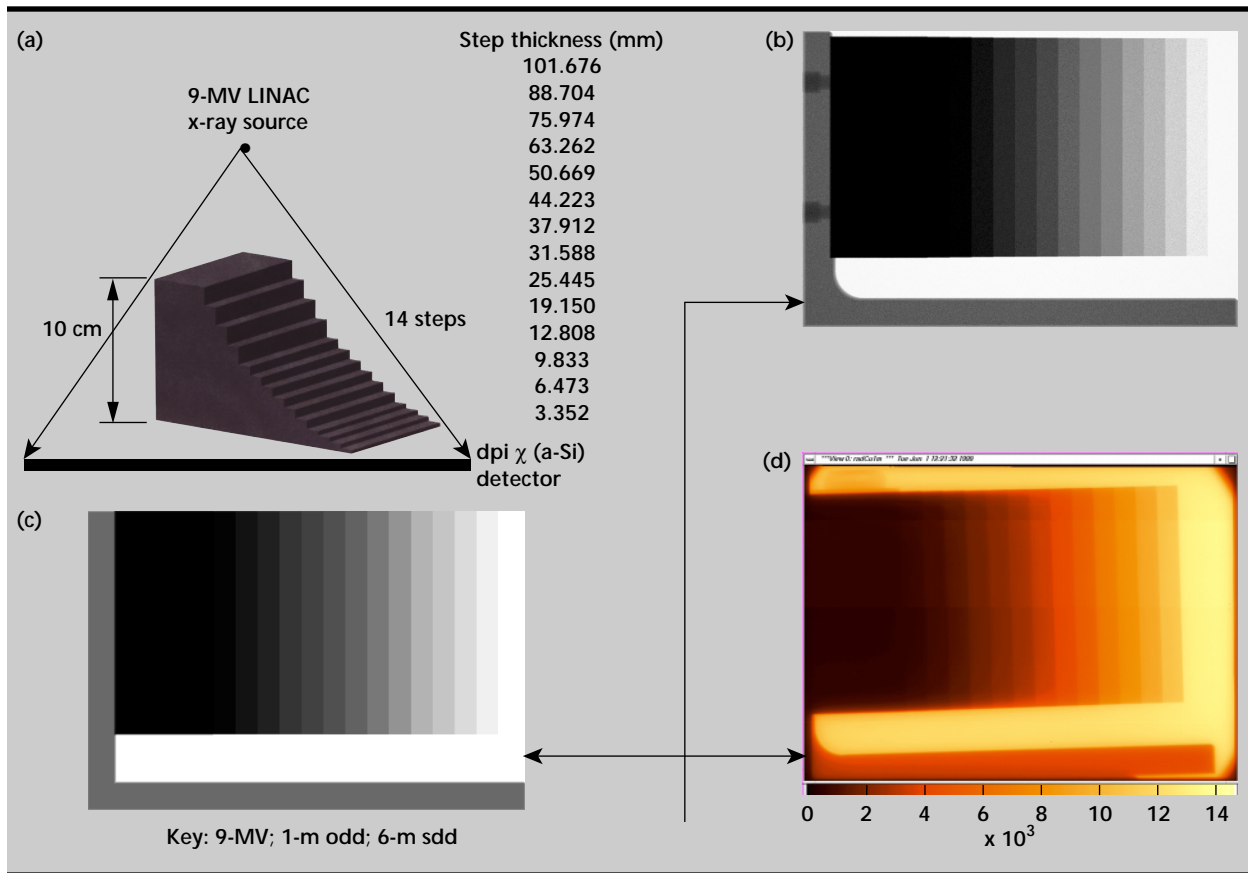


Figure 14. (a) Schematic showing the source, detector and Cu-step wedge geometry (not to scale). (b) Resultant COG Monte Carlo simulated radiographic image. (c) HADES simulated radiographic image. (d) Experimental radiographic image at 9 MV.

source distribution to the detector(s). The detector response, which previously was described as a Gaussian blur, has been enhanced to include energy-dependent blur as a user option.

A schematic of the Monte Carlo detector model is shown in **Fig. 16**. The point-spread function (PSF) of this detector model was obtained as a function of energy. These results have been added to the detector library of HADES.

In FY-99, we have been studying by simulation the scattered radiation component (or background) of several radiographically thick objects. Our experience in using full-physics Monte Carlo methods to radiographically model these objects, has led us to conclude that the scattered radiation in many cases, is slowly varying (see **Fig. 17**). We have modified HADES to read, if desired, user-specified data files describing radial variation of the scattered radiation level, as well as the average user-specified energy spectrum of the scattered radiation. The scattered radiation level does not have to be flat and the energy spectrum of the scattered radiation is not a scaled version of the input spectrum.

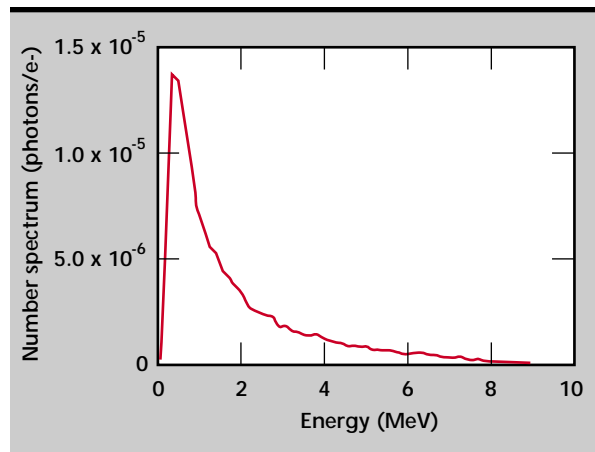


Figure 15. MCNP computed simulation of the Bremsstrahlung spectrum of the B239 VARIAN 3000 9-MV LINAC. This simulation was for the target and target holder. It did not include the mirror or other components.

Some aspects of the overall tomography problem are independent of the object being studied, for example, incident source distribution and detector response, may be pre-calculated with full-physics Monte Carlo codes and stored as user-specifiable

input files. Aspects of the overall tomography problem that depend on the object being studied (for example, the scattered radiation level), but do not depend strongly on the fine details of the object's structure, may also be included via user-specifiable files. These files may or may not be updated during the course of a reconstruction. Thus the experimental effects being added to HADES improve its overall realism and its radiographic simulation capability without compromising HADES speed.

We have used the Monte Carlo code COG to model the 9-MV electron-bremsstrahlung x-ray source and, thus far, three of the six test objects. Our initial approach has been to use a relatively simplistic (though still fairly accurate) Monte Carlo source model and a "boundary-crossing" imaging detector model (already incorporated into COG). These simulations are currently being run on the ASCI Blue-Pacific machine using between 80 and 160 CPUs per run. We are also writing a new imaging module for COG that will allow us to model the detailed response of the Min-R/*dpix* detector array (for example, electron energy deposition in the $\text{GdO}_2\text{S}_2\text{CH}$ scintillation layer). This should lead to improved agreement with experimental radiographs and Ta-edge spatial resolution measurements (see Fig. 18).

Comparisons between Experiments and Simulations. The Ta-edge radiographs were used to determine the MTF for the Min-R/*dpix* detector array. This was determined by the edge-spread function method. This method requires a profile across the edge, the differential of this edge and then the Fourier transform is taken of the differentiated edge.

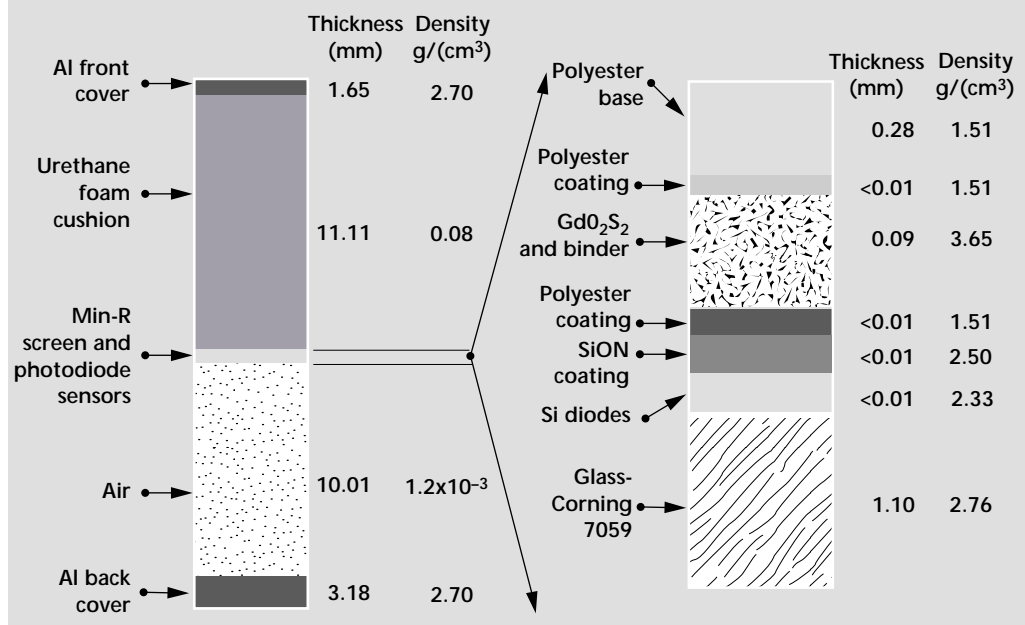
The transform results are normalized to unity and only the positive frequencies are plotted. This is a convenient experimental procedure for characterizing the spatial response of an imaging system.

To be a pure measurement of the imager, the edge should be positioned close to the imager to effectively eliminate source size contributions. It should also be opaque to radiation and not be a source of scattered radiation. It must also be thin to facilitate alignment. While convenient, this method is prone to error and uncertainty regarding the low-frequency portion of the response. This information is carried in the subtle roll-off in signal at large distance from the edge. It is difficult to measure in the presence of noise and effects from non-uniform radiation field. In addition, when this type of measurement is done using 9-MV radiation, the edge is neither opaque nor non-scattering. When deriving an MTF in this manner, it is imperative that the line-out and its derivative extend over sufficient distance to capture the low frequency effects. The results will depend on the extent of the data. If the data do not sufficiently capture the low frequency content, then all the derived MTF for higher frequencies is incorrect.

We present MTFs derived from the Ta edge in Fig. 18. Note that for our work we orient the *dpix* detector with the long dimension of the panel horizontal. Much of what is indicated by these MTFs is understandable and reassuring.

First, the MTF is reduced when the Ta edge is 1 m from the panel (odd = 1 m). We expect this because the source penumbra projected onto the panel is about 400- μm full width at half maximum

Figure 16. A schematic of the Min-R/*dpix* detector model used in our Monte Carlo calculations of the detector response function as a function of energy.



and this should cause the MTF to approach zero around 2 lp/mm.

Second, the MTF is slightly smoother but little different when we average more pixels. This is also as expected.

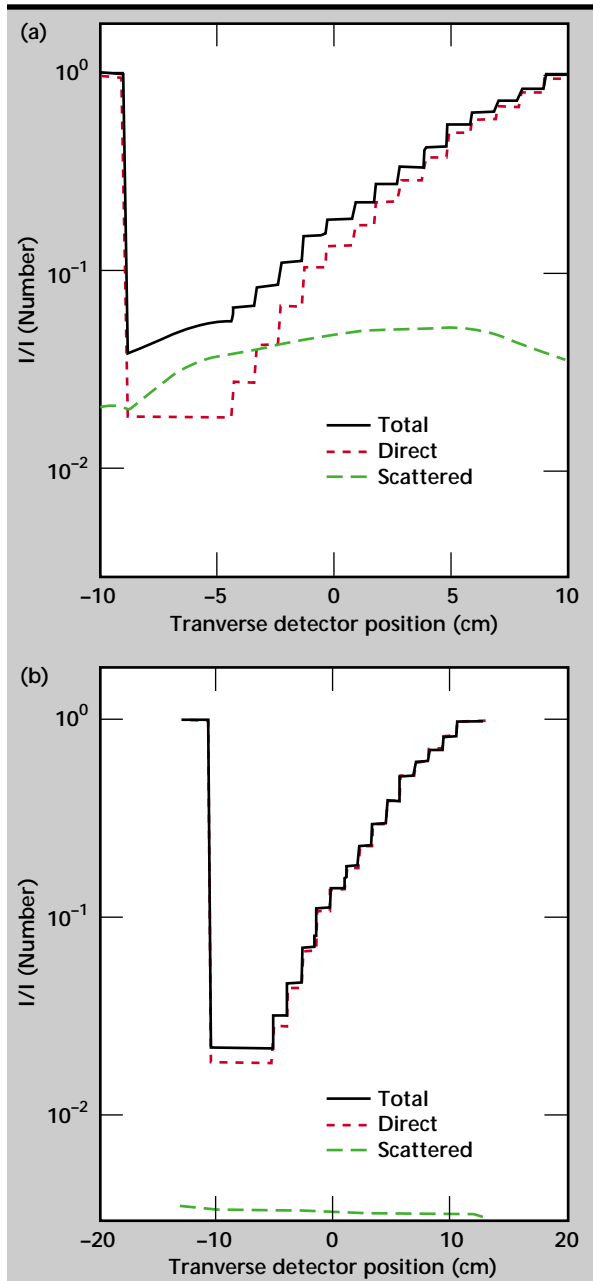


Figure 17. Line outs of a full-physics Monte Carlo simulated radiographic image of the Cu-step wedge. A 9-MV Bremsstrahlung source was used to generate the radiograph. (a) Cu-step wedge 20-cm from the detector. (b) Cu-step wedge positioned 1 m from the detector. This shows that we can estimate scatter from simulations of different experimental geometries. Note that the scattered radiation is slowly varying as compared to the object. Thus we believe that the scatter within HADES needs only to be updated periodically.

Third, no significant change is seen when comparing the intensity image (I) to the normalized image (I/I_0). This is the case, because we have attempted to

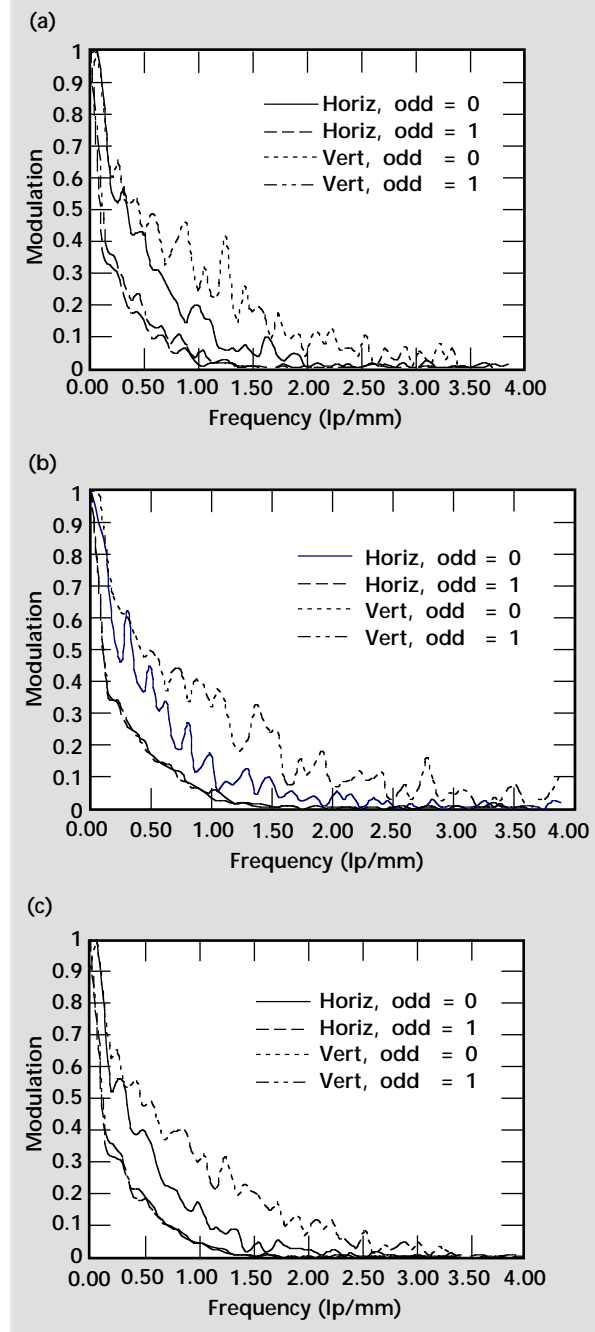


Figure 18. Experimentally determined MTF data of the Min-R/dpix detector at 9 MV determined from the Ta-edge radiographs. (a) MTF for the intensity, I , radiograph. The edge extracted was averaged over five pixels in width to reduce noise. (b) MTF for the I/I_0 radiograph. The edge was averaged over five pixels. (c) MTF for the intensity radiograph. The edge was averaged over ten pixels. The horizontal and vertical label refers to the orientation of the Ta edge. A profile was extracted normal to this edge to calculate the MTF.

linearize the detector response by calibration, and we do not expect large field-flatness effects.

However, there is one unexpected result depicted in **Fig. 18**. The MTF in the *dpix* detector is different in the two directions for odd = 0 m. This is probably not attributable to source asymmetry since it persists with the Ta edge in contact with the detector. It must be a property of our *dpix* detector when these data were acquired. We were experiencing poor detector performance in that we were getting high line-to-line noise in one direction in the detector. More work is required to understand these results.

Figures 17 through 21 show examples of our codes' abilities to predict artifacts that occur for a specific combination of photon source, experimental object, experimental configuration, and detector system. **Figure 17** shows MCNP-based estimates of the level of scattered radiation that is expected at the detector plane, as the odd is changed from 0.20 to 1.0 m. The calculations suggest that there should be a measurable decrease in the background level as the object approaches the source. This prediction

is confirmed by the experimental results shown in **Fig. 19**. The data in **Fig. 19** have not been re-scaled to be distance at the object. It is encouraging that the experimental radiographic data of the Cu-step wedge also reveal that several steps are not observed when the wedge is placed on the detector, which is consistent with the simulation results given in **Fig. 17**.

A more quantitative comparison between simulation and experimental results is shown in **Fig. 20**. Our first HADES simulation results (**Fig. 20a**) do not match the experimental results. In this case the HADES simulation did not account for all of the blur due to the detector. Note that the simulated results show a sharp step function while the experimental data are more blurred. We modeled only the detector's physical pixel size of $127 \times 127 \mu\text{m}^2$. As mentioned earlier we modeled and studied the Min - R/*dpix* detector PSF as a function of energy. Incorporation of the PSF into HADES simulations of the step wedge (**Fig. 20b**) begins to account for much of the distortion caused by the detection

Figure 19. A horizontal attenuation profile from each of the Cu-step wedge experimental radiographs obtained at several distances from the detector, as labeled. It should be noted that the magnification of the object is increasing as the object gets closer to the x-ray source. This was not corrected for in the data shown.

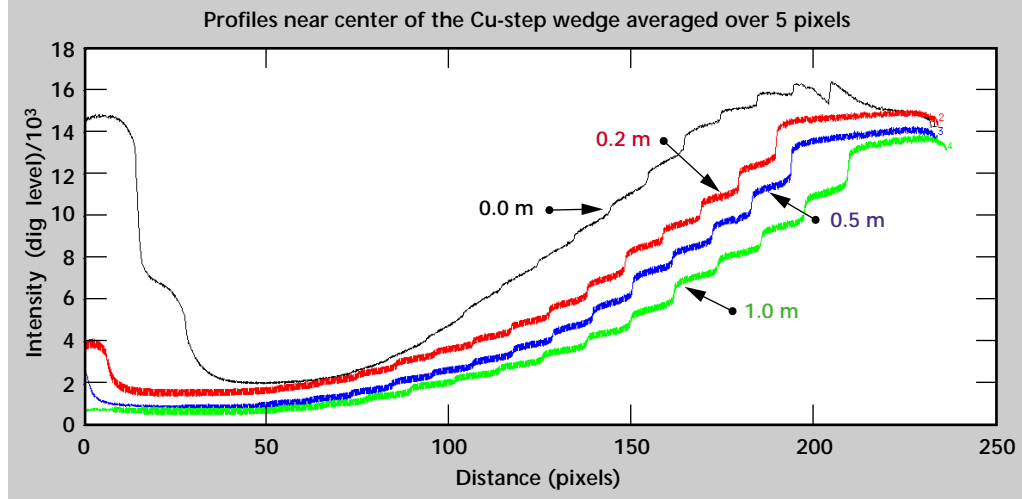
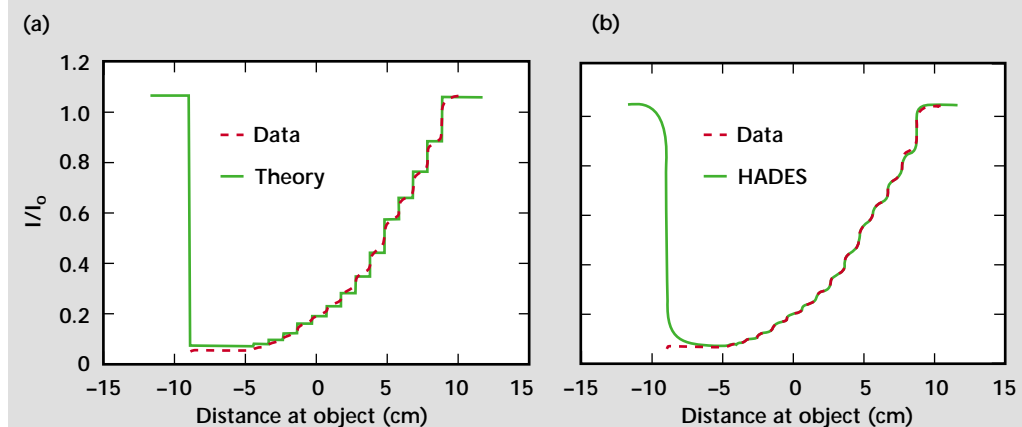


Figure 20. Comparison between HADES simulated results and experimental results for the Cu-step wedge 1 m from the detector. (a) HADES results with a 9-MV Bremsstrahlung source and a perfect detector. (b) HADES results with a 9-MV Bremsstrahlung source and a Monte Carlo determined detector response function.



system: the rounding of the steps is due to the long "tail" in the experimentally measured ESF of this detector. Note that the HADES simulated results in this case provide a much better match with the experimental data.

The ratio of the measured intensity to our HADES calculated intensity is shown in **Fig. 21**.

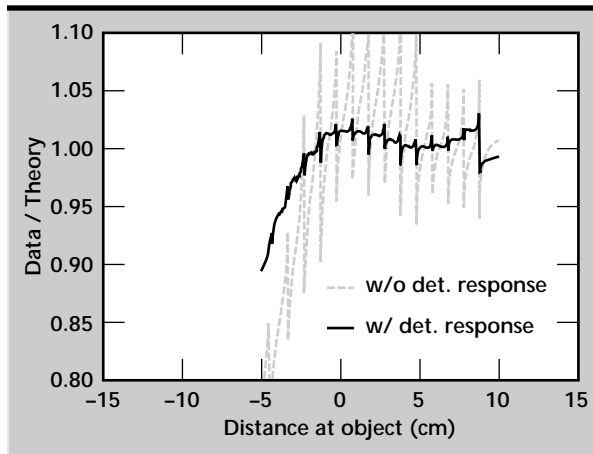


Figure 21. The ratio of the experimental data to HADES simulated data from Fig. 20 reveals that there are still some discrepancies that need to be further investigated.

There is a low-frequency error of a few percent, suggesting possibility of improving the assumed energy distribution of the photon source and/or the energy-dependent sensitivity of the detector model. There is also a high-frequency component, suggesting the need for an improved understanding of the blurring processes.

Image Reconstruction Algorithms. The reconstruction process associated with CCG can be described as follows. First an initial value for the desired image of the object is chosen. Then a forward projector model calculates the radiographs associated with this image. CCG then compares these calculated radiographs with the actual projections or radiographs and determines a better set of values for the image. The process is repeated until a satisfactory stopping point is reached. The ultimate goal of this part of the project is to create HADES-CCG, where HADES supplies the projectors and CCG performs the image reconstruction (see **Fig. 3**).

CCG has a number of stopping criteria built into the code. At this time these criteria do not seem to work with the cone-beam forward projection geometry. JCONE-CCG is being used to study how to determine when to stop the search during cone-beam

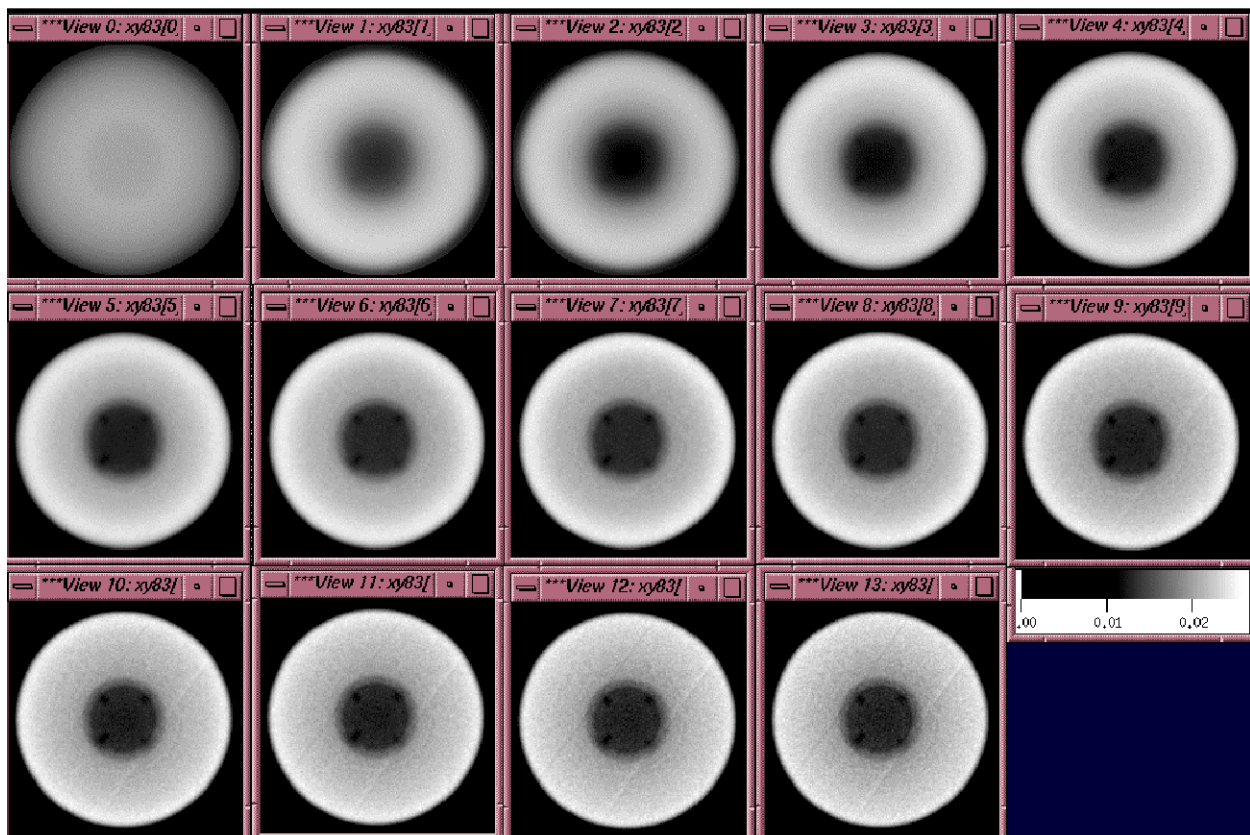


Figure 22. Successive iterations (from left to right, top to bottom) of JCONE-CCG for reconstruction of a single slice from high-energy neutron data of a test object consisting of nested cylinders of different materials (W/brass/polyethylene). The later iterations show interior details machined into the inner polyethylene cylinder.

image reconstruction. One effective stopping criterion involves plotting the norm of the residuals versus the norm of the solution.³² The residual is the difference between the calculated and measured radiographs, $\|\mathbf{B}\hat{\mathbf{o}} - \mathbf{p}\|$. This method was used to analyze experimental high-energy neutron data of a test object consisting of nested cylinders of different materials (W/brass/polyethylene). The inner cylinder (polyethylene) featured a set of slots of different depths. **Figure 22** shows the same cross-sectional slice of the object for each iteration obtained by JCONE-CCG. Note that the slots in the polyethylene are clearly visible in the later iterations.

The plot of the norm of the residual versus the norm of the solution for each iteration is shown in **Fig. 23**. The norm of the residual decreases as the solution approaches the correct value. The norm of the solution provides a measure of the change of the solution from one iteration to the next. As seen in **Fig. 23**, the curve shows an initial steep drop as the image rapidly approaches the best solution. After a point the curve begins to level off, at this time the search begins to work on noise. This can lead to undesirable results. With respect to **Fig. 22**, it can be seen that before iteration 5 (View 4) some of the object features do not appear as clearly as after iteration 5. After iteration 8 it appears that the object becomes noisier and eventually two parallel lines appear across the object beginning around iteration 9 (View 8).

These lines are not a real effect within this data as we have observed that these two lines also show up in the iterations of other data sets. Analysis of **Fig. 23** reveals that the norm of the residuals begins to level off around iteration 5 and there are only small changes after iteration 8. We are studying how to use this and other methods to determine the optimum number of iterations to produce the best results automatically.

RECON/CCG and HADES are both large complicated codes, created and maintained by separate organizations. Since the interactions between the two codes is limited and clearly defined, it has been decided to run the codes separately and exchange information between them using shared memory.

This year we concentrated on three issues: reducing artifacts, mitigating the effects of beam hardening, and blur removal. We present an example of artifact removal. Streak and ring artifacts are very common in tomographic reconstructions. Streak artifacts result when a detector has been corrupted in a single projection: the usual cause is a hit by extraneous radiation. Ring artifacts result when a detector has been uniformly corrupted over all

projections: typical causes are gain misadjustments and electronics problems in which the detector is either “cold” (zero) or “hot” (saturated).

We present a simulated example. The true unknown is shown in **Fig. 24a**, and the corrupted projection data in the form of a sinogram is given in **Fig. 24b**. A sinogram is a 2-D image created by displaying all the detector outputs at one projection angle along a horizontal line and stacking these lines according to projection angle. Radiation hits were simulated by Gaussian mixture noise with probability 0.99 that the noise at a detector is Gaussian with standard deviation σ , and with probability 0.01 that it is Gaussian with standard deviation 100σ . Consequently, there is a hit 1% of the time. These outliers are obvious as speckles in **Fig. 24b**. The projection data were further corrupted by setting one detector output to zero for all projections, the result is the vertical line in the sinogram. The maximum likelihood estimation method with the usual assumption that the noise on the observed data is Gaussian with constant variance leads to the usual least-squares fit between observed data and modeled data generated from the current estimate of the unknown image. Least-squares is the method commonly used in iterative tomography algorithms.

Unfortunately, the squared error function is highly sensitive to outliers. This is demonstrated in the image reconstructed using least squares shown in **Fig. 24c**. Radiation hits caused the streak artifacts in **Fig. 24c**, and the cold detector produced the ring artifact. We used robust statistical methods to mitigate the effects of the outliers.

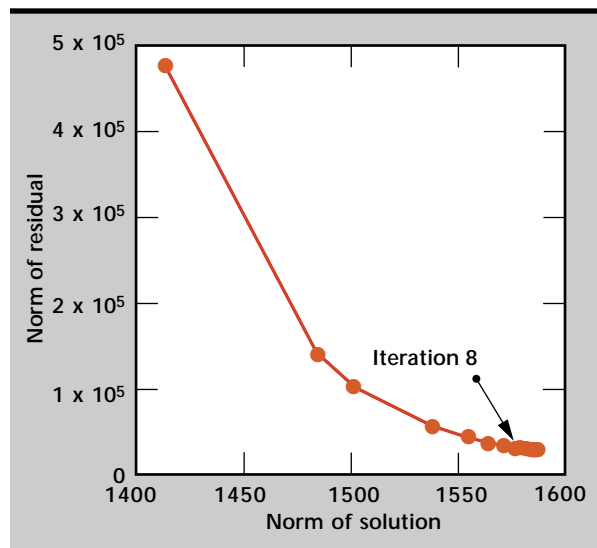


Figure 23. Plot of the norm of the residual versus the norm of the solution as a function of iteration for the neutron data shown in Fig. 22. This curve is used to determine the iteration that contains the best recovery of the object with the least noise.

First, as described by **Eq. 7**, we modified the squared error function so that it transitioned from a squared penalty for small mismatches between observed data and modeled data to a linear penalty for large mismatches, thereby making the fitting function much less sensitive to outliers. The result is shown in **Fig. 24d**: the streak artifacts have disappeared, but an attenuated ring artifact remains. To improve the reconstruction further, we added another transition from the linear penalty for large mismatches to a saturated penalty for very large mismatches. This error function is shown in **Eq. 8**. The result of using **Eq. 8** is shown in **Fig. 24e** where the ring artifact has almost completely disappeared. To our knowledge this has been the first application of robust statistical techniques to tomography. This was made possible by the effectiveness of CCG in minimizing the modified cost functions. The results for our simulated example were dramatic.

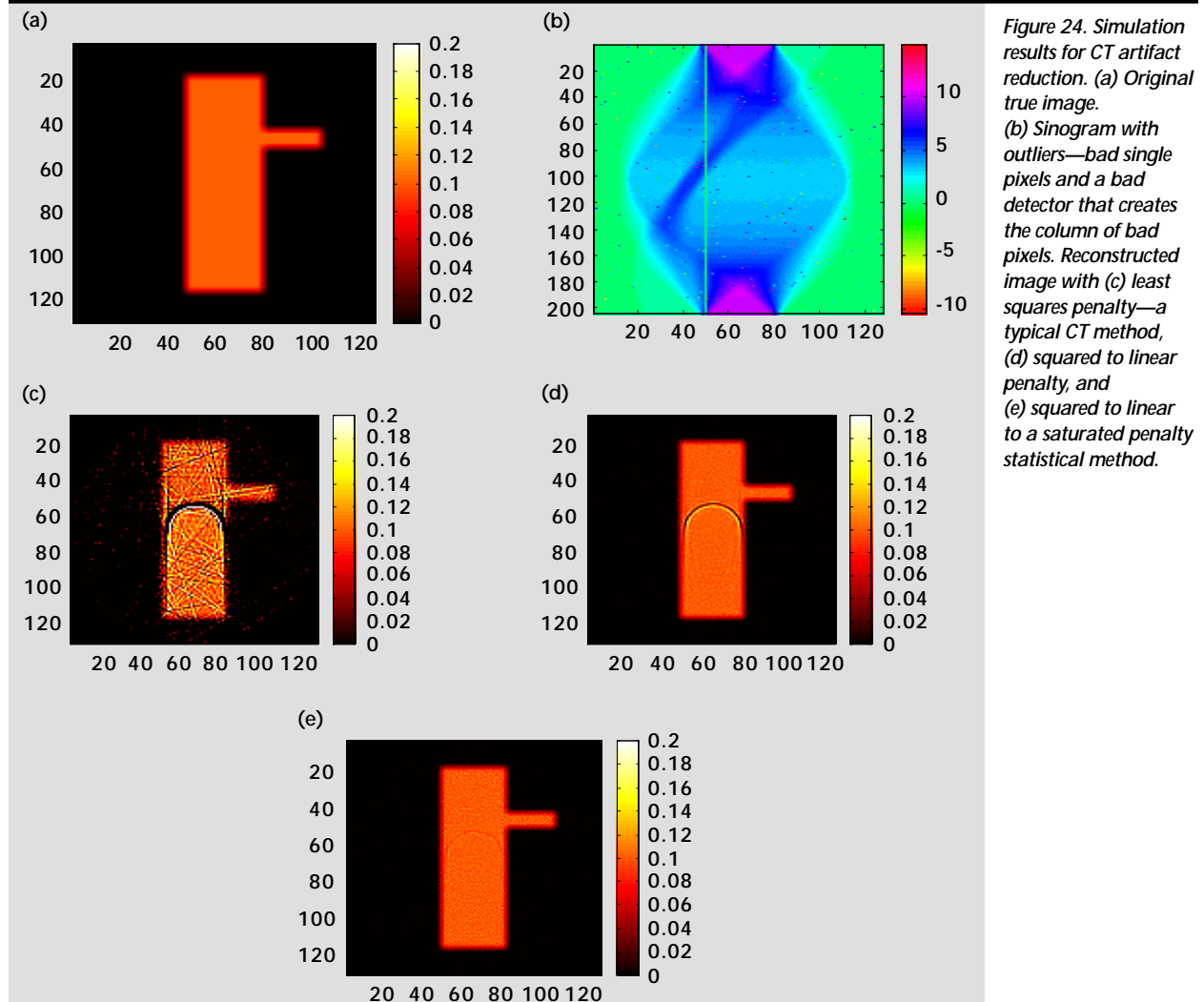
There are many real problems at LLNL and elsewhere that are replete with streak and ring artifacts.

Our initial investigation into using this method to reduce these artifacts was only partially successful. Work continues in this area.

Other work on artifacts due to outliers, beam hardening, scatter and blurring will continue for the rest of the year and through FY-00. We are currently extending our robust algorithms to Poisson data problems that occur in photon-starved x-ray tomography, neutron and proton tomography, and emission tomography.

In addition, we have developed algorithms that model selective attenuation at different spectral energies. These algorithms model beam hardening directly in the reconstruction process, rather than using a polynomial correction for this in the sinogram before image reconstruction. These algorithms apply to both the single material and the multiple material problems.

Finally, we have developed an efficient deconvolution algorithm to deal with the blurring problem, and we are in the process of incorporating it into our tomography algorithms.



Summary

Preliminary scattering models have been incorporated into HADES and this code has been transferred to LLNL programs. HADES is being used to simulate a Mg tensile bar specimen.

We are using an a-Si array with a Min-R scintillator at 9 MV for radiographic and tomographic imaging. The spatial response for this system has been measured. Monte Carlo simulations were used to determine the energy spectrum for the source and detector spatial response as a function of energy.

We have acquired experimental radiographs and HADES simulations for all test objects, and detailed COG simulations for some of them. We have begun validation of the radiation models by comparison with experimental radiographs.

Incorporation of both the source spectral information and detector PSF were required to improve HADES simulated radiographs to within 5% of the measured radiographs. These results are encouraging however, we need better agreement than this to get tomographic image reconstructions with 1% accuracy.

We have determined a method to merge the CCG and HADES codes into a new image reconstruction code.

Future Work

We will demonstrate accurate and fast radiographic simulation tools by further investigation and refinement of our Monte Carlo and HADES models to improve the agreement with the measured radiographic results. We will complete the designs and fabrication of phantoms such as an opaque test object. Experimental radiographs of the test objects will be acquired as well as more emphasis placed on CT projection data. The merging of CCG and HADES will be completed and several performance tests with simulated and experimental CT data will be studied.

We need to demonstrate that our methods to reduce CT artifacts in simulated data work as well with experimental data. New methods will be developed to reconstruct images of objects with high-Z/high-density (opaque) components, which compromise traditional CT algorithms.


Acknowledgments

The authors would like to thank D. Rikard, E. Updike, K. Morales, A. Guerrero and D. Schneberk for acquiring and processing the DR data; R. Perry

for helping process the Ta-edge DRs to generate edge response and MTFs; A. Waters for providing the Mg radiographic and tomographic data; and D. Schneberk for processing and reconstructing the nail phantom data.

References

1. A. C. Kak and M. Slaney (1987), "Principles of computerized tomographic imaging," IEEE Press, New York, New York.
2. C. J. Leliveld, J. G. Maas, V. R. Bom, and C. W. E. van Eijk (1994), "The effects of detected scattered radiation and beam hardening in x-ray computerized tomographic imaging of industrial objects," *Proc. of the Int. Symp. on Computerized Tomography for Industrial Applications*, Berlin, Germany, June 8–10.
3. D. J. Schneberk, S. G. Azevedo, H. E. Martz, and M. F. Skeate (1990), "Sources of error in industrial tomographic reconstructions," *Mat. Eval.*, Vol. **48**, No. 609.
4. F. Dietrich and J. Hall (1996), "Detector concept for neutron tomography in the 10–15 MeV energy range," Lawrence Livermore National Laboratory, Livermore, California (UCRL-ID-123490).
5. F. Dietrich, J. Hall, and C. Logan (1997), "Conceptual design for a neutron imaging system for thick target analysis operating in the 10–15 MeV energy range," J. Duggan and I. Morgan (eds.), *Application of Accelerators in Research and Industry* (AIP CP392), AIP Press, New York, New York, pp. 837–840.
6. J. Hall, F. Dietrich, C. Logan, and G. Schmid (1999), "Development of high-energy neutron imaging for use in NDE applications," to be published in *Proc. of SPIE Conference*, Denver, Colorado, July.
7. G. Kowalski (1978), "Suppression of ring artifacts in CT fan-beam scanners," *IEEE Trans. Nucl. Sci.*, Vol. **NS25**, No. 5, pp. 1111–1116.
8. M. B. Aufderheide, D. Slone, and A. Schach von Wittenau (1999), "HADES: A code for radiographic simulation," Lawrence Livermore National Laboratory, Livermore, California (UCRL-CODE-99035).
9. T. Wilcox and E. Lent (1993), "COG - a particle transport code designed to solve the Boltzman equation for deep-penetration (shielding) problems," Vol. **1** Users Manual, Lawrence Livermore National Laboratory, Livermore, California (M-221-1); see also R. Buck and E. Lent (1993), "COG: a new, high-resolution code for modeling radiation transport," LLNL Energy and Technology Review (June); additional information on COG may be obtained via the Web at URL http://www-phys.llnl.gov/N_Div/COG/.
10. J.F. Briesmeister (1997), "MCNP—a general Monte Carlo N-particle transport code," Technical Report LA-12625-M, Los Alamos National Laboratory, Los Alamos, New Mexico.

11. G. P. Roberson, D. J. Schneberk, J. J. Haskins, C. M. Logan, H. E. Martz, D. E. Perkins, and D. R. Rikard (1998), "Improving computed tomography design and operation using simulation tools," Lawrence Livermore National Laboratory, Livermore, California, *Engineering Research, Development and Technology* (UCRL-53868-97), January.
12. D. L. Weirup, H. E. Martz, and D. J. Schneberk (1993), "New production reactor target particle characterization by computer simulation of computed tomography systems," Lawrence Livermore National Laboratory, Livermore, California (UCRL-UR-114836), August.
13. J. Hall (1996), "Monte Carlo modeling of neutron and gamma-ray imaging systems," *Neutrons in Research and Industry*, SPIE, Vol. **2867**, No. 465, Lawrence Livermore National Laboratory, Livermore, California (UCRL-JC-122830).
14. R. Buck and J. Hall (1999), "Applications of the COG multiparticle Monte Carlo transport code to simulated imaging of complex objects," to be published in *Proc. of SPIE Conference*, Denver, Colorado, July.
15. D. M. Goodman, E. M. Johansson, and T. W. Lawrence (1993), "On applying the conjugate gradient algorithm to image processing problems," Ch. 11 in *Multivariate Analysis: Future Directions*, C. R. Rao, ed., Elsevier Science Publishers.
16. H. W. VanTrees (1968), "Detection estimation and modulation theory," John C. Wiley and Sons, New York, New York.
17. H. Stark (1987), "Image recovery: theory and application," Orlando Academic Press.
18. L. Kaufman (1993), "Maximum likelihood, least squares and penalized least squares for PET," *IEEE Trans. Med. Imaging*, Vol. **12**, No. 2.
19. D. M. Goodman, T. W. Lawrence, E. M. Johansson, and J. P. Fitch (1993), "Bispectral speckle interferometry to reconstruct extended objects from turbulence-degraded telescope images," Ch. 13 in *Handbook of Statistics, Vol. 10: Signal Processing and its Applications*, N. K. Bose and C. R. Rao, eds., North Holland.
20. R. H. Byrd, J. Nocedal, and R. B. Schnabel (1994), "Representations of quasi-Newton matrices and their use in limited memory methods," *Math. Prog.*, Vol. **63**, No. 2, January.
21. D. M. Goodman (1997), "Maximum likelihood estimation with Poisson (counting) statistics for waste drum inspection," Lawrence Livermore National Laboratory, Livermore, California (UCRL-ID-127361), May.
22. P. J. Huber (1981), "Robust Statistics," John C. Wiley and Sons, New York, New York.
23. P. McCullagh and J. A. Nelder (1989), "Generalized Linear Models," 2nd Ed., Chapman and Hall, London.
24. F. Natterer (1986), "The Mathematics of Computerized Tomography," John C. Wiley and Sons, New York, New York.
25. H. E. Martz, G. P. Roberson, D. C. Camp, D. J. Decman, and J. A. Jackson (1998), "Active and passive computed tomography mixed waste focus area final report," Lawrence Livermore National Laboratory, Livermore, California (UCRL-ID-131695), November.
26. R. T. Bernardi (1997), "Field test results for radioactive waste drum characterization with waste inspection tomography (WIT)," presented at the *5th Nondestructive Assay and Nondestructive Examination Waste Characterization Conference*, Salt Lake City, Utah, January 14–16, INEL CONF-970126, pp. 107–115.
27. R. T. Bernardi and H. E. Martz, Jr. (1995), "Nuclear waste drum characterization with 2 MeV x-ray and gamma-ray tomography," *Proc. of the SPIE's 1995 International Symposium on Optical Science, Engineering, and Instrumentation*, Vol. **2519**, San Diego, California, July 13–14.
28. A. M. Waters, H. Martz, K. Dolan, M. Horstemeyer, D. Rikard, and R. Green (1999), "Characterization of damage evolution in an AM60 magnesium alloy by computed tomography," R. E. Green, Jr., ed., *Proc. of Nondestructive Characterization of Materials™*, Sydney, Australia, June 28–July 2; pp. 616–621.
29. R. L. Weisfield, M. A. Hartney, R. A. Street, and R. B. Apte (1998), "New amorphous-silicon image sensor for x-ray diagnostic medical imaging applications," *SPIE Medical Imaging, Physics of Medical Imaging*, Vol. **3336**, pp. 444–452.
30. K. Dolan, C. Logan, J. Haskins, D. Rikard, and D. Schneberk (1999), "Evaluation of an amorphous silicon array for industrial x-ray imaging," *Engineering Research Development and Technology* (UCRL-53868-99), Lawrence Livermore National Laboratory, Livermore, California, January.
31. C. M. Logan and A. E. Schach von Wittenau (1999), "Effects of back shield albedo on imagery with a dpiX Flashscan 20 using a 9-MV Bremsstrahlung spectrum: measurements and Monte Carlo simulations," submitted to *Materials Evaluation*, Lawrence Livermore National Laboratory, Livermore, California (UCRL-JC-136055).
32. C. L. Lawson and R. J. Hanson (1974), "Solving Least Squares Problems," Prentice-Hall, Inc., Englewood Cliffs, New Jersey. 



Ultra-Wideband Phased Array

Rexford M. Morey
Laser Engineering Division
Electronics Engineering

We have explored the unique characteristics of ultra-wideband phased arrays. We performed proof-of-principle experiments and calculated radiation patterns as a function of number of elements and element spacing for a linear and a planar array.

Introduction

The Micropower Impulse Radar (MIR) program at Lawrence Livermore National Laboratory (LLNL) has led to many successful demonstrations of ultra-wideband (UWB) radar, such as concrete bridge deck inspection (HERMES) and plastic mine detection (LandMark). These applications use a single transmit/receive unit or an array of transmit/receive units, which essentially operate independently of each other and not in a phased array configuration. With the low power available from MIR transmitters, signal-to-noise ratios limit the useful radar range of single-channel MIR implementations. Target detectability is a function of power on the target. To increase power on the target, an array of MIR transmitter/antenna units can be time-triggered to transmit as a time-domain UWB phased array.

UWB phased arrays have several unique characteristics that are not achievable with narrow-band phased arrays. We have explored several of these unique characteristics. In contrast to narrow-band phased arrays, UWB phased array elements can be sparse and randomly spaced. Also beam-width and side lobe level can be independently controlled. Therefore, there are several significant reasons to investigate UWB time-domain phased arrays, including extended radar range, deeper penetration into solid materials, side lobe level versus radiated beam-width, and beam steering.

Important applications of UWB phased arrays include characterizing deep underground structures, monitoring fluids and fluid flow in the earth for environmental restoration, detailed imaging of distress in concrete infrastructures, and vehicle control in subway systems (such as the San Francisco transit system, BART) and the Automated Highway System (for example, intelligent cruise control).

This report presents the initial steps of a new program to develop a core technology in high-power arrays for 3-D image formation and visualization in dense media such as the subsurface of the earth. The program is built on the extensive body of work at LLNL in geophysics,¹⁻⁴ MIR technology,⁵ ground-penetrating radar (GPR) imaging,⁶⁻⁸ and laboratory measurements of electromagnetic (EM) properties of materials.⁹

To determine the utility of high-power UWB arrays, proof-of-principle experiments and array modeling were performed. These experiments required assembling a time-domain phased array using MIR technology. The proof-of-principle experiments included assembling and testing a two-element, a four-element, and an eight-element transmitting array. The model studies included calculating the radiation patterns of arrays of UWB transmitters as a function of number of elements and element spacing for a linear array and a planar array. Also radiation patterns were calculated when beam steering is invoked.

Applications of high-power arrays include characterizing underground facilities (UGFs), battle-damage assessment of targeted UGFs, detection and mapping of unexploded ordnance (UXO), and geophysical surveys, such as earthquake assessment and monitoring fluid flow. The deployment of a sparse multi-element UWB array, which includes multiple time-synchronized transmitters, has not been done before.

Past UWB and GPR research has included development of single-channel radar systems and data processing methods for locating hazardous waste, profiling lake bottoms, determining characteristics of geological interfaces, and evaluating civil structures and materials such as concrete.¹⁰⁻¹³ The multi-element UWB system signal-to-noise (SNR) will

increase over a single-channel UWB system by using an array of time-synchronized UWB transmitters to put more energy on a subsurface volume element (voxel).

Progress

Recent advances in diffraction tomography,¹⁴ in seismic exploration,¹⁵ and in acoustical diagnostic imaging¹⁶ have come from using multiple transmitting and/or receiving elements which look at the same voxel from a variety of angles. In the future we propose using multiple transmitters and multiple receivers in large time-domain phased arrays. Simultaneous triggering of the multiple transmitters increases radar range by putting more power on the target, while the multiple receivers collect more of the reflected energy.

Modeling

A typical UWB signal can be characterized as single cycle of a sine wave called a monocycle. A Mathcad program was developed to calculate the radiation pattern from various array configurations transmitting UWB monocycle signals.

Figure 1 is an example of the time-space radiation pattern for a nine-element linear array. If the monocycle pulse-width is 1 ns, then the element spacing is about 1 ft and the array length is 8 ft. The radiation pattern is created from the superposition

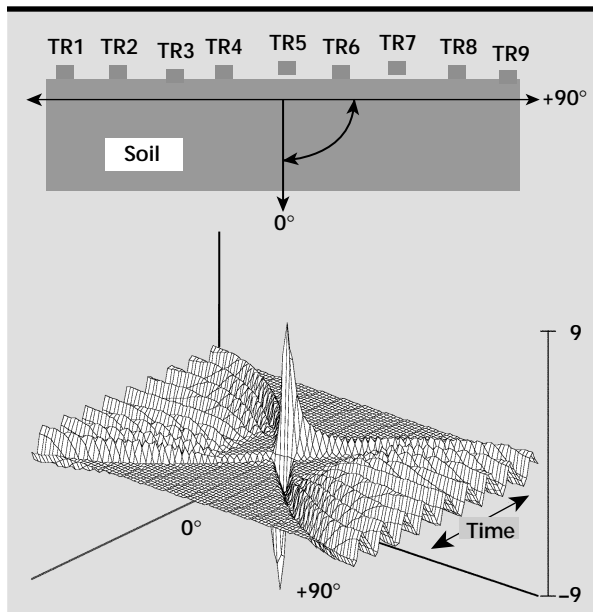


Figure 1. Time-space radiation pattern of a linear array of nine elements with element spacing equal to one pulse width.

of the nine transmitter pulses synchronized to arrive on boresight (0°) at the same time. If the observer is at $+90^\circ$, then the signal from the nearest transmitter arrives first, followed by a sequence of pulses from each of the other transmitters, forming the “side lobes” of the array radiation pattern.

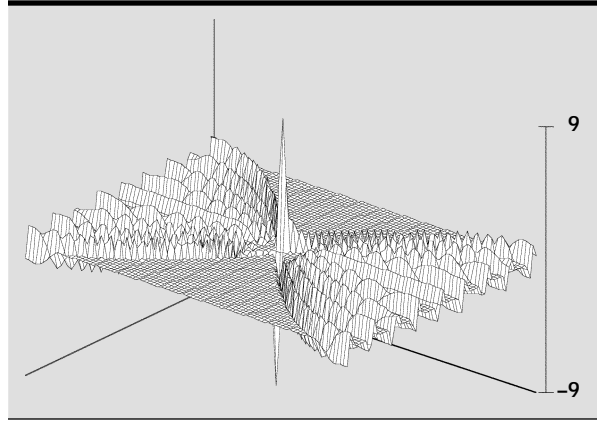


Figure 2. Time-space radiation pattern of a nine-element linear UWB array with element spacing equal to two pulse widths.

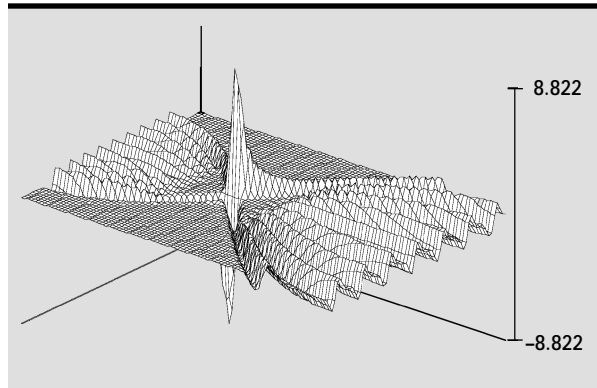


Figure 3. Time-space radiation pattern with the main beam steered off boresight by 20° .

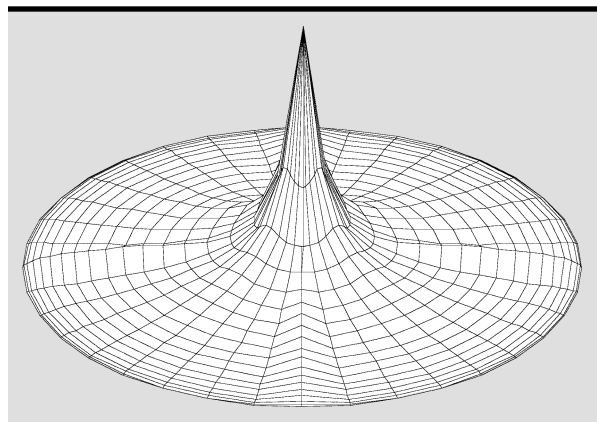


Figure 4. Time-space radiation pattern for a 9×9 -element planar array with a one-pulse-width element spacing.

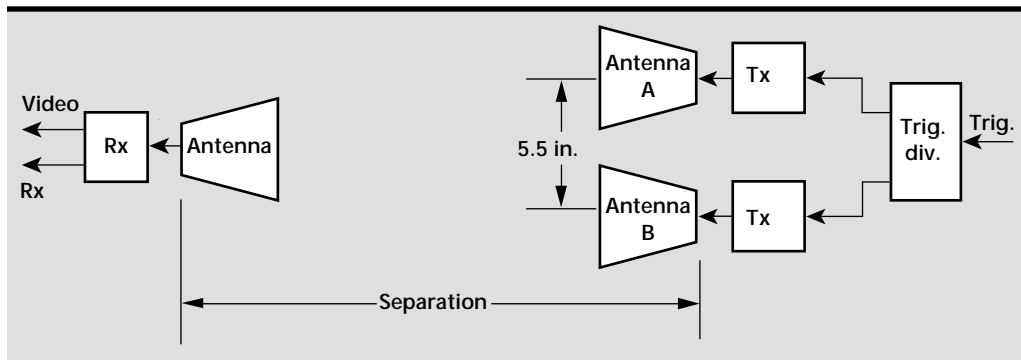


Figure 5. Diagram of two-transmitter measurement setup.

Figure 2 represents the calculated radiation pattern when the element spacing is two pulse-widths, doubling the array length and thus narrowing the 3-dB width of the main beam. The side-lobe level is the same as in **Fig. 1**, thus we have independent control of main-beam characteristics and side-lobe level, a property of UWB arrays that is not available with conventional narrow-band arrays.

An example of beam steering is shown in **Fig. 3** for the same nine-element linear array. The width of the main beam increases as the beam is steered off boresight by 20° .

Modeling was also done for planar arrays as shown in **Fig. 4**.

Patterns for a planar array are calculated using a unicycle pulse (half of a monocyte) for simplicity of display. The plots are in spherical coordinates (ρ , θ , and ϕ) showing the envelope of the beam pattern.

Simple Array Measurements

The first experiment was conducted to determine the result of transmitting from two MIR transmitters simultaneously. The purpose is to see if the voltage wavelets radiated from two transmitters added at the receiver.

Figure 5 is a diagram of the test setup showing two closely spaced MIR transmitter/antenna units, A and B. The transmitters are triggered simultaneously so that the two transmitted signals arrive at the receiving antenna at the same time.

Measurements were made at two 'separations': 26 in. and 105 in. The measurement procedure consisted of first pointing Antenna B away from the receiving antenna and recording the received voltage-versus-time signal transmitted by Antenna A only. Then the measurement was repeated for recording Antenna B signal only. Finally antennas A and B were pointed at the receiving antenna to record the combined transmitted signal.

Figure 6 shows plots of the received signal for the 26-in. separation for Antenna A and Antenna B. The individual signals are nearly identical. The "Antennas A and B" plot, **Fig. 7**, is the received signal when both transmitting antennas are pointed at the receiver. The individual A and B signals were mathematically added in a computer and are plotted in **Fig. 8**, "Antennas A plus B." Note that the results are nearly identical. Similar results were obtained when the separation was increased to 105 in.

In conclusion, when two identical transmitting antennas are directed at a receiving antenna the voltage signals are added, thus doubling the received voltage.

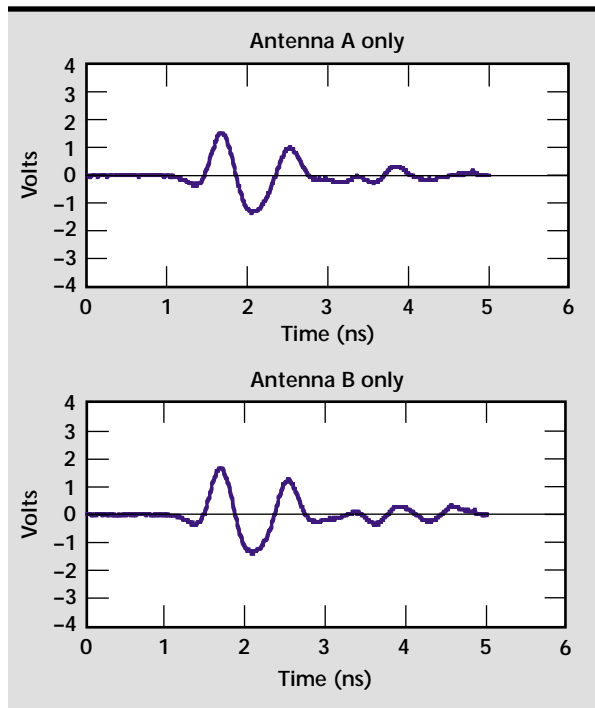


Figure 6. Signals transmitted from Antennas A and B.

Multi-Element Array Measurements

A five-element MIR array was assembled and tested as illustrated in **Fig. 9**, with four transmitters on the outside of the square and one MIR receiver in the center. The transmitters were synchronized electronically to focus the multi-element beam about 10 ft in front of the array. **Figures 10** and **11** show the

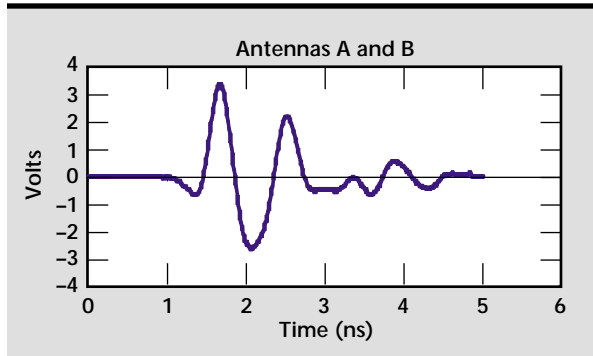


Figure 7. Signal transmitted from both antennas simultaneously.

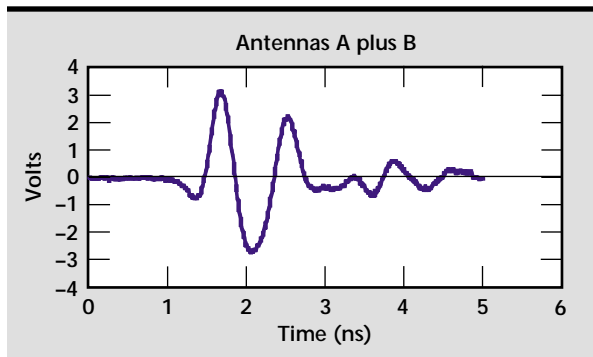


Figure 8. Result of mathematically adding signals from Antennas A and B.

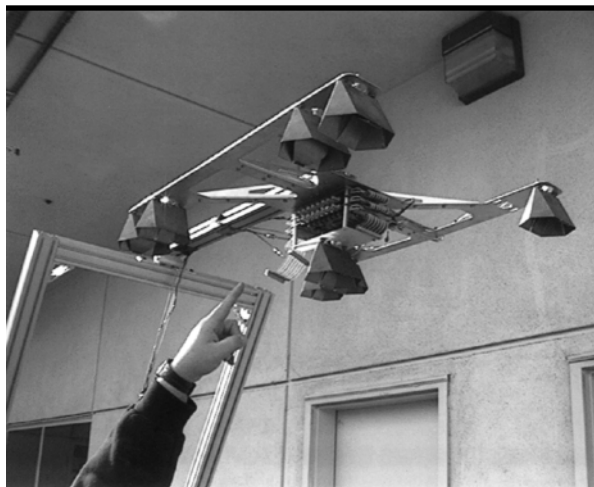


Figure 9. UWB array setup using four transmitters and one receiver.

results of the reflected signal as each transmitter is turned on in sequence.

The signal reflected from the ground increases in amplitude as more transmitters are turned on without a noticeable increase in clutter and noise. Therefore, the signal-to-noise is improved as more transmitters are used, obviously increasing the radar range and performance.

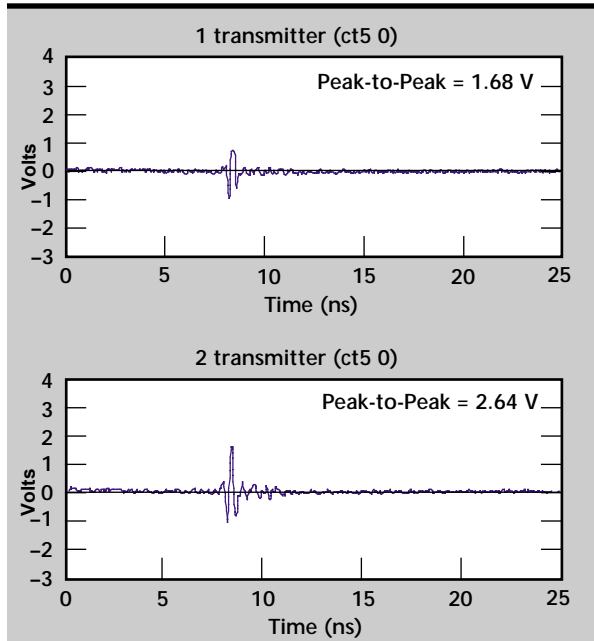


Figure 10. Reflected signal when one and then two transmitters are turned on.

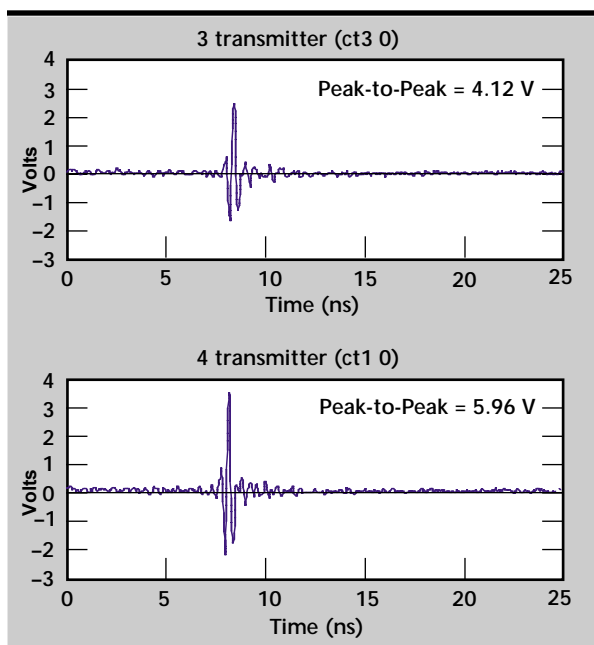


Figure 11. Reflected signal when three and then four transmitters are turned on.




Figure 12. Linear array of eight transmitters and one receiver.

A nine-element linear array was also assembled and tested as seen in **Fig. 12**. The single receiving unit is at the center of the array with four transmitters on either side. The transmitter synchronization test results are the same as for the five-element array, except that the reflected signal is the superposition of eight transmitters.

Future Work

Other groups both inside and outside LLNL are showing interest in multi-element UWB arrays. As an example, a presentation was made to DARPA on using UWB arrays for UGF characterization. Present day GPR will not reliably detect deep UGF. Model studies indicate that a large GPR array will increase radar range to a level that will interest DARPA and also DTRA. These programs and others will be pursued.

References

1. R. J. Lytle, E. F. Laine, D. L. Lager, and D. T. Davis (1979), "Cross-borehole electromagnetic probing to locate high-contrast anomalies," *Geophys.*, Vol. **44**, No. 10, October.
2. W. Daily, A. Ramirez, D. LaBrecque, and J. Nitao (1992), "Electrical resistivity tomography of vadose water movement," *Water Resource Research*, Vol. **28**, pp. 1429–1442.
3. S. D. Nelson and E. Johansson (1995), "Single pass surface-to-borehole reconstruction," *Engineering Research, Development and Technology*, Lawrence Livermore National Laboratory, Livermore, California (UCRL-53868-95).
4. A. Ramirez, W. Daily, M. Butner, and D. LaBrecque (1997), "Electrical resistivity monitoring of the thermomechanical heater test in Yucca Mountain," *Proc. of the Symp. on the Application of Geophysics to Engineering and Environmental Problems*, Reno, Nevada, Vol. **1**, pp. 11–20.
5. J. Mast, S. Azevedo, W. Haddad, L. Ng, and G. Burnett, "Micropower impulse radar technology and applications," Lawrence Livermore National Laboratory, Livermore, California (UCRL-ID-130474).
6. S. D. Nelson (1994), "Electromagnetic modeling for ground penetrating radar using fine difference time domain modeling codes," *Proc. on Advanced Microwave and Millimeter Wave Detectors, SPIE Proceedings*, Vol. **2275**, July.
7. J. E. Mast and E. M. Johansson (1994), "Three-dimensional ground penetrating radar imaging using multi-frequency diffraction tomography," *SPIE*, Vol. **2275**, July.
8. E. M. Johansson *et al.* (1994), "Three-dimensional ground penetrating radar imaging using synthetic aperture time domain focusing," *Proc. on Advanced Microwave and Millimeter Wave Detectors, SPIE Proceedings*, Vol. **2275**, July.
9. J. J. Roberts, E. Carlberg, and W. Lin, "Electrical properties of tuff from the ESF as a function of water saturation and temperature," Lawrence Livermore National Laboratory, Livermore, California (UCRL-ID-129594).
10. N. Osumi and K. Ueno (1988), "Detection of buried plant," *IEE Proc. on Communication, Radar, and Signal Processing*, Vol. **135**, Pt. F, pp. 330–342, August.
11. G. Junkin and A. P. Anderson (1988), "Limitations in microwave holographic synthetic aperture imaging over a lossy half-space," *IEE Proc. on Communication, Radar, and Signal Processing*, Vol. **135**, Pt. F, pp. 321–329, August.
12. Y. Michiguchi, K. Hiramoto, M. Nishi, T. Ootaka, and M. Okada (1988), "Advanced subsurface radar system for imaging buried pipes," *IEEE Trans. on Geoscience and Remote Sensing*, Vol. **GE-26**, pp. 733–740, November.
13. C. Liu and L. C. Shen (1991), "Numerical simulation of subsurface radar for detecting buried pipes," *IEEE Trans. on Geoscience and Remote Sensing*, Vol. **GE-29**, pp. 795–798, September.
14. A. J. Devaney (1982), "A filtered back propagation algorithm for diffraction tomography," *Ultrasonic Imaging*, Vol. **4**, pp. 336–350, April.
15. E. A. Robinson and S. Treitel (1980), *Geophysical Signal Analysis*, Prentice-Hall, Englewood Cliffs, New Jersey.
16. H. Lee (1984), "Formation of the generalized backward projection method for acoustical imaging," *IEEE Trans. on Sonics and Ultrasonics*, Vol. **31**, pp. 157–161, May. 

Photonic Velocimetry System Optimization

Paul D. Sargis, Nicole E. Molau, and Jeffrey B. Cooke
Defense Sciences Engineering Division
Electronics Engineering

Oliver T. Strand
Defense and Nuclear Technology

Mark E. Lowry
Information Science and Technology Program

We have developed an optimized photonic Doppler velocimeter with improved stability and stronger signal levels compared to our FY-98 prototype as a diagnostic for high explosives tests.

Introduction

Surface velocity measurements are of great interest to the high-explosives physics community. Currently, physicists at Lawrence Livermore National Laboratory (LLNL) perform these measurements using a technique called Fabry-Perot Velocimetry (FPV). Although FPV yields excellent data, the total number of data channels will always be less than optimum due to the high procurement cost of custom hardware, the high manpower costs, and the large volume occupied by FPV.

Photonic Doppler velocimetry (PDV) is intended to supplement the FPV diagnostic with many additional low-cost data channels. Our hardware consists of commercial off-the-shelf telecommunications components that fit together in a small chassis. Data is recorded on a transient digitizing oscilloscope.

Figure 1 illustrates the basic PDV system. Infrared light from a laser passes through a multi-mode fiber-optic coupler and is focused onto a moving surface by means of a probe lens. The reflected light is Doppler-shifted and is heterodyned with a fraction of the laser output in a "square law" optical detector. Under the appropriate polarization and modal conditions, the detector generates an electrical current proportional to the square of the optical fields. For the Doppler-shifted light, this corresponds to a beat frequency proportional to the instantaneous velocity of the target. Multi-mode fiber is used to maximize the amount of light collected from the target.

We carried out a successful R&D demonstration of this technique in FY-98. When operated in parallel with the FPV diagnostic, our data showed excellent agreement. At the end of that year, however, it became clear that another year of development would be necessary to optimize the signal-to-noise ratio and improve the stability of the system.

Progress

Our efforts in FY-99 have focused on identifying the causes of system instability and weak signal levels. Since we demonstrated consistency of results with the FPV system during explosives testing last year, we confined our experiments to the photonics laboratory this year.

Last year, our actual system configuration was a bit more complicated than the diagram shown in **Fig. 1**. We used commercial off-the-shelf probes that

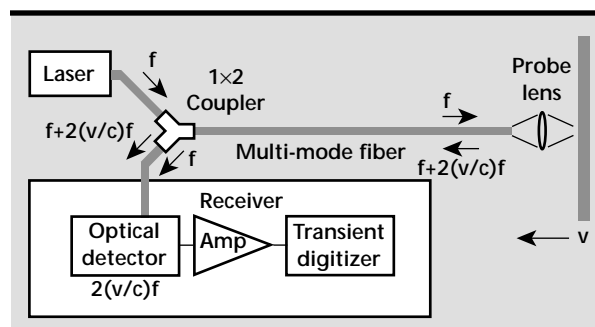


Figure 1. Basic block diagram of the photonic Doppler velocimeter system.

had been designed to reduce optical back-reflections from the surface of the lens to a level of 0.01%. This is generally a desirable specification in the fiber-optics industry, but in our case, it required us to inject a fraction of the laser source power back into the detector to permit heterodyning with the Doppler-shifted light. We accomplished this by using a 2- \times -2 fiber-optic coupler as shown in **Fig. 2**.

Early in the year, we came to the conclusion that a major source of our heterodyne inefficiency was due to this practice of having the Doppler-shifted light and the unshifted laser light traverse different optical paths on the way to the optical detector. The Doppler-shifted light was filling different modes and undergoing different polarization changes than the unshifted laser light, due to the extra segment of multi-mode fiber between the probe and the coupler. The most likely causes of the unstable heterodyne signal are the spatial overlap of the speckle patterns and the polarization state overlap of the two signals.

Upon recognition of this problem, we began using probes having an optical back-reflection of 3%. This is approximately equal to the level of reflection from the diffuse moving surface whose velocity we are measuring. In this new configuration, both wavelengths follow the same fiber-optic path, as illustrated in **Fig. 1**.

We also addressed the problem of polarization instability. The laser generates polarized light, but multi-mode fiber does not depolarize it. Instead, the polarization wanders in a random fashion as the light passes through the fiber. This causes the heterodyne signal to vary in amplitude. In addition, repositioning or creating bends in the fiber induces changes in the polarization state at the detector. In fact, we have been able to demonstrate almost total extinction of the heterodyne signal by moving the fiber into just the right position.

Since the development of a depolarized laser source was beyond the scope of this project, we built a polarization diversity receiver, as illustrated in **Fig. 3**, to address the polarization instability issue. The polarization diversity receiver takes the place of the receiver block in **Fig. 1**. The incoming light is collimated into a miniature polarization beam-splitting

cube. The orthogonal polarization states are each collimated into a short multi-mode fiber, followed by an optical detector. Ideally, when one polarization state is at a null, the orthogonal state is at a maximum. However, due to the poor collimation inherent with a multi-mode source, the actual extinction ratio is only five to one.

We tested the polarization-diversity receiver on a low-velocity experiment involving a shock-driven niobium foil target. The niobium foil has a diffuse surface and is identical to the material we use for surface ejecta measurements. Transient digitizer data from the S and P polarization states is shown in **Fig. 4**. Some of the amplitude variation can be attributed to motion of the target. However, the drastic amplitude change at 7 μ s would suggest that the polarization wanders on a microsecond time scale. It is therefore advisable to record both polarization states so that a high signal-to-noise ratio can be obtained from one channel or the other.

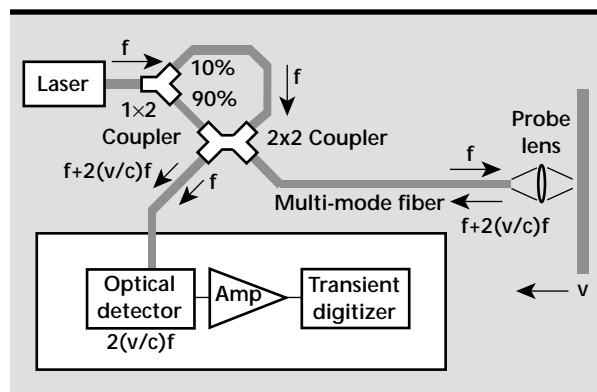


Figure 2. Detailed block diagram of FY-98 photonic Doppler velocimeter system.

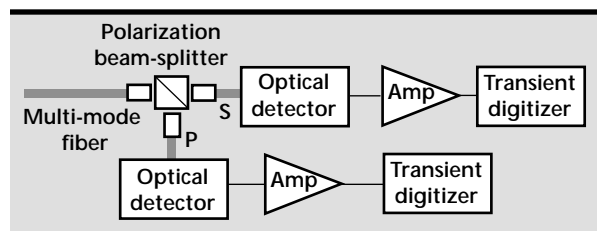


Figure 3. Polarization diversity receiver diagram.

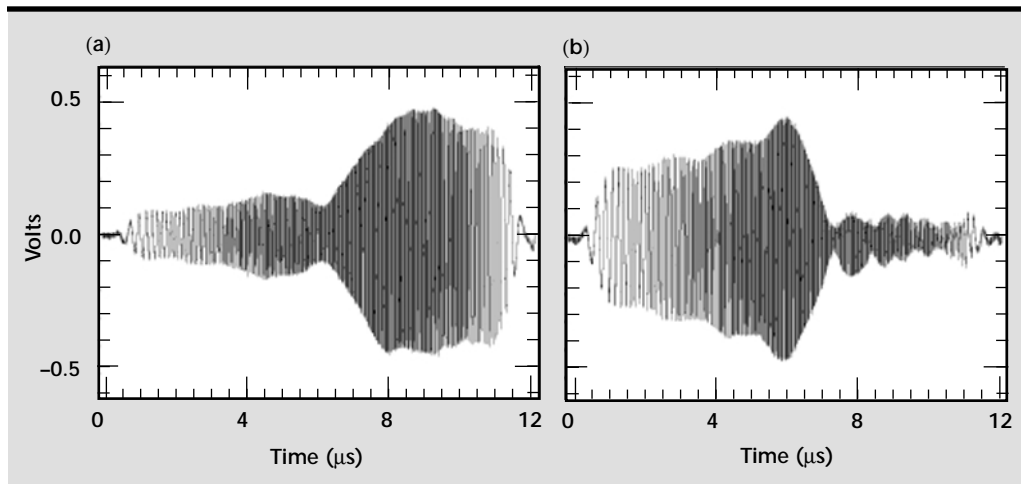


Figure 4. Raw data from niobium foil experiment:
(a) S polarization,
(b) P polarization.

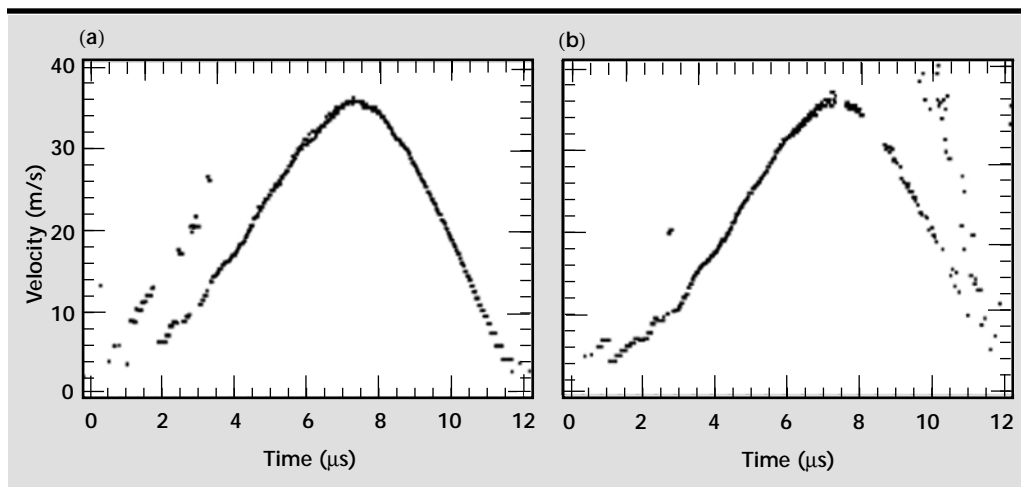


Figure 5. Processed data from niobium foil experiment:
(a) S polarization,
(b) P polarization.

The Doppler beat frequency signal from each channel was converted to instantaneous frequency versus time, and then to velocity versus time, as shown in **Fig. 5**. No filtering or smoothing was used to obtain these results. The instantaneous frequency was obtained by calculating the time between zero crossings. A more sophisticated technique such as a sliding power spectral density calculation yields smoother results, but this simple processing method emphasizes the value of recording both polarization states.

Future Work

We plan to develop a versatile field-hardened version of the PDV that can be used for a wide variety of high-explosives applications at LLNL. Before we release the hardware for general use, we will verify the reliability on a series of dedicated shots at the High Explosives Applications Facility (HEAF). We will also refine our data processing techniques so that experimenters will have quick post-shot access to velocity data. 